University of Alberta

Magnetic Resonance Spectroscopy Editing Techniques of Coupled Spin Systems at High Field

by

Jeff Snyder ©

A thesis submitted to the Faculty of Graduate Studies and Research
in partial fulfillment of the requirements for the degree of

Doctor of Philosophy

Physics

Edmonton, Alberta
Fall 2008

Library and
Archives Canada

Published Heritage
Branch

395 Wellington Street
Ottawa ON K1A 0N4
Canada

Bibliothèque et
Archives Canada

Direction du
Patrimoine de l'édition

395, rue Wellington
Ottawa ON K1A 0N4
Canada

Your file Votre référence
ISBN: 978-0-494-46427-4
Our file Notre référence
ISBN: 978-0-494-46427-4

NOTICE:
The author has granted a non-exclusive license allowing Library and Archives Canada to reproduce, publish, archive, preserve, conserve, communicate to the public by telecommunication or on the Internet, loan, distribute and sell theses worldwide, for commercial or non-commercial purposes, in microform, paper, electronic and/or any other formats.

The author retains copyright ownership and moral rights in this thesis. Neither the thesis nor substantial extracts from it may be printed or otherwise reproduced without the author's permission.

AVIS:
L'auteur a accordé une licence non exclusive permettant à la Bibliothèque et Archives Canada de reproduire, publier, archiver, sauvegarder, conserver, transmettre au public par télécommunication ou par l'Internet, prêter, distribuer et vendre des thèses partout dans le monde, à des fins commerciales ou autres, sur support microforme, papier, électronique et/ou autres formats.

L'auteur conserve la propriété du droit d'auteur et des droits moraux qui protège cette thèse. Ni la thèse ni des extraits substantiels de celle-ci ne doivent être imprimés ou autrement reproduits sans son autorisation.

In compliance with the Canadian Privacy Act some supporting forms may have been removed from this thesis.

While these forms may be included in the document page count, their removal does not represent any loss of content from the thesis.

Conformément à la loi canadienne sur la protection de la vie privée, quelques formulaires secondaires ont été enlevés de cette thèse.

Bien que ces formulaires aient inclus dans la pagination, il n'y aura aucun contenu manquant.

Canada

To Jodi,
For all your support
And the fun we had in Edmonton

Abstract

Magnetic resonance spectroscopy (MRS) provides a non-invasive tool for investigating chemical concentrations in the human brain. The detection of metabolites is useful in understanding functional pathways in healthy and diseased states. Many important metabolites are composed of multiple interacting spins coupled through chemical bonds in the molecule. Whereas the observation of strong uncoupled (singlet) resonances is straightforward, complex coupling patterns and signal overlap often hinder the detection of coupled spin systems, rendering quantification problematic. One of the primary goals of this project is to investigate spectral editing techniques to detect coupled spin systems and provide a means for increasing the accuracy of quantification.

A new method of spectral editing based on subtraction spectroscopy is proposed, which relies on signal differences at constant echo time (TE) produced by varying the inter-pulse delays in an asymmetric PRESS sequence. The method requires no spectrally selective pulses or multiple quantum filters, and can be easily implemented with a standard PRESS sequence. All non-varying spectral information is maintained, in contrast to other popular editing techniques. In terms of strongly coupled spin systems, the procedure is demonstrated for glutamate and glutamine discrimination, as well as simulated optimization of field strength for detection of several strongly coupled metabolites. To produce the necessary TE space variations for weakly coupled systems, the flip angle of the second refocusing pulse was varied. This technique was applied for the detection of γ-aminobutyric acid, which is completely obscured at standard clinical field strengths.

A second editing method investigated the optimization of PRESS timing parameters at multiple field strengths for the simultaneous detection of glutamate and glutamine in vivo, by maximizing the signal yield and minimizing the significant overlap at lower field strengths. Finally, the effect of radiofrequency interference effects was studied at high field to investigate signal losses due to reduced excitation and refocusing in spectroscopic images. Possible differences between coupled and uncoupled spin systems were investigated in spectroscopic imaging at 4.7 T.

Acknowledgements

First, I would like to thank my supervisor, Dr. Alan Wilman, for guidance in my research and discussing the daily questions I had during the program. Also, I appreciate the time invested by the other members of the supervisory committee, Dr. Frances Fenrich and Dr. Jack Tuszynski. It was an honour to have Dr. M. Albert Thomas as the external examiner for the defence, and I appreciate his time in critiquing the thesis and travelling to Canada.

Thank you to Dr. Richard Thompson for discussing ideas with me, however impractical they might have been, and also for helping me with the simulator which was fundamentally important to my work. I am grateful to Dr. Chris Hanstock for all his contributions in aiding my knowledge of spectroscopy. Also, thank you to Dr. Peter Allen for inspiring me in the pursuit of my project.

I appreciate my fellow graduate students for volunteering for my long experiments. Thank you to Rob Stobbe for providing a home for me in the last few months of my program and for the many talks about politics, religion, and life in general we had while sharing an office. Also, thank you to Dr. Jacob Ellegood for dropping by my office every day to chat and for the fun at ISMRMs, to Dr. Atiyah Yahya for reminding me to keep up my Spanish, and to Dr. Yusuf Bhagat for his encouragement during my program and discussions about sports.

I owe many good times to my extended family during my stay in Edmonton: Dallas and Lesley for their support and encouraging Jodi that my pursuing an academic career was an ok thing to do, Kory and Tim for all the great talks and fun times during the holidays and providing me with a better overall picture of life, Mom Green and Brad for all their helpful advice and keeping us sane, and Mom and Dad for supporting me in my academic pursuits from the beginning and their understanding.

Finally, I am indebted to Jodi for all her time and effort in maintaining our long term goals as a family and her unending support during the many changes in our plans in the last few years, and her openness to trying new things and taking on some tough challenges. Also, Erika and Reese have brightened each day with their smiles and simple outlook on life. "Molly in her-rasions..."

Table of Contents

Chapter 1: Introduction 1

1.1 Introduction 1

1.2 Spin Angular Momentum 5
  1.2.1 General One Spin Systems 5
  1.2.2 Two Spin Systems 8
  1.2.3 Density Matrix 11
    1.2.3.1 Time Evolution 14

1.3 Theoretical Properties of Nuclear Magnetic Resonance 17
  1.3.1 Spin Interaction with a Static Magnetic Field 17
  1.3.2 Macroscopic Magnetization 20
    1.3.2.1 Thermal Equilibrium Density Operator 23
  1.3.3 Radiofrequency Pulses and the NMR Experiment 24
    1.3.3.1 RF Field Effects on the Density Operator 25
  1.3.4 Relaxation 28

1.4 Spin Interactions 33
  1.4.1 Chemical Shift 33
    1.4.1.1 Chemically Equivalent Nuclei 35
    1.4.1.2 Density Matrix Evolution: Chemical Shift 38
  1.4.2 Spin Coupling 39
    1.4.2.1 Density Matrix Evolution: Weak Coupling 43
    1.4.2.2 Some Aspects of Strong Coupling 44

1.5 Localization 46
  1.5.1 Gradients 46
    1.5.1.1 Slice Selection 47
    1.5.1.2 Gradient Effects on the Density Operator 49
  1.5.2 Localization Schemes in Spectroscopy 49
    1.5.2.1 PRESS 50
    1.5.2.2 STEAM 51
    1.5.2.3 Spectroscopic Imaging 53

1.6 Techniques for Evolution of a Weakly Coupled System Under PRESS 55
  1.6.1 The First 90° Pulse 57
  1.6.2 The First Evolution Period 58
  1.6.3 The First 180° Pulse 60
    1.6.3.1 Spoiler Gradients 60
  1.6.4 The Remainder of the Sequence 62

1.6.5 Contrasts to Strong Coupling.......... 64
1.6.6 Other PRESS Aspects and Numerical Simulation.......... 65

1.7 Common In Vivo Metabolites.......... 67

1.8 References.......... 75

Chapter 2: Strongly Coupled Versus Uncoupled Spin Response to Radiofrequency Effects: Application to Glutamate and Glutamine in Spectroscopic Imaging **82**

2.1 Introduction.......... 82

2.2 Methods.......... 85
2.2.1 Theoretical Simulations.......... 85
2.2.2 Single Voxel Experiments.......... 88
2.2.3 Spectroscopic Imaging Experiments.......... 89
2.2.4 Area Calculations.......... 90

2.3 Results.......... 91

2.4 Discussion.......... 96

2.5 References.......... 101

Chapter 3: Difference Spectroscopy Using PRESS Asymmetry: Application to Glutamate, Glutamine and Myo-inositol **104**

3.1 Introduction.......... 104

3.2 Methods.......... 106
3.2.1 Theory.......... 106
3.2.1.1 Numerical Simulations.......... 106
3.2.1.2 Analytical Approximations.......... 107
3.2.2 Experimental.......... 109
3.2.2.1 Phantom Experiments.......... 109
3.2.2.2 In Vivo Experiments.......... 110

3.3 Results.......... 111
3.3.1 Glutamate/Glutamine Discrimination.......... 111
3.3.2 Analytical Approximations.......... 115

3.4 Discussion.......... 120

3.5 References 124

Chapter 4: Spectral Editing of Weakly Coupled Spins Using Variable Flip Angles in PRESS Constant Echo Time Difference Spectroscopy 126

4.1 Introduction 126

4.2 Methods 128
  4.2.1 Theory 128
    4.2.1.1 Numerical Simulations 128
    4.2.1.2 Analytical Approximations 130
  4.2.2 Phantom Experiments 131

4.3 Results 132
  4.3.1 Analytical Calculations 132
  4.3.2 Simulations 135
  4.3.3 Phantom Experiments 137

4.4 Discussion 141

4.5 References 145

Chapter 5: Determination of Optimal PRESS Timings for Discrimination of Glutamate and Glutamine at 1.5 T, 3 T and 4.7 T 147

5.1 Introduction 147

5.2 Methods 149
  5.2.1 Numerical Simulations 149
  5.2.2 In Vivo Experiments 151

5.3 Results 152
  5.3.1 Optimized Timings 152
  5.3.2 In Vivo Experiments 156

5.4 Discussion 157

5.5 References 159

Chapter 6: Conclusion **161**

6.1 Constant Echo Time Difference Spectroscopy........ 162

6.2 Static Field Considerations........ 164

6.3 Future Investigations........ 165

6.4 References........ 167

Appendix 1: Spin Matrices for a Two Spin System **168**

Appendix 2: Product Operator Transformation Tables **171**

Appendix 3: Product Operator Transformation Tables for a Strongly Coupled Two Spin System **174**

List of Tables

Chapter 1: Introduction

1-1 Gyromagnetic ratios and biological concentrations for selected nuclei........ 17
1-2 T1 and T2 relaxation times for various metabolites at 1.5 T, 3 T and 4.7 T........ 31
1-3 Metabolite concentration ranges in the human brain........ 73

Chapter 2: Strongly Coupled Versus Uncoupled Spin Response to Radiofrequency Effects: Application to Glutamate and Glutamine in Spectroscopic Imaging

2-1 In vivo normalized areas for Glx PQ and Cho at different flip angles........ 93

Chapter 3: Difference Spectroscopy Using PRESS Asymmetry: Application to Glutamate, Glutamine and Myo-inositol

3-1 Optimal field strengths for subtraction spectroscopy........ 119

Chapter 5: Determination of Optimal PRESS Timings for Discrimination of Glutamate and Glutamine at 1.5 T, 3 T and 4.7 T

5-1 Calculations of percent metabolite area composition for Glu and Gln at 1.5 T, 3 T, and 4.7 T........ 155

List of Figures

Chapter 1: Introduction

1-1 Zeeman energy splittings due to the application of an applied external field........ 19
1-2 Relaxation properties for choline at 1.5 T and 4.7 T........ 30
1-3 Magnetic field interaction producing the chemical shift........ 34
1-4 Test for chemical equivalence for protons in methane........ 36
1-5 Test for chemical equivalence for protons in 2-methyl-2-butene........ 37
1-6 Possible orientations for nuclei-election pairs in an A-X bond........ 40
1-7 Intersection of excited slices for localization........ 48
1-8 Diagram of a basic PRESS sequence........ 51
1-9 PRESS and STEAM flip angle dependence........ 53
1-10 PRESS spectroscopic imaging sequence diagram........ 54
1-11 Timing diagram for a standard PRESS sequence........ 56
1-12 Sample spectrum of an AX weakly coupled system........ 63
1-13 Sample spectrum of a strongly coupled AB system........ 65
1-14 High resolution spectrum of rat brain extract........ 74

Chapter 2: Strongly Coupled Versus Uncoupled Spin Response to Radiofrequency Effects: Application to Glutamate and Glutamine in Spectroscopic Imaging

2-1 Glx PQ area calculations in TE space........ 86
2-2 Calculated B_1 map at 4.7 T........ 87
2-3 Glx and Cho spectra from phantom experiments at 90°, 80° and 65°........ 91
2-4 Graph of simulated and experimental areas for Glx PQ and Cho........ 92
2-5 Single voxel in vivo spectra at various flip angles........ 94
2-6 Spectroscopic imaging data at 4.7 T........ 95

Chapter 3: Difference Spectroscopy Using PRESS Asymmetry: Application to Glutamate, Glutamine and Myo-inositol

3-1 TE space analysis for the MN group of Glu and Gln........ 112
3-2 Simulated spectra at difference spectroscopy timings for Glu and Gln........ 114
3-3 Phantom and volunteer spectra at subtraction timings........ 115
3-4 Myo-inositol TE space signal maps........ 116
3-5 Analysis of J and chemical shift dependence on subtraction experiments........ 117
3-6 Calculated yields based on the AB approximation for various metabolites........ 120

Chapter 4: Spectral Editing of Weakly Coupled Spins Using Variable Flip Angles in PRESS Constant Echo Time Difference Spectroscopy

4-1 Calculated TE space area maps for a weakly coupled AX system...... 133
4-2 Calculated maximum difference spectroscopy yield based on a two spin system with J = 7.3 Hz and Δ = 226 Hz.................................... 134
4-3 TE space area maps produced by the simulator at 4.7 T for the A_2 group of GABA under PRESS excitation.. 135
4-4 GABA and Cr spectra from the subtraction simulations.................... 136
4-5 GABA phantom subtraction spectra... 138
4-6 GABA and Cr phantom subtraction spectra...................................... 140

Chapter 5: Determination of Optimal PRESS Timings for Discrimination of Glutamate and Glutamine at 1.5 T, 3 T and 4.7 T

5-1 Simulated short echo time spectra of Glu and Gln at various field strengths.. 153
5-2 Simulated spectra at optimized timings for Glu and Gln at 1.5 T, 3 T and 4.7 T.. 154
5-3 In vivo spectra acquired at optimized timings determined from the simulation at 1.5 T and 4.7 T.. 156

List of Symbols and Abbreviations

^{13}C	Carbon-13
^{19}F	Fluorine-19
^{1}H	Hydrogen
^{39}K	Potassium-39
^{23}Na	Sodium-23
^{31}P	Phosphorus-31
$\mathbf{B_0}$	Static magnetic field
$\mathbf{B_1}$	Excitation magnetic field (radiofrequency field)
$\mathbf{B_{eff}}$	Rotating frame effective magnetic field
B_{nuc}	Magnetic field at nuclear site
BW	Bandwidth
CHESS	CHEmical Shift Selective
Cho	Choline
Cr	Creatine
CYCLOPS	CYCLically Ordered Phase Sequence
DRY	Drastic Reduction of water signals in spectroscopY
E_Z	Energy eigenvalues
FID	Free Induction Decay
$\mathbf{G}$	Magnetic gradient field
GABA	γ-aminobutyric acid
Gln	Glutamine

Glu	Glutamate
Glx	Glutamate + Glutamine
I	Imaginary unit
I	Nuclear spin principal quantum number
$\mathbf{I}$	Nuclear angular momentum
I_X, I_Y, I_Z	Cartesian spin operators
I_+, I_-	Cartesian raising and lowering operators
$\hat{I}_+, \hat{I}_-$	Spherical raising and lowering operators
J	J-coupling constant
k	Boltzmann's constant
Lac	Lactate
LASER	Localization by Adiabatic Selective Refocusing
m_I	Nuclear spin projection quantum number
mI	Myo-inositol
M_0	Thermal equilibrium net magnetization
M_X, M_Y, M_Z	Cartesian bulk magnetization components
M_+	Observable magnetization
MQC	Multiple Quantum Coherence
MRI	Magnetic Resonance Imaging
MRS	Magnetic Resonance Spectroscopy
MRSI	Magnetic Resonance Spectroscopic Imaging
N	Number of spins
NAA	N-acetylaspartate

NAAG	N-acetylaspartylglutamate
NMR	Nuclear Magnetic Resonance
P(...)	Quantum mechanical probability
ppm	Parts per million
PRESS	Point RESolved Spectroscopy
r	Position in space
RF	Radiofrequency
SI	Spectroscopic Imaging
SQC	Single Quantum Coherence
STEAM	Stimulated Echo Acquisition Mode
SV	Single Voxel
T	Tesla
T	Temperature
T1	Longitudinal relaxation time constant
T2	Transverse relaxation time constant
Tau	Taurine
TE	Echo time
TE1	First echo time in a PRESS sequence
TE2	Second echo time in a PRESS sequence
TM	Mixing time in a STEAM sequence
TMS	Tetramethylsilane
Tr	Trace
TR	Repetition time

VOI	Volume Of Interest
WET	Water suppression Enhanced through T1 effects
$\hat{x}, \hat{y}, \hat{z}$	Cartesian unit vectors
$\hat{x}_\rho, \hat{y}_\rho$	Rotating frame unit vectors
$\hbar$	Planck's constant divided by 2π
$\mathcal{H}$	Hamiltonian
$\mathcal{H}_J$	Coupling Hamiltonian
$\mathcal{H}_{RF}$	Radiofrequency pulse Hamiltonian
$\mathcal{H}_Z$	Zeeman Hamiltonian
ℓ	Orbital quantum number
α	Flip angle for a radiofrequency pulse
δ	Chemical shift
Δz	Excited slice thickness
$\Delta\delta$	Chemical shift difference
ϕ	Arbitrary basis state
γ	Gyromagnetic ratio
μ	Nuclear magnetic moment

ρ	Density operator
θ	Flip angle
σ	Density matrix
σ	Electron shielding parameter/screening constant
ω	Resonance frequency
ω_0	Larmor frequency
ψ	Arbitrary wavefunction

Chapter 1

Introduction

1.1 Introduction

Nuclear magnetic resonance (NMR) has been used extensively in vivo as a non-invasive means of investigating internal anatomy and function. Magnetic resonance imaging (MRI) is the most predominant form in clinical use, and measures the content of protons from water in various tissues, and also provides the ability to distinguish different anatomical features and pathologies via diverse contrast mechanisms. In contrast to MRI, NMR spectroscopy (MRS) provides additional information into metabolic processes by measuring the amount of protons in different chemical metabolites in a localized area of a given tissue, allowing examination of metabolic pathways in healthy and diseased states.

The success of MRI has depended on the ample signal due to the large concentration of water in biological tissues, and to a lesser extent and similarly to MRS, the use of non-ionizing radiation in tissue preservation in contrast to other modalities including x-ray, computed tomography, and nuclear medicine. The small amount of available signal produced by metabolites has inhibited the clinical utilization of MRS, as metabolite concentrations are roughly four orders of magnitude smaller than water. MRI scans can be obtained rapidly with good spatial resolution, whereas MRS requires longer scanning times for inclusion of signal averaging, and larger volume elements (voxels) are needed to boost signal. In addition, although extra information is afforded in MRS, the variations in metabolite concentrations due to disease or trauma and their effects on the various metabolic pathways can be difficult to quantify and is rarely understood fully. Nevertheless, the ability to detect metabolite variations in pathologies can serve as an important diagnostic tool in addition to MRI, invaluable in disease investigation. Previous studies of disease in brain with MRS include (although not limited to) stroke (1-6), epilepsy (7-12), depression (13-16), multiple sclerosis (17-22), Parkinson's disease (23-26), Alzheimer's disease (27-31), schizophrenia (32-34), and amyotrophic lateral sclerosis (ALS) (35-37).

In addition to the low signal available in MRS, the proton NMR spectrum for brain metabolites covers a relatively narrow frequency range, resulting in multiple overlap between signals at standard clinical field strengths. This overlap decreases the accuracy of quantification of metabolites, and in some cases can completely obscure a smaller signal. Another difficulty in quantification is produced by the coupling of spins within a particular metabolite, called J-coupling. Several important in vivo metabolites are comprised of multiple spins, and each spin in the molecule can affect the NMR properties of neighboring spins via interaction through chemical bonds This interaction effectively splits a single resonance into multiple peaks, with a combined area equal to the original peak in the absence of J-coupling. Therefore, signal arising from coupled spins tends to be weaker than a non-coupled spin system with the same amount of contributing protons. The amount of radiofrequency (RF) power used for the pulses and their timing in the sequence play a major role in the amplitude and phase of a particular coupled spin, unlike a system comprised of uncoupled spins. Therefore, the prediction of the signal produced following a pulse sequence is critical in quantifying coupled spin systems. Although this process may seem detrimental in observing the small signals from metabolites, the effects of J-coupling can be used as a mechanism to 'edit' the proton spectrum, by manipulating sequence parameters and suppressing surrounding resonances while maximizing the target signal. Several editing methods have been used in previous studies, including multiple quantum filtering, J-resolved spectroscopy, and others (38-47), although these techniques typically introduce complexities into the pulse sequence and reduce the clinical viability.

The many drawbacks of MRS may seem overwhelming and it is not without warrant that clinicians deem MRS as a secondary priority to MRI. Consequently, one of the primary goals of this thesis is to develop new editing strategies that are simple to use and can be easily implemented clinically. The techniques proposed use the standard spectroscopy sequences available to clinical scanners, and are general in scope to aid in the quantification of a number of metabolites. Chapter 3 describes a technique to edit strongly coupled spin systems, while Chapter 4 illustrates a method to manipulate weak coupling properties. Chapter 5 investigates the optimization of timing parameters in the pulse sequence to provide increased resolution and signal yield for specific metabolites. The methods use a standard localization scheme and are heavily dependent on numerical simulation to predict the outcome of the edited metabolite.

In addition, quantification of coupled spin systems in spectroscopic imaging (a combination of imaging and spectroscopy) is explored. Most of the experiments for this work are conducted at high field (usually 4.7 T), which introduces new problems in spectral quantification when spectroscopic imaging is used. The wavelength of the RF field is comparable to human head dimensions at 4.7 T, and therefore superposition effects (destructive interference) produce a spatial RF dependence. Depending on the location of a voxel in the spectroscopic imaging experiment, the amplitude of a particular metabolite will vary with the disparate RF field. The RF field effect is investigated for coupled and uncoupled systems in Chapter 2.

Due to the complexity of coupled spin systems, the main theme in the thesis is the density operator/matrix approach for describing the evolution of spins in the NMR environment throughout an entire experiment or pulse sequence, introduced in the subsequent section. The theoretical construct of the density operator is developed first from basic quantum mechanical formulations of spin angular momentum, followed by the Liouville – von Neumann equation describing the time evolution of the density operator – an essential progression in spin mechanics. This treatment is followed by introduction to individual aspects of the NMR experiment and their influence on the evolution of the density operator based on the relevant Hamiltonian operator. The collection of interactions can be summed into the effects an entire pulse sequence has on the density operator, and a theoretical prediction of the spectral information for a particular spin system.

1.2 Spin Angular Momentum

In order to discuss the general properties of nuclear magnetic resonance, an understanding of general angular momentum as it is applied to nuclear spins is required. The famous Stern-Gerlach experiment (48,49) illustrated that previous theories relying on orbital angular momentum, with integer quantum number, ℓ, could not explain the results of their experiment. The product was the concept of spin angular momentum, which enabled the use of a half integer angular momentum system, with principal quantum number I and projection quantum number m_I, where:

$$I \in \left\{0, \frac{1}{2}, 1, \frac{3}{2}, \ldots\right\}, \quad \text{and} \qquad (1.1)$$

$$m_I \in \{-I, -I+1, \ldots, I-1, I\}.$$

The remainder of this thesis focuses on the ^{1}H nucleus, with I = 1/2, and possible m_I values of –1/2 and 1/2. The quantum mechanical framework for a one spin system is described in the next section.

1.2.1 General One Spin Systems

For a one spin experiment comprised of a two level system, a pair of basis states are required. In accordance with the development of the interaction between external magnetic fields and the nuclear spin discussed in the next section, the natural choice is the basis states of I^2, the magnitude squared operator, and I_Z, the z-axis projection operator. Both states have a principal quantum number of I = 1/2, and have notation $|+\rangle$ and $|-\rangle$ with matrix form:

$$|+\rangle = \left|I=\frac{1}{2}, m_I=+\frac{1}{2}\right\rangle = \begin{bmatrix}1\\0\end{bmatrix},$$
$$|-\rangle = \left|I=\frac{1}{2}, m_I=-\frac{1}{2}\right\rangle = \begin{bmatrix}0\\1\end{bmatrix}. \tag{1.2}$$

In this basis, the magnitude of the spin angular momentum vector is:

$$\sqrt{I(I+1)}\hbar = \frac{\sqrt{3}}{2}\hbar, \tag{1.3}$$

and therefore the I^2 operator is the identity matrix multiplied by the above result squared:

$$I^2 = \frac{3}{4}\hbar^2\begin{bmatrix}1 & 0\\0 & 1\end{bmatrix}. \tag{1.4}$$

At this point, it is beneficial to exclude the $\hbar$ factor in operators to convert to the more useful units of Hertz rather than Joules in subsequent Hamiltonian calculations. In this basis, the representation of the I_Z operator is simply a diagonal matrix with the relevant eigenvalues as entries:

$$I_Z = \frac{1}{2}\begin{bmatrix}1 & 0\\0 & -1\end{bmatrix}. \tag{1.5}$$

The following relations are obtained when I_Z is operated on the eigenstates:

$$I_Z|+\rangle = \frac{1}{2}|+\rangle, \quad I_Z|-\rangle = -\frac{1}{2}|-\rangle. \tag{1.6}$$

The I_X and I_Y projection operators are needed to complete the treatment of the spin 1/2 system. I_X and I_Y are determined from the raising and lower operators, I_+ and I_-, respectively, where:

$$I_\pm = I_X \pm iI_Y, \tag{1.7}$$

and *i* is the imaginary unit. The effects of operating I_+ and I_- on the eigenstates is:

$$I_+|+\rangle = 0, \quad I_+|-\rangle = |+\rangle,$$
$$I_-|-\rangle = 0, \quad I_-|+\rangle = |-\rangle. \tag{1.8}$$

It is now straightforward to represent these operators in matrix form, first by evaluating I_+ and I_-, and then applying the relation in eqn. (1.7) to calculate I_X and I_Y:

$$I_+ = \begin{bmatrix} 0 & 1 \\ 0 & 0 \end{bmatrix}, \quad I_- = \begin{bmatrix} 0 & 0 \\ 1 & 0 \end{bmatrix}$$
$$I_X = \frac{1}{2}\begin{bmatrix} 0 & 1 \\ 1 & 0 \end{bmatrix}, \quad I_Y = \frac{1}{2i}\begin{bmatrix} 0 & 1 \\ -1 & 0 \end{bmatrix}. \tag{1.9}$$

In general when discussing a one spin system, there are finite probabilities for being in either the $|+\rangle$ and $|-\rangle$ states, and therefore a general wavefunction is needed to represent these possibilities. The wavefunction, ψ, is a linear combination of the two states, and is generally time-dependent:

$$|\psi\rangle = c_+|+\rangle + c_-|-\rangle, \tag{1.10}$$

where c_+ and c_- are complex numbers which reflect the relative proportions of the two states. It should be noted that the basis states are orthogonal and normalized:

$$\langle +|+\rangle = \langle -|-\rangle = 1,$$
$$\langle +|-\rangle = \langle -|+\rangle = 0. \tag{1.11}$$

The quantum mechanical probability for the spin system being in a certain state is given by the square modulus of the product of the wavefunction and the investigated state. For example, the probability of the system being in the $|+\rangle$ state, $P(|+\rangle)$, is given by:

$$P(|+\rangle) = |\langle +|\psi\rangle|^2, \tag{1.12}$$

and using the orthogonality of the basis states, this expression simplifies to:

$$P(|+\rangle) = c_+^* c_+, \tag{1.13}$$

where the asterisk denotes the complex conjugate. Starting with this general foundation of spin mechanics, it is possible to explore the simplest interaction in nuclear magnetic resonance: the interaction of a spin with an external magnetic field. However, many interesting phenomena occur when two spins interact with each other, and therefore it is necessary to expand the treatment to a general two spin system.

1.2.2 Two Spin Systems

A general two spin system, with spins labeled I and S, has four possible spin orientations and therefore four basis states using the previous I^2 and I_Z basis. The principal quantum numbers, I and S, have the value of 1/2 and are generally excluded when denoting the spin states. The states are defined by the possible projection quantum numbers for each spin. Explicitly, these four states can be written as:

$$\begin{aligned}
\left|m_I = \frac{1}{2}; m_S = \frac{1}{2}\right\rangle &= |++\rangle \\
\left|m_I = \frac{1}{2}; m_S = -\frac{1}{2}\right\rangle &= |+-\rangle \\
\left|m_I = -\frac{1}{2}; m_S = \frac{1}{2}\right\rangle &= |-+\rangle \\
\left|m_I = -\frac{1}{2}; m_S - = \frac{1}{2}\right\rangle &= |--\rangle .
\end{aligned} \tag{1.14}$$

Similarly to the one spin case, the + sign denotes a projection quantum number of 1/2, and the – sign a projection quantum number of –1/2. The order the signs appear in the ket is important, as the first sign denotes the projection quantum number for the I spin and the second sign denotes the number for the S spin. The basis states are defined in matrix form in the following equation:

$$|++\rangle = \begin{bmatrix}1\\0\\0\\0\end{bmatrix}, \quad |+-\rangle = \begin{bmatrix}0\\1\\0\\0\end{bmatrix}, \quad |-+\rangle = \begin{bmatrix}0\\0\\1\\0\end{bmatrix}, \quad |--\rangle = \begin{bmatrix}0\\0\\0\\1\end{bmatrix}. \tag{1.15}$$

The resultant spin matrices will therefore be 4 x 4, and can be computed by taking the direct product of a corresponding 2 x 2 one spin matrix with the identity matrix, with product order dependent on multiplication of I before S. For example, in the case of I_Z, the spin matrix can be calculated by:

$$I_Z = I_Z \times 1 = \frac{1}{2}\begin{bmatrix}1 & 0\\0 & -1\end{bmatrix} \times \begin{bmatrix}1 & 0\\0 & 1\end{bmatrix} = \frac{1}{2}\begin{bmatrix}\boxed{\begin{matrix}1 & 0\\0 & 1\end{matrix}} & \boxed{\begin{matrix}0 & 0\\0 & 0\end{matrix}}\\ \boxed{\begin{matrix}0 & 0\\0 & 0\end{matrix}} & \boxed{\begin{matrix}-1 & 0\\0 & -1\end{matrix}}\end{bmatrix}. \tag{1.16}$$

Each element in I_Z is multiplied by each element of the identity matrix to produce an individual element in the 4 x 4 representation. It should be noted that each element in a spin matrix is equivalent to $\langle\phi_1|I_n|\phi_2\rangle$, where ϕ_1 and ϕ_2 can be any one of the four basis states, *i.e.* $|++\rangle$, $|+-\rangle$, $|-+\rangle$, or $|--\rangle$, and the subscript n denotes an arbitrary I spin operator. For illustrative purposes and using I_Z as an example, we can label the matrix as (excluding the factor of 1/2):

$$I_Z = \begin{array}{c|cccc|} & |++\rangle & |+-\rangle & |-+\rangle & |--\rangle \\ \hline \langle++| & 1 & 0 & 0 & 0 \\ \langle+-| & 0 & 1 & 0 & 0 \\ \langle-+| & 0 & 0 & -1 & 0 \\ \langle--| & 0 & 0 & 0 & -1 \end{array}. \tag{1.17}$$

As stated previously, the I_Z operator measures the projection of the I spin onto the z-axis. Therefore, I_Z acting on $|+\,+\rangle$ and $|+\,-\rangle$ produces $1/2|+\,+\rangle$ and $1/2|+\,-\rangle$, respectively, and I_Z operating on $|-\,+\rangle$ and $|-\,-\rangle$ produces $-1/2|-\,+\rangle$ and $-1/2|-\,-\rangle$. This analysis allows easy verification for the generation of the 4 x 4 spin matrices discussed above, as the I_Z matrix is simple to compute in this manner.

The procedure to calculate the z-axis projection operator for the S spins, S_Z, differs from I_Z only in the order of multiplication, with the identity matrix placed first:

$$S_Z = 1 \times S_Z = \begin{bmatrix} 1 & 0 \\ 0 & 1 \end{bmatrix} \times \frac{1}{2}\begin{bmatrix} 1 & 0 \\ 0 & -1 \end{bmatrix} = \frac{1}{2}\begin{bmatrix} \boxed{\begin{matrix} 1 & 0 \\ 0 & -1 \end{matrix}} & \boxed{\begin{matrix} 0 & 0 \\ 0 & 0 \end{matrix}} \\ \boxed{\begin{matrix} 0 & 0 \\ 0 & 0 \end{matrix}} & \boxed{\begin{matrix} 1 & 0 \\ 0 & -1 \end{matrix}} \end{bmatrix}. \tag{1.18}$$

The S_Z operator therefore has the following effects on each of the four basis states:

$$\begin{aligned} S_Z|++\rangle &= \frac{1}{2}|++\rangle, \quad S_Z|+-\rangle = -\frac{1}{2}|+-\rangle \\ S_Z|-+\rangle &= \frac{1}{2}|-+\rangle, \quad S_Z|--\rangle = -\frac{1}{2}|--\rangle. \end{aligned} \tag{1.19}$$

The remainder of the useful 2 spin matrices can be calculated in a similar manner and are given in Appendix 1. The raising and lowering operators are used extensively in spin mechanics, and it is therefore useful to state their effects on basis states explicitly. The results of the I raising and lowering operators are:

$$\begin{aligned} &I_+|++\rangle = 0, \quad I_-|++\rangle = |-+\rangle \\ &I_+|+-\rangle = 0, \quad I_-|+-\rangle = |--\rangle \\ &I_+|-+\rangle = |++\rangle, \quad I_-|-+\rangle = 0 \\ &I_+|--\rangle = |+-\rangle, \quad I_-|--\rangle = 0, \end{aligned} \tag{1.20}$$

and the S raising and lower operators have the following effects:

$$\begin{aligned} &S_+|++\rangle = 0, \quad S_-|++\rangle = |+-\rangle \\ &S_+|+-\rangle = |++\rangle, \quad S_-|+-\rangle = 0 \\ &S_+|-+\rangle = 0, \quad S_-|-+\rangle = |--\rangle \\ &S_+|--\rangle = |-+\rangle \quad S_-|--\rangle = 0. \end{aligned} \tag{1.21}$$

The spin matrices for a two spin system allow investigation of interactions between the spins, and are therefore a powerful tool in spin mechanics. Many of the spin interactions can be illustrated for a two spin system and generalized to an N-spin system, although increasing the amount of interacting spins places significant demands on the ability to produce analytical solutions.

1.2.3 Density Matrix

The density matrix is a useful tool in spin mechanics, and allows the calculation of the population of spin states and possible spin state coherences. To develop this concept, the starting point is the Schrödinger time dependent equation:

$$\mathcal{H}|\psi\rangle = i\frac{\partial}{\partial t}|\psi\rangle, \tag{1.22}$$

where the Hamiltonian, $\mathcal{H}$, has units of Hertz. A single spin system will be used for illustration, thus the definition of ψ is identical to the previous section for a generalized wavefunction based on two orthonormal eigenstates. It should also be noted that ψ is dependent on time, *i.e.* ψ(t). For this system, the expectation value for an arbitrary operator, U(t), is given by:

$$\langle U(t)\rangle = \langle \psi(t)|U|\psi(t)\rangle. \tag{1.23}$$

Expansion of eqn. (1.23) by incorporating the representation of the general wavefunction (eqn. (1.10)) yields:

$$\langle U(t)\rangle = c_+^* c_+ \langle +|U|+\rangle + c_+^* c_- \langle +|U|-\rangle + c_-^* c_+ \langle -|U|+\rangle + c_-^* c_- \langle -|U|-\rangle. \tag{1.24}$$

This equation can be written as the trace (Tr) of a product of two matrices:

$$\langle U(t)\rangle = Tr\begin{bmatrix} c_+^* c_+ & c_-^* c_+ \\ c_+^* c_- & c_-^* c_- \end{bmatrix}\begin{bmatrix} \langle +|U|+\rangle & \langle +|U|-\rangle \\ \langle -|U|+\rangle & \langle -|U|-\rangle \end{bmatrix}. \tag{1.25}$$

In practical situations, more than one spin exists and the assumption that all spins are in the same state at a given time is invalid. Therefore, it is necessary to take the ensemble average of each of the terms in the first matrix of eqn. (1.25). The density matrix, σ, is defined as the first matrix in the above equation, *i.e.*:

$$\sigma = \begin{bmatrix} c_+^* c_+ & c_-^* c_+ \\ c_+^* c_- & c_-^* c_- \end{bmatrix}. \tag{1.26}$$

The diagonal elements of σ are simply the probabilities of the system being in a given state (eqn. (1.13)), and therefore are proportional to the population. The off-diagonal elements imply an interaction between the two states, or coherence. The concept of coherence will be discussed in more detail in section 1.6.

The corresponding density operator, ρ, has matrix elements equivalent to the elements of the density matrix, such that:

$$\langle \phi_j | \rho | \phi_k \rangle = c_k^* c_j, \tag{1.27}$$

and in the one spin system, ϕ_j and ϕ_k can either be + or −. Therefore, by analyzing eqn. (1.25) and applying the definition of the density operator, the matrix representation of the expectation value of an arbitrary operator can be written as:

$$\begin{aligned} \langle U(t) \rangle &= \langle + | \rho | + \rangle \langle + | U | + \rangle + \langle + | \rho | - \rangle \langle - | U | + \rangle \\ &\quad + \langle - | \rho | + \rangle \langle + | U | - \rangle + \langle - | \rho | - \rangle \langle - | U | - \rangle. \end{aligned} \tag{1.28}$$

The expectation value in terms of the generalized indices as in eqn. (1.27), and with further simplification can be consequently expressed as:

$$\begin{aligned} \langle U(t) \rangle &= \sum_j \sum_k \langle \phi_j | \rho | \phi_k \rangle \langle \phi_k | U | \phi_j \rangle \\ &= \sum_j \langle \phi_j | \rho U | \phi_j \rangle \\ &= Tr(\rho U). \end{aligned} \tag{1.29}$$

Using this development, any expectation value for a particular observable can be calculated. Therefore, it is more efficient to use the density matrix method to evaluate spin evolution in NMR than applying evolution to individual wavefunctions. A final density operator can be computed for an entire sequence of events (*e.g.* a pulse sequence) and expectation values immediately following the sequence computed. The significance of individual elements in the density matrix will be explored in subsequent sections.

1.2.3.1 Time Evolution

The density operator is a dynamic quantity, and therefore an explanation of time evolution is required. The Schrödinger equation (eqn. (1.22)) can be expanded in terms of an arbitrary basis set, $|\phi_j\rangle$:

$$\mathcal{H}\sum c_j|\phi_j\rangle = i\frac{\partial}{\partial t}\sum_j c_j|\phi_j\rangle . \tag{1.30}$$

Multiplying the above equation by $\langle\phi_p|$, and assuming the orthogonality of the basis states, *i.e.* $\langle\phi_p|\phi_j\rangle = 0$, removes the summation from the right side of equation (1.30):

$$\sum_j c_j\langle\phi_p|\mathcal{H}|\phi_j\rangle = i\frac{\partial}{\partial t}c_p. \tag{1.31}$$

It is instructive to determine the time derivative of a single density matrix element, $\langle\phi_p|\rho|\phi_k\rangle$, in order to calculate the derivative of the coefficient, c_p:

$$\begin{aligned}\frac{\partial}{\partial t}\langle\phi_p|\rho|\phi_k\rangle &= \frac{\partial}{\partial t}c_p c_k^* \\ &= c_p\frac{\partial}{\partial t}\left(c_k^*\right) + \frac{\partial}{\partial t}\left(c_p\right)c_k^*.\end{aligned} \tag{1.32}$$

Solving for the time derivative of c_p in equation (1.31) and substituting into the above yields:

$$\frac{\partial}{\partial t}\langle\phi_p|\rho|\phi_k\rangle = ic_p\sum_j c_j^*\langle\phi_j|\mathcal{H}|\phi_k\rangle - i\sum_j c_j\langle\phi_p|\mathcal{H}|\phi_j\rangle c_k^*. \tag{1.33}$$

Note that the products $c_pc_j^*$ and $c_jc_k^*$ are elements of the density matrix, and therefore the above equation can be rewritten as:

$$\frac{\partial}{\partial t}\langle\phi_p|\rho|\phi_k\rangle = i\sum_j\langle\phi_p|\rho|\phi_j\rangle\langle\phi_j|\mathcal{H}|\phi_k\rangle - i\sum_j\langle\phi_p|\mathcal{H}|\phi_j\rangle\langle\phi_j|\rho|\phi_k\rangle. \tag{1.34}$$

The normalization of states, *i.e.* $\langle\phi|\phi\rangle = |\phi\rangle\langle\phi| = 1$, allows further simplification by elimination of the summations:

$$\frac{\partial}{\partial t}\langle\phi_p|\rho|\phi_k\rangle = i\langle\phi_p|\rho\mathcal{H}|\phi_k\rangle - i\langle\phi_p|\mathcal{H}\rho|\phi_k\rangle. \tag{1.35}$$

It is possible to rewrite eqn. (1.35) by introducing the commutator relation. For two general operators, A and B, the commutator is written as:

$$[A, B] = AB - BA. \tag{1.36}$$

If the operator AB acting on a general eigenstate is equivalent to BA acting on the same eigenstate, the operators A and B commute, and the commutation [A, B] is equal to zero. Therefore, the order of operation of A and B is irrelevant and can be interchanged. The significance of commuting operators is vitally important in quantum mechanical measurements, as commuting operators are simultaneous observables. Returning to the treatment of time evolution of the density matrix, eqn. (1.35) becomes:

$$\frac{\partial}{\partial t}\langle\phi_p|\rho|\phi_k\rangle = \langle\phi_p|i[\rho, \mathcal{H}]|\phi_k\rangle, \tag{1.37}$$

and including all possible elements of the density matrix results in:

$$\frac{\partial\rho}{\partial t} = i[\rho, \mathcal{H}]. \tag{1.38}$$

Eqn. (1.38) is called the Liouville – von Neumann equation (50) and is a restatement of the Schrödinger equation describing an ensemble of spins. If the density operator and Hamiltonian do not commute, then the density matrix will evolve with time. A simple solution occurs when the Hamiltonian is time independent, with integration of eqn. (1.38) resulting in:

$$\rho(t) = e^{-i\mathcal{H}t}\rho(0)e^{i\mathcal{H}t}, \tag{1.39}$$

where ρ(0) is the density operator at time t = 0. For time dependent Hamiltonians, the solution is much more complex, and therefore approximations will be used to preserve the time independence of the Hamiltonian operator. The description of the mechanics of evolving spin systems in specific nuclear magnetic resonance interactions using the density matrix and density operator will be discussed in subsequent sections and is central to this thesis.

1.3 Theoretical Properties of Nuclear Magnetic Resonance

1.3.1 Spin Interaction with a Static Magnetic Field

A nuclear magnetic moment is required for a nucleus to be NMR visible, and occurs when the nucleus has either an odd number of neutrons or an odd number of protons or both. Only unpaired nuclear spins are of importance. The nuclear magnetic moment, $\boldsymbol{\mu}$, a vector quantity, is related to the nuclear angular momentum, **I**, by:

$$\boldsymbol{\mu} = \gamma \boldsymbol{I} \hbar. \tag{1.40}$$

The constant, γ, is called the gyromagnetic ratio, and is specific to each nucleus of differing composition. Table 1-1 lists common nuclei used in NMR experiments, along with their biological concentration and gyromagnetic ratio. Due to the large biological concentration and gyromagnetic ratio of ^{1}H, it has typically been the mainstream choice for in vivo spectroscopy experiments, although ^{13}C and ^{31}P have also been investigated significantly.

***Table 1-1**: Gyromagnetic Ratios and Biological Concentrations for Selected Nuclei (51,52)*

Nucleus	Biological Concentration (%)*	Gyromagnetic Ratio (MHz/T)
^{1}H	100	42.58
^{13}C	2.00	10.71
^{19}F	0.037	40.05
^{23}Na	1.50	11.26
^{31}P	10.0	17.23
^{39}K	2.33	1.99

* as a percent of ^{1}H concentration

The NMR experiment requires preparation of the sample by placing it in a strong static magnetic field, $\mathbf{B_0}$. By convention, the direction of $\mathbf{B_0}$ is parallel to the z-axis, and therefore $\mathbf{B_0} = (0, 0, B_0)$ in Cartesian coordinates. Assuming the field is static and completely uniform, the Hamiltonian, $\mathcal{H}_Z$, describing the interaction energy between the nuclear magnetic moment and the static field is given by:

$$\mathcal{H}_Z = -\boldsymbol{\mu}\bullet\boldsymbol{B_0} = -\gamma\hbar B_0 I_Z \,. \tag{1.41}$$

The energy eigenvalues, E_z, can be calculated by solving the time-independent Schrödinger equation:

$$\mathcal{H}_Z\phi = E_Z\phi \,, \tag{1.42}$$

where the energy eigenstates are denoted by ϕ. Substituting the result for $\mathcal{H}_Z$ into the above equation yields:

$$-\gamma\hbar B_0 I_Z\phi = E_Z\phi \,. \tag{1.43}$$

The only operator in $\mathcal{H}_Z$ is I_Z, and therefore the energy eigenstates will also be eigenstates of I_Z. In accordance with the basis developed in the previous sections for a one spin system, the energy eigenvalues E_Z are calculated as:

$$E_Z = \mp\frac{1}{2}\gamma\hbar B_0 \,, \tag{1.44}$$

with corresponding eigenstates $|+\rangle$ and $|-\rangle$. The lower energy eigenvalue is achieved when the nuclear magnetic moment is aligned with the external magnetic field ('spin up', eigenstate $|+\rangle$). In contrast, the higher energy eigenstate, $|-\rangle$, occurs when the magnetic moment is aligned antiparallel to the external field ('spin down'). In order to induce a transition between the two levels, energy equal to the difference between the two eigenstates, $\gamma\hbar B_0$, must be applied. This transition results in a characteristic spectral line, with frequency, ω_0, related to the energy difference and given by the Larmor equation:

$$\omega_0 = \gamma B_0 \,. \tag{1.45}$$

It should be noted that in the absence of an applied magnetic field, no energy splittings (known as Zeeman splittings) are observed. Figure 1-1 shows the effect of Zeeman splitting and the corresponding transition line in frequency space.

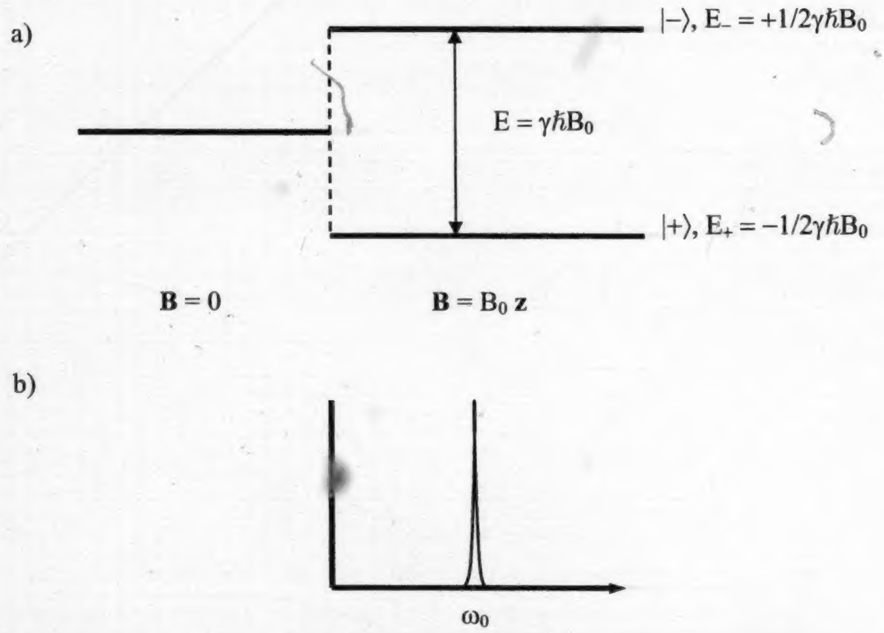
a)
$|-\rangle$, $E_- = +1/2\gamma\hbar B_0$
$E = \gamma\hbar B_0$
$|+\rangle$, $E_+ = -1/2\gamma\hbar B_0$
$\mathbf{B} = 0$
$\mathbf{B} = B_0\,\mathbf{z}$
b)
ω_0

***Figure 1-1**: a) Zeeman energy splittings due to the application of an applied external field, B_0, resulting in two energy eigenstates, $|\alpha\rangle$ and $|\beta\rangle$. b) Characteristic line of transition between $|+\rangle$ and $|-\rangle$, with Larmor frequency $\omega_0 = \gamma B_0$.*

Returning to the representation of an arbitrary wavefunction for a single spin (eqn. (1.10)), we can solve Schrödinger's equation (1.22) (assuming the Hamiltonian is time independent) to obtain the evolution of the wavefunction interacting with the static field. The solution to this particular problem is:

$$\begin{aligned} |\psi(t)\rangle &= e^{\frac{i\mathcal{H}t}{\hbar}}|\psi(0)\rangle \\ &= e^{i\gamma B_0 I_Z t}\left(c_+|+\rangle + c_-|-\rangle\right), \end{aligned} \tag{1.46}$$

and substitution of the Larmor frequency for γB_0 and replacement of the I_Z operator with the relevant eigenvalues yields:

$$|\psi(t)\rangle = e^{\frac{1}{2}i\omega_0 t}c_+|+\rangle + e^{-\frac{1}{2}i\omega_0 t}c_-|-\rangle. \tag{1.47}$$

1.3.2 Macroscopic Magnetization

A single isolated spin is a good theoretical construct, but does not reflect practical situations. In reality, a sample will have many different spins, and when placed in a static field, these spins will tend to align parallel or antiparallel to the field axis, to produce a net magnetization, M_0. As the lower energy state (parallel to the field) is more favorable, slightly more spins will occupy this state than the higher energy, antiparallel case. Before generalizing to an ensemble of spins, the expectation values for the magnetization of a single spin system should be calculated. The coefficients in eqn. (1.47) are in general complex numbers, and are described by amplitude and phase terms:

$$c_+ = |c_+|e^{\frac{1}{2}i\theta_+}, \quad c_- = |c_-|e^{\frac{1}{2}i\theta_-}, \tag{1.48}$$

where θ_+ and θ_- are the phase angles of the coefficients, and the vertical bars denote the magnitude. Therefore, the wavefunction for a single spin interacting with a static magnetic field can be written as:

$$|\psi(t)\rangle = e^{-\frac{1}{2}i(\omega_0 t-\theta_+)}|c_+||+\rangle + e^{\frac{1}{2}i(\omega_0 t+\theta_-)}|c_-||-\rangle. \tag{1.49}$$

The relations for the magnetization in the z-direction (μ_Z) and in the xy-plane (μ_+, where $\mu_+ = \mu_X + i\mu_Y$) can be obtained from eqn. (1.40), and in order to compute the expectation values, the spin angular momentum term, I, is replaced by the operator form. Consequently, the expectation value for the z-magnetization for one spin is:

$$\begin{aligned}\langle\mu_Z\rangle &= \langle\psi(t)|\gamma\hbar I_Z|\psi(t)\rangle \\ &= \frac{1}{2}\gamma\hbar\left(|c_+|^2 - |c_-|^2\right),\end{aligned} \tag{1.50}$$

and therefore, the z-magnetization depends on the difference between the probabilities of the spin being aligned parallel or antiparallel to the field. The expectation value for the magnetization in the xy-plane is:

$$\begin{aligned}\langle\mu_+\rangle &= \langle\psi(t)|\gamma\hbar I_+|\psi(t)\rangle \\ &= \gamma\hbar|c_+||c_-|e^{i\left[\omega_0 t+\frac{1}{2}(\theta_- -\theta_+)\right]} \\ &= \gamma\hbar|c_+||c_-|e^{i\omega_0 t}e^{\frac{1}{2}i(\theta_- -\theta_+)}.\end{aligned} \tag{1.51}$$

The equation for the mean value of the xy-magnetization implies a precession at the angular frequency ω_0 about the z-axis. The xy-magnetization also depends on the relative phase difference between the two states. The treatment can be expanded to obtain relations for the macroscopic magnetization of multiple spins, by taking the ensemble average of eqns. (1.50) and (1.51). The total magnetization, M_0, is a measure of the population difference between the $|+\rangle$ and $|-\rangle$ states. In an ensemble of spins, the phases are assumed to be randomly distributed, and therefore the ensemble average of $\langle\mu_+\rangle$ is zero with no perturbation other than the static magnetic field. Consequently, in thermal equilibrium, the net magnetization is solely due to M_Z, the longitudinal magnetization, and the population difference is governed by the Boltzmann distribution. M_0 is determined by the fraction of spins in the $|-\rangle$ state subtracted from the fraction of spins in the $|+\rangle$ state, multiplied by the number of spins, N. In accordance with eqn. (1.50), we can denote M_0 by:

$$M_0 = \overline{\langle \mu_Z \rangle} = \frac{1}{2}\gamma\hbar N\left(\frac{|c_+|^2 - |c_-|^2}{|c_+|^2 + |c_-|^2}\right), \tag{1.52}$$

where the horizontal line denotes the ensemble average. Each probability is given by the Boltzmann distribution:

$$\begin{gathered} |c_\pm|^2 = e^{\frac{-E_Z}{kT}}, \\ |c_+|^2 = e^{\frac{\gamma\hbar B_0}{2kT}}, \quad |c_-|^2 = e^{\frac{-\gamma\hbar B_0}{2kT}}, \end{gathered} \tag{1.53}$$

where T is the temperature in K, and k is Boltzmann's constant. Expanding the exponentials in a power series and substituting into eqn. (1.52) gives:

$$M_0 = \frac{1}{2}\gamma\hbar N\left(\frac{\frac{\gamma\hbar B_0}{kT}}{2}\right) = \frac{\gamma^2\hbar^2 B_0 N}{4kT}. \tag{1.54}$$

The term in brackets is the fraction of spins contributing to the NMR signal. Note that at a temperature of 300 K, and a static field of 4.7 T, and assuming the spins are protons, the bracketed term is calculated to be 3 x 10^{-6}, and therefore only 3 in one million spins contribute to the observable NMR signal.

1.3.2.1 Thermal Equilibrium Density Operator

The density matrix can also be calculated for the thermal equilibrium case, ρ₀, to establish a starting point for investigation of further perturbations to the spin systems. Expanding the probabilities for a one spin system (eqn. (1.53)) in terms of power series, we obtain:

$$\overline{|c_+|^2} = 1 + \frac{\gamma\hbar B_0}{2kT}, \quad \overline{|c_-|^2} = 1 - \frac{\gamma\hbar B_0}{2kT}. \tag{1.55}$$

Therefore, we need the density operator to produce the above matrix elements for ⟨+|ρ|+⟩ and ⟨−|ρ|−⟩, respectively. If we make the assumption that:

$$\tilde{\rho}_0 = e^{-\frac{\mathcal{H}_Z}{kT}}, \tag{1.56}$$

and expand the exponential in a power series, then:

$$\tilde{\rho}_0 = 1 - \frac{\mathcal{H}_Z}{kT}, \tag{1.57}$$

where 1 is the identity matrix, and substitution of eqn. (1.41) for $\mathcal{H}_Z$ yields:

$$\tilde{\rho}_0 = 1 + I_Z \frac{\gamma\hbar B_0}{kT}. \tag{1.58}$$

In general, the constant multiplying I_Z is discarded, along with the static identity matrix term, leaving the final representation of the thermal equilibrium density operator as:

$$\rho_0 = I_Z. \tag{1.59}$$

1.3.3 Radiofrequency Pulses and the NMR experiment

In a typical NMR experiment, the spins are first prepared by application of the strong, static magnetic field to produce a population difference between the spin states. The spins are then excited to a higher energy state by a radiofrequency (RF) field, $\mathbf{B_1}$, which tends to 'tip' the net magnetization away from the z-axis and into the xy-plane. In order to provide the necessary torque to tip the magnetization, the RF field must rotate in the plane orthogonal to $\mathbf{B_0}$. After $\mathbf{B_1}$ is turned off, the static field produces a torque experienced by the magnetization, causing precession about B_0 at the Larmor frequency, which can be detected by an appropriately placed receiver coil. The total magnetic field experienced by the nuclei, **B**, can be written as:

$$\mathbf{B} = \mathbf{B_1} + \mathbf{B_0} = B_1\left(\cos\omega t\ \hat{x} - \sin\omega t\ \hat{y}\right) + B_0\hat{z}, \tag{1.60}$$

where ω is defined as a positive quantity. Therefore, the Hamiltonian including both fields is:

$$\mathcal{H} = -\hbar\gamma\mathbf{B}\bullet\mathbf{I} = -\hbar\gamma\left(B_1 I_X \cos\omega t - B_1 I_Y \sin\omega t + B_0 I_Z\right). \tag{1.61}$$

The Hamiltonian is now time dependent, and therefore Schrödinger's time dependent equation must be solved to calculate wavefunction evolution. To simplify the problem, we can change into a new coordinate system that rotates concurrently with the Larmor frequency by applying the transformations:

$$\begin{aligned} \hat{x}_\rho &= \cos(\omega t)\hat{x} - \sin(\omega t)\hat{y}, \\ \hat{y}_\rho &= \sin(\omega t)\hat{x} + \cos(\omega t)\hat{y}, \end{aligned} \tag{1.62}$$

where ω is the frequency of rotation and the subscript ρ denotes the rotating frame. The z-axis is not included in the plane of rotation and therefore remains unchanged. In this frame of reference, the magnetic field is replaced by an effective magnetic field, B_{eff}:

$$\mathbf{B}_{\mathrm{eff}} = B_1\hat{x}_\rho + \left(B_0 + \frac{\omega}{\gamma}\right)\hat{z}. \tag{1.63}$$

The resonance condition occurs when B_1 rotates in a negative sense at the Larmor frequency, and therefore $\omega = -\gamma B_0$, and the resulting field reduces to:

$$\mathbf{B}_{\mathrm{eff}} = B_1\hat{x}_\rho. \tag{1.64}$$

Therefore, the Hamiltonian for an on resonance RF pulse in the rotating frame reduces to (again discarding the $\hbar$ factor):

$$\mathcal{H}_{RF} = -\gamma B_1 I_X. \tag{1.65}$$

In the rotating frame, the effect of the RF pulse is a rotation of the magnetization about the y_ρ-axis if the pulse is originally polarized along the x_ρ direction. The phase of the magnetization with respect to the z-axis after application of the RF pulse depends on the amount of time the pulse is applied. From this point on, we will assume the rotating frame of reference for all calculations.

1.3.3.1 RF Field Effects on the Density Operator

The time evolution of the density operator can be evaluated for the RF Hamiltonian described in eqn. (1.65). In the rotating frame, the Hamiltonian for the static and RF fields is time-independent, and therefore the solution has a form similar to eqn. (1.39), with substitution of $\mathcal{H}_{RF}$:

$$\begin{aligned} \rho(t) &= e^{-i\mathcal{H}_{RF}t}\rho(0)e^{i\mathcal{H}_{RF}t}, \\ &= e^{i\gamma B_1 I_X t}\rho(0)e^{-i\gamma B_1 I_X t}. \end{aligned} \tag{1.66}$$

In the thermal equilibrium case with only **B₀** acting on the spins, the density operator at t = 0 was shown in section 1.3.2.1 to be I_Z. Therefore, the solution to the density operator evolution assuming this initial condition can be calculated by successive differentiation to construct a differential equation:

$$\frac{\partial\rho}{\partial t} = (i\gamma B_1 I_X)e^{i\gamma B_1 I_X t}I_Z e^{-i\gamma B_1 I_X t} + (-i\gamma B_1)e^{i\gamma B_1 I_X t}I_Z e^{-i\gamma B_1 I_X t}I_X. \tag{1.67}$$

The I_X operators commute with the exponential I_X operators, and utilizing the commutation relation for I_X and I_Z,

$$I_Z I_X - I_X I_Z = [I_Z, I_X] = iI_Y, \tag{1.68}$$

the first derivative of the density operator can therefore be written as:

$$\frac{\partial\rho}{\partial t} = -(\gamma B_1)e^{i\gamma B_1 I_X t}I_Y e^{-i\gamma B_1 I_X t}. \tag{1.69}$$

Differentiating a second time, and utilizing commutation relations for I_Y and I_X yields:

$$\begin{aligned} \frac{\partial^2\rho}{\partial t^2} &= -(\gamma B_1)^2 e^{i\gamma B_1 I_X t}I_Z e^{-i\gamma B_1 I_X t}, \\ &= -(\gamma B_1)^2 \rho(t). \end{aligned} \tag{1.70}$$

The solution of this differential equation has the general form:

$$\rho(t) = Q_1 e^{i\gamma B_1 t} + Q_2 e^{-i\gamma B_1 t}, \tag{1.71}$$

where Q_1 and Q_2 are constants to be determined by the boundary conditions, given by:

$$\rho(0) = I_Z, \quad \text{and} \qquad (1.72)$$

$$\left.\frac{\partial \rho}{\partial t}\right|_{t=0} = -\gamma B_1 I_Y.$$

Consequently, the evolution of the density operator due to a rectangular RF pulse is:

$$\rho(t) = I_Z \cos(\theta) + I_Y \sin(\theta), \qquad (1.73)$$

where $\theta = \gamma B_1 t$ is the conventional flip angle – the amount the magnetization rotates in the yz-plane. By setting $\theta = \pi/2$, *i.e.* $t = \pi/2\gamma B_1$, the resulting density operator is equal to I_Y, and this is equivalent to the effect of the commonly known 90° pulse. If the RF field remains on for a longer period of time, *e.g.* $\theta = \pi$, a 180° pulse, the initial magnetization is inverted to the –z-axis, with a corresponding density operator form of $-I_Z$. These two particular pulses play a significant role in NMR and specifically in spectroscopy, and are used exclusively in the two general forms of spectroscopy pulse sequences, PRESS and STEAM, which will be described in later sections. This particular solution technique to the Liouville – von Neumann (50) equation can be applied to any time-independent Hamiltonian to produce time evolution for the density operator. The solutions are usually given in tabular form to avoid repetition of calculations commonly used to describe pulse sequences. For example, the transformation of the density operator under RF excitation as shown above can be written as:

$$I_Z \xrightarrow{-\gamma B_1 I_X t} I_Z \cos(\gamma B_1 t) + I_Y \sin(\gamma B_1 t), \qquad (1.74)$$

where the arrow denotes the evolution under a specific Hamiltonian. The results of common transformations are given in Appendix 2.

1.3.4 Relaxation

Based on the previous discussion of the NMR experiment, it would seem that after the magnetization is tipped into the xy-plane for detection that it remains there indefinitely. However, the energy gained by the spins from the excitation field is slowly dissipated in two separate processes called relaxation (53-56). These processes can be described by first order rate equations, and are given the characteristic times of T1 and T2, with reported values shown in Table 1-2 (57-63). The constant T1 describes the magnetization returning to 63% of its thermal equilibrium value along the z-axis before excitation, due to a loss of energy with its surroundings, or lattice. This energy cannot be recovered for further spin excitation. The loss typically involves molecular interactions such as rotations and tumblings which have a certain intrinsic frequency. When the Larmor frequency of precessing spins is in close proximity to the intrinsic frequency, the energy exchange is efficient, the relaxation is maximized and T1 has a minimal value. The solution to the rate equation for this process gives the following relation for the longitudinal magnetization, M_Z, at a later time, t:

$$M_Z(t) = M_0 + \left(M_Z(0) - M_0\right)e^{\frac{-t}{T1}}, \tag{1.75}$$

where M_0 is the thermal equilibrium value of the magnetization, as defined in eqn. (1.54). A plot of the above equation for choline at 1.5 T and 4.7 T is shown in Figure 1-2a, using T1 values from Table 1-2. The plot assumes the magnetization is completely in the transverse plane at t = 0 and therefore $M_Z(0) = 0$. T1 values tend to increase with increased magnetic field, and therefore the time for restoration of the magnetization to the thermal equilibrium orientation along the z-axis increases with increased field. Note that at typical values of 1.5 s for the repetition time (TR) used in this thesis, about 60% of M_Z

has been recovered at 4.7 T for Cho based on Fig. 1-2a, and therefore only 60% is available for further excitation in the subsequent acquisition. In a spoiled, steady-state environment (many repetitions, remnant transverse magnetization is dephased following acquisition), the optimal excitation angle (Ernst angle, α_E) may deviate from the normal 90° to achieve maximum transverse magnetization, and can be calculated from the following equation:

$$\cos(\alpha_E) = e^{\frac{-TR}{T1}}. \tag{1.76}$$

A plot of the Ernst angle vs. TR is shown in Fig. 1-2c for choline at 1.5 T and 4.7 T. At TR = 1.5 s, the Ernst angle is calculated to be 70.4° at 4.7 T, and 76.5° at 1.5 T. Consequently, a reduction in the excitation flip angle for this particular TR may produce more signal for choline at both field strengths.

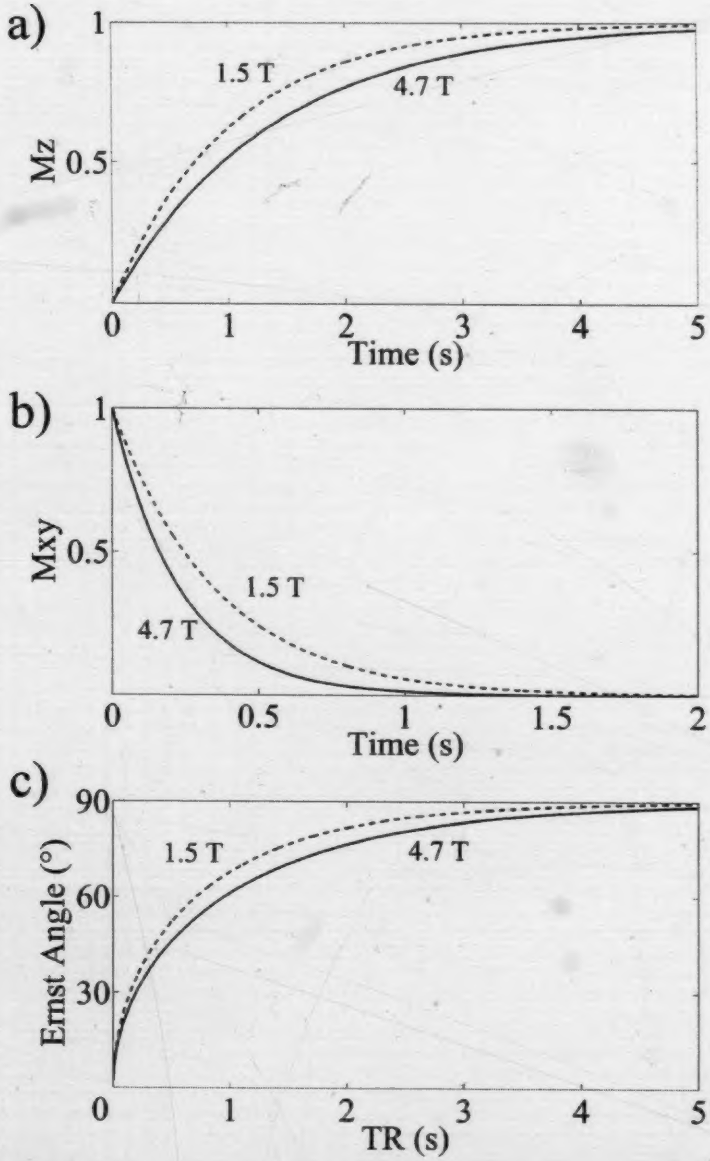

Figure 1-2: *Relaxation properties for choline at 1.5 T (dashed lines) and 4.7 T (solid). a) T1 relaxation based on eqn.* (1.75). *b) T2 relaxation based on eqn.* (1.77). *c) Ernst angle (eqn.* (1.76)*) vs TR. The maximum values of* M_Z *and* M_{XY} *have been normalized to 1 in a) and b), respectively.*

The second process, T2 or spin-spin relaxation, involves the dephasing of the spins in the xy- or transverse plane, due to loss of coherence between spins producing the net magnetization. The Larmor frequency can fluctuate between nearby spins due to variations in the local magnetic field produced by field gradients, differing sample environments, molecular vibrations or rotations, or B_0 inhomogeneities. Consequently, the spins begin to precess at different frequencies based on the local magnetic field and phase coherence is lost. The constant T2 denotes the time required for the magnetization in the transverse plane to decay to 37% of the original value. The remaining transverse magnetization, M_{XY}, after a time, t, can be expressed as:

$$M_{XY}(t) = M_{XY}(0)e^{\frac{-t}{T2}}. \tag{1.77}$$

An illustration of this equation is also provided for choline in Fig. 1-2b. T2 values tend to decrease with increased magnetic field strength, and therefore coherence in the transverse plane is lost more rapidly at higher field.

Table 1-2: *T1 and T2 relaxation times for various metabolites at 1.5 T, 3 T and 4.7 T*

Field Strength (T)	Metabolite	T1 (ms)*	T2 (ms)*
4.7	Water	1413 ± 13	58 ± 1
	N-acetylaspartate (NAA)	1324 ± 69	193 ± 25
	Creatine (Cr)	1400 ± 43	187 ± 14
	Choline (Cho)	1374 ± 25	231 ± 30
3	Water	1110 ± 40	-
	NAA	1400 ± 150	295 ± 12
	Cr	1310 ± 130	156 ± 7
	Cho	1170 ± 150	217 ± 17
1.5	Water	860 ± 30	87 ± 4
	NAA	1360 ± 60	336 ± 46
	Cr	1240 ± 100	217 ± 29
	Cho	1030 ± 150	352 ± 52

* Values are shown as mean ± standard deviation

Although relaxation provides a method for contrast in magnetic resonance imaging (MRI), it is typically a source of signal loss in spectroscopy. Most spectroscopy sequences are therefore designed to acquire a signal as quickly as possible following excitation to alleviate any relaxation losses, though specialized sequences can produce valuable signal at longer sequence timings.

1.4 Spin Interactions

The beauty of NMR spectroscopy lies in the fact that generally not all spins in a sample are identical, and differing molecular environments alter precessional frequencies – the chemical shift effect – producing complex and interesting spectra. In addition, spins can interact with neighbouring spins to induce splittings in a peak from a single proton through the process of J-coupling. These fundamental properties allow discrimination of multiple chemicals within a sample using NMR spectroscopy. Other spin interactions play a minor or insignificant role in spectral quantification in the liquid and in vivo environments and are therefore excluded from this analysis.

1.4.1 Chemical Shift

The electronic configuration of a chemical bond in a molecule influences the total magnetic field at the nuclear site, thus altering the resonance frequency (64). The static field, $\mathbf{B_0}$, induces circulations in the electron cloud surrounding the nucleus, and by Lenz's law, these circulations produce a magnetic moment opposed to $\mathbf{B_0}$, thereby reducing the local magnetic field. Figure 1-3 illustrates the magnetic fields interacting with the nucleus producing the chemical shift.

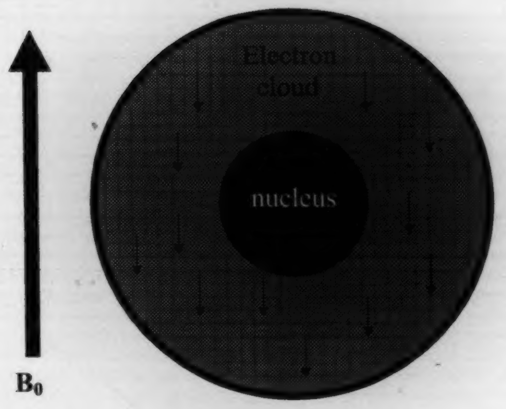

***Figure 1-3**: The applied magnetic field, $\mathbf{B_0}$, induces small, opposing magnetic fields (small arrows) in the electron cloud surrounding the nucleus, with a net effect of reducing the local magnetic field at the nuclear site.*

The perturbation of the electron cloud has a net effect of reducing the local field by a factor of σB_0, where σ is a screening constant, or shielding parameter for the nucleus. Including the electron shielding factor, the field at the nucleus, B_{nuc}, can be written:

$$B_{nuc} = (1-\sigma)B_0, \tag{1.78}$$

with a corresponding change in the Larmor equation of:

$$\omega = \gamma(1-\sigma)B_0. \tag{1.79}$$

The screening factor will also change the form of the Zeeman Hamiltonian for the interaction of a spin with a static magnetic field, *i.e.*:

$$\mathcal{H}_Z = -\gamma(1-\sigma)B_0 I_Z. \tag{1.80}$$

Therefore, two nuclei with different screening constants will have different resonance frequencies, and are displaced from each other in the spectrum. This displacement is called the chemical shift, δ, and is given by the relation:

$$\delta_{IS} = \sigma_I - \sigma_S. \tag{1.81}$$

with σ_I and σ_S being the screening constants for nuclei I and S, respectively. The chemical shift is dependent on field strength, and in order to compare spectra acquired at different fields, the parts per million (ppm) scale is used with chemical shifts measured relative to a reference compound. In general cases, the reference compound is tetramethylsilane (TMS), and is labeled as the zero point on the horizontal axis (ppm) of the spectrum, even if TMS is not included in the sample, as is the case in vivo. The relative chemical shifts can therefore be expressed as:

$$\delta(ppm) = \frac{\omega_I - \omega_{TMS}}{\omega_0} \times 10^6, \tag{1.82}$$

where ω_I is the resonance frequency of the nucleus of interest. In these ppm units, the chemical shift is constant regardless of the applied magnetic field.

1.4.1.1 Chemically Equivalent Nuclei

A unique resonance peak is produced for each chemically nonequivalent nucleus in a molecule. The equivalence of two protons can be determined by substituting a group X for one of the protons. The same product will be formed if the two protons are equivalent regardless of which proton is substituted. For example, consider methane, CH_4, as an elementary example (Figure 1-4):

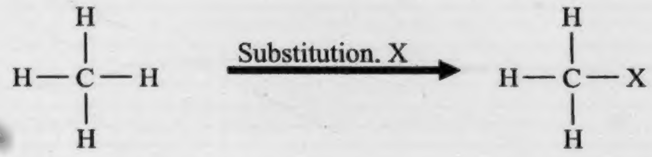

Figure 1-4: *Test for chemical equivalence of protons in methane by substitution of the arbitrary group X. All four products formed are identical.*

Upon substituting the group X for any of the protons, the same product is formed and therefore the protons in the molecule are chemically equivalent and only one resonance frequency is produced. In a more complicated example, such as 2-methyl-2-butene, the ten protons are not all chemically equivalent, as four substitution products can be formed (Figure 1-5) (65):

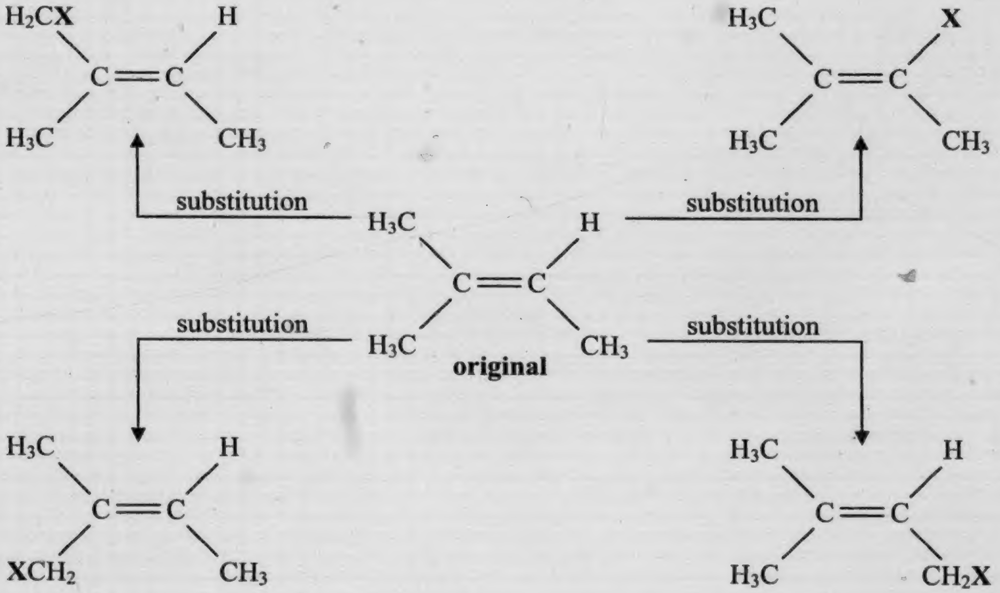

***Figure 1-5**: Test for chemically equivalent nuclei in 2-methyl-2-butene by substitution of an arbitrary group X. Four products can be formed from the ten possible substitutions.*

Consequently, protons in 2-methyl-2-butene are not all equivalent, and four different resonant frequencies result in the spectrum. This particular test can be used to determine the number of different resonance frequencies and the basis for a characteristic spectrum for a molecule. Chemical equivalence should not be confused with magnetic equivalence, which occurs when nuclei in a molecule have the same chemical shift and are equally coupled with any other nucleus in the molecule. The process of spin coupling will be discussed in the section 1.4.2.

1.4.1.2 Density Matrix Evolution: Chemical Shift

The Zeeman Hamiltonian for a nucleus, I, with resonance frequency ω_I due to the chemical shift can be written as:

$$\mathcal{H}_Z = -\gamma(1-\sigma_I)B_0 I_Z = -\omega_I I_Z, \tag{1.83}$$

and solution to the following equation produces the time evolution of the density operator at time, t:

$$\begin{aligned} \rho(t) &= e^{-i\mathcal{H}_Z t}\rho(0)e^{i\mathcal{H}_Z t} \\ &= e^{i\omega_I I_Z t}\rho(0)e^{-i\omega_I I_Z t}. \end{aligned} \tag{1.84}$$

If $\rho(0)$ contains only z-axis projection operators, the density operator will commute with the exponential operators and remain unchanged under time evolution. However, if $\rho(0)$ contains any transverse operators, *i.e.* I_X or I_Y, then the solution can be obtained in a similar manner to the time evolution during an RF pulse (section 1.3.3.1), with transformations of:

$$\begin{aligned} I_X &\xrightarrow{-\omega_I I_Z t} I_X\cos(\omega_I t) + I_Y\sin(\omega_I t), \\ I_Y &\xrightarrow{-\omega_I I_Z t} I_Y\cos(\omega_I t) - I_X\sin(\omega_I t). \end{aligned} \tag{1.85}$$

The Zeeman Hamiltonian results in the rotation of transverse spin operators at the chemically shifted resonance frequency. Consequently, nuclei with different chemical shifts will precess at different rates in the transverse plane.

1.4.2 Spin Coupling

Spins in a molecule can interact with each other through the process of spin coupling, which includes two major mechanisms: the dipolar interaction, and scalar or J- coupling. In solid NMR the dipolar interaction is prevalent, given that the magnetic dipole behavior of a nuclear spin can influence the magnetic field of neighboring spins, and alter the resonance frequency. However, this effect averages almost to zero in liquid and in vivo NMR experiments of small molecules which have rapid, random motion, and is therefore ignored in this treatment, with J-coupling being the major contributing factor to spin coupling.

The hyperfine (electron-nucleus) interaction of J-coupling was first explained by Ramsey and Purcell in 1952 (66). When two nuclei interact through J-coupling, the electrons in the chemical bond between the nuclei allow transmission of the spin state information by local magnetic field fluctuation. For example, consider two spins, A and X, coupled in a molecule by a chemical bond. Although the electrons are distributed throughout the cloud of the bond, there is a high probability that one electron is near the A nucleus, and one is near the X nucleus (Figure 1-6). The Pauli exclusion principle requires that one of the electrons in the bond have a 'spin up' orientation and the other be 'spin down'. Therefore, there are two possible configurations the A and X spins can have: both antiparallel to the corresponding bonding electron (case 2), or either A or X being parallel to the electron configuration (case 1).

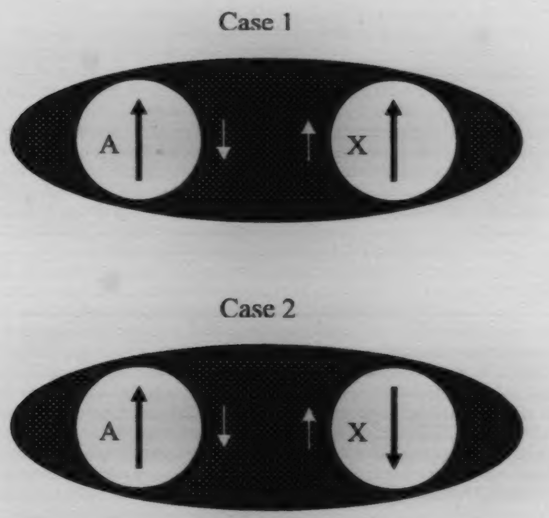

***Figure 1-6**: Two possible orientations for nuclei-electron pairs in a bond between A and X nuclei. Case 1 has one nuclei antiparallel to the corresponding electron spin, and Case 2 has both antiparallel.*

The lowest energy configuration occurs when both nuclei are antiparallel to their bonding electrons, as in Case 2, and therefore in an ensemble of AX molecules, slightly more than half possess this arrangement. If nucleus A is now excited by a radiofrequency field, the energy of transition is dependent upon the original orientation of the X spin, resulting in two transition energies or spectral frequencies. The spectral peak of the X spin will also experience a splitting due to the possible configurations of the A spins. Therefore, the orientation information of the adjacent nuclei in a molecule is transmitted via the electrons in the bond. This hyperfine interaction between the electron and nucleus can only manifest when the probability of the electron occupying the nuclear site is non-zero, and thus only bonds with s character can produce J-coupling. The coupling effect is usually small compared to the chemical shift Hamiltonian, and therefore the two frequencies are generally spaced close together, creating a multiplet (a doublet in the previous example) at the chemical shift frequency. It should be noted that the interaction is not dependent on the presence of a static magnetic field, and therefore the effect is field independent, with a coupling constant, J, describing the strength of the interaction in Hz. Because the coupling depends on the orientations of the interacting spins, the coupling Hamiltonian, $\mathcal{H}_J$, can be written as the dot product of the spin operators, multiplied by the coupling constant. For the two interacting spins in this case, we have:

$$\begin{aligned} \mathcal{H}_J &= 2\pi J_{AX}\left(\boldsymbol{A}\bullet\boldsymbol{X}\right) \\ &= 2\pi J_{AX}\left(A_X X_X + A_Y X_Y + A_Z X_Z\right), \end{aligned} \tag{1.86}$$

where **A** and **X** denote the vector spin operators, the subscripts X, Y and Z are the directions in Cartesian space and J_{AX} is the coupling constant between the A and X spins.

In general, the contributions to the energy levels of a coupled system can be evaluated by solving Schrödinger's equation for a two spin system, with the basis set defined in section 1.2.2 and using the Hamiltonian in eqn. (1.86) in addition to the Zeeman Hamiltonian for a two-spin system:

$$\mathcal{H}_Z = -\omega_A A_Z - \omega_X X_Z. \tag{1.87}$$

The derivation results in four energy levels (53):

$$\begin{aligned} E_{++} &= \frac{1}{2}\left(-\omega_A - \omega_X + \pi J_{AX}\right), \\ E_{+-} &= \frac{1}{2}\left(-\sqrt{\left(\omega_A - \omega_X\right)^2 + \left(2\pi J_{AX}\right)^2} - \pi J_{AX}\right), \\ E_{-+} &= \frac{1}{2}\left(\sqrt{\left(\omega_A - \omega_X\right)^2 + \left(2\pi J_{AX}\right)^2} - \pi J_{AX}\right), \\ E_{--} &= \frac{1}{2}\left(\omega_A + \omega_X + \pi J_{AX}\right). \end{aligned} \tag{1.88}$$

The coupling is termed strong if the coupling constant is on the same order of magnitude as the chemical shift difference, Δδ, between A and X, and the full Hamiltonian must be used to describe the interaction. However, if the chemical shift difference is much greater than J, a weak coupling approximation can be used:

$$\mathcal{H}_{J,\text{weak}} = 2\pi J_{AX} A_Z X_Z, \quad \text{when } \frac{J}{\Delta\delta} \ll 1. \tag{1.89}$$

In this case, J_{AX}^2 is negligible compared to $(\omega_A - \omega_X)^2$ in eqn. (1.88) and may be disregarded. A general rule for application of weak coupling is when $J/\Delta\delta < 0.2$ (53). The weak approximation simplifies the construction of analytical solutions to spin evolution, whereas strongly coupled systems require more rigorous evaluation. In addition, the chemical shift difference increases with increasing B_0, and therefore the strength of coupling for a particular spin group decreases.

When discussing coupled systems, the Pople notation (67) will be used, where weakly coupled spins are labeled by letters spaced far apart in the alphabet, and strongly coupled systems are closely spaced. The number of identical spins is included as a subscript. For example, a weakly coupled two spin system could be labeled an AX system, and a strongly coupled system could be labeled as an AB system. A four spin weakly coupled system with three identical spins would be represented as AX_3. In this notation, the number of interacting spins and relative strength of coupling is immediately clear for simple systems with few total nuclei, as is the case with most in vivo metabolites.

1.4.2.1 Density Matrix Evolution: Weak Coupling

For a two spin coupled system, with spins labeled A and X and resonance frequencies of ω_A and ω_X, respectively, the thermal equilibrium density operator in accordance with (1.59) is:

$$\rho(0) = A_Z + X_Z. \tag{1.90}$$

In the weak coupling regime, the coupling Hamiltonian contains only z-axis projection operators. Therefore, when solving for the evolution of the density operator (eqn. (1.39)), ρ(0) commutes with the exponential operators, and therefore the density operator remains unchanged, and the general transformation can be written as:

$$A_Z \xrightarrow{2\pi J A_Z X_Z t} A_Z, \tag{1.91}$$

similar to the chemical shift effect. The same transformation can be stated for the X spins. It should be noted that during this time evolution, the Zeeman Hamiltonian also affects the spin in accordance with the chemical shift discussion above, but the two effects can be considered independently as the Hamiltonians commute when considering weak coupling. The coupling Hamiltonian only operates on transverse components of the density operator, which can be produced by an RF excitation pulse. Although the coupling Hamiltonian is present throughout an entire pulse sequence, it is negligible compared to the RF Hamiltonian, *i.e.* $\mathcal{H}_{RF} >> \mathcal{H}_J$. Therefore, effects of J-coupling can be ignored during the time the RF pulse is on. If at some point in the spin evolution a transverse operator is produced, the solution to the time evolution equation can be evaluated in a similar manner as the RF and Zeeman Hamiltonian cases, and produces the following transformations:

$$\begin{aligned} A_X &\xrightarrow{2\pi J A_Z X_Z t} A_X \cos(\pi J_{AX} t) + 2A_Y X_Z \sin(\pi J_{AX} t), \\ A_Y &\xrightarrow{2\pi J A_Z X_Z t} A_Y \cos(\pi J_{AX} t) - 2A_X X_Z \sin(\pi J_{AX} t). \end{aligned} \tag{1.92}$$

The transverse density operator components are transformed into two terms: one comprised of an oscillating part of the original operator, and a second oscillating function which is multiplied by transverse and longitudinal spin operators. The second term also has operators of both the interacting spins, and therefore a mixing or coherence between the spins occurs. By selecting the appropriate time delay, it is possible to maximize one of the terms and eliminate the other, which can be beneficial for editing resonance signals in the final spectrum.

1.4.2.2 Some Aspects of Strong Coupling

A strongly two spin system generally has the Popel notation AB. The entire coupling Hamiltonian must be considered when the coupling constant is on the same order of magnitude as the chemical shift difference. Consequently, the coupling Hamiltonian will include the operators $A_X B_X$ and $A_Y B_Y$ in addition to the longitudinal components. The spin evolution equation cannot be solved as in the weak coupling case, as the Zeeman and coupling Hamiltonians no longer commute. It is possible however to partition the Hamiltonian into two commuting parts, $\mathcal{H}_0$ and $\mathcal{H}_1$, defined as:

$$\begin{aligned} \mathcal{H}_0 &= \varpi(A_Z + B_Z) + 2\pi J_{AB} A_Z B_Z, \\ \mathcal{H}_1 &= \delta\omega(A_Z - B_Z) + 2\pi J_{AB}(A_X B_X + A_Y B_Y), \end{aligned} \tag{1.93}$$

where $\delta\omega = (\omega_A - \omega_B)/2$ and $\varpi = (\omega_A + \omega_B)/2$. As outlined in (68), spherical angular momentum operator are used to calculate the transformation equations, defined as:

$$\breve{I}_+ = -\frac{1}{\sqrt{2}} I_+, \quad \breve{I}_- = \frac{1}{\sqrt{2}} I_-, \tag{1.94}$$

where the curved overbar denotes the spherical form of the operator. This formulation allows us to solve simple, strongly coupled systems such as the two spin AB system, and the three spin ABX system (68), using similar derivations as before. The transformation equations for a strongly coupled two spin system are listed in Appendix 3. The utility of analytical solutions decreases rapidly with increasing number of spins in strongly coupled systems, as the equations become increasingly complex and calculation intensive. Also, all spins in the system are directly involved in the calculation of system evolution for strongly coupled spins, whereas two spins in a large weak system can be treated independently because of commuting Hamiltonians. Therefore, approximations in strongly coupled spin systems are invaluable in our understanding of their properties.

1.5 Localization

In spectroscopy experiments, it is useful to limit signal acquisition to a specific area in space, particularly in in vivo experiments focused on regional studies in the brain. A single RF pulse experiment (pulse-acquire) will tip the magnetization into the xy-plane for detection, but will not allow the signal to be confined to a specified area. Therefore, it is necessary to use more than one pulse in combination with magnetic field gradients to produce the localization. Typically, the signal is acquired from an excited cube, called a voxel (volume element).

1.5.1 Gradients

Linear magnetic field gradients are used in many aspects of NMR experiments, particularly in creating spatially dependent magnetic fields for imaging and spectroscopy. The gradient always adds to the main magnetic field (**B₀**), but can vary in any linear combination of the Cartesian directions (x, y, z). If two gradients are applied at the same time with components in two different directions, the resultant gradient will be the sum of the individual gradients. In general, a point in space at a position, **r**, will experience a net magnetic field in terms of the static field and gradient field (**G**) of:

$$B = B_0 + \mathbf{G} \bullet \mathbf{r}. \tag{1.95}$$

Therefore, the resonance frequency of a given species will now be based on position:

$$\omega = \omega_0 + \gamma G r. \tag{1.96}$$

1.5.1.1 Slice Selection

A general 'hard' RF pulse will excite all frequencies in the sample, and therefore we need a way to selectively excite frequencies based on position defined by the spatially dependent magnetic field. This can be accomplished by use of a 'soft' pulse, which excites a range of frequencies, and in conjunction with the magnetic field gradient, excites a certain 'slice' within the sample. This technique is called slice selection, and the thickness of the excited slice, Δz, is related to the bandwidth (BW, inverse of duration) of the soft pulse:

$$\Delta z = \frac{BW}{\gamma G}. \tag{1.97}$$

In order to localize the signal to a three-dimensional voxel, three gradient/pulse pairs need to be applied. Only signal from spins in the intersection of the three excited slices in space will be completely refocused and detected (Figure 1-7):

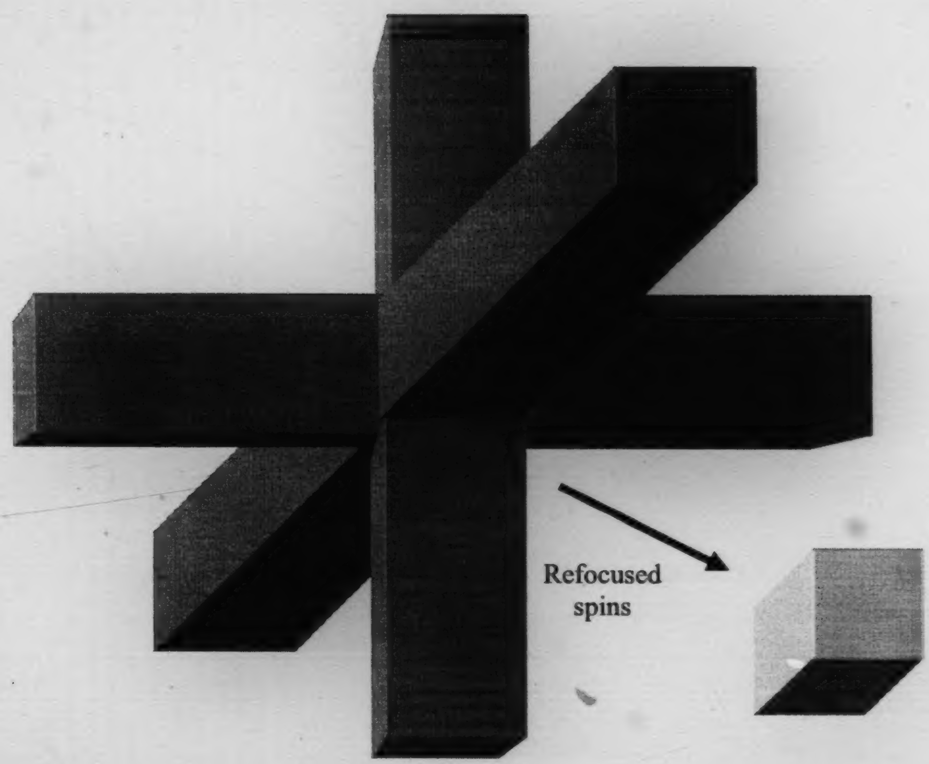

***Figure 1-7**: The gradient/pulse pairs excite three slices in space in the sample. Only spins from the intersection of the three slices are completely refocused, and the detected signal is from the intersection region, or voxel.*

Any residual signal from outlying regions is diminished by the application of crusher gradients. For the final two slices, the location of spins within a slice are encoded by a gradient before slice selection by a pulse/gradient pair, and then decoded by a similar gradient after. This has the effect of only keeping a coherent signal from spins within the selected slices, and suppressing the rest by excessive phase accumulation.

It should be noted that soft pulses have amplitudes and/or phases that vary with time, and therefore have time-dependent Hamiltonians. These pulses are usually segmented in numerical density operator simulations as many, short hard pulses, allowing the application of previously described methods to calculate spin evolution.

1.5.1.2 Gradient Effects on the Density Operator

The Hamiltonian describing the effects of a spin in a linear magnetic field gradient is similar to the static field Zeeman Hamiltonian, but includes the spatial component:

$$\mathcal{H}_g = -\gamma\, \mathbf{G} \bullet \mathbf{r} I_Z. \tag{1.98}$$

In terms of the raising and lowering operators, the effects of the gradient Hamiltonian on a spin at location **r** has the following transformations:

$$\begin{aligned} I_+ &\xrightarrow{-\gamma G r I_Z t} I_+ e^{-i\gamma G r t}, \\ I_- &\xrightarrow{-\gamma G r I_Z t} I_- e^{i\gamma G r t}, \\ I_Z &\xrightarrow{-\gamma G r I_Z t} I_Z. \end{aligned} \tag{1.99}$$

The gradient has the effect of adding a phase equal to γGrt to the spins in the sample. For multiple spin species in the sample, the effects can be treated separately for each as the Hamiltonians commute. Also, the gradient Hamiltonian commutes with the weak coupling and Zeeman Hamiltonians because of the recurrent longitudinal spin operators. The Zeeman Hamiltonian has the effect of accumulating phase differentiated in frequency space, whereas spins in a gradient will accumulate phase based on position.

1.5.2 Localization Schemes in Spectroscopy

The two most common techniques used in in vivo spectroscopy are PRESS (Point RESolved Spectroscopy) (69) and STEAM (STimulated Echo Acquisition Mode) (70).

Both sequences provide three dimensional localization of the volume of interest in the sample.

1.5.2.1 PRESS

A basic PRESS sequence is shown in Figure 1-8. The lighter grey blocks indicate slice selective gradients, while the darker blocks denote crusher or spoiler gradients. The sequence consists of a 90° pulse followed by 2 180° pulses. The 90° pulse tips the magnetization into the transverse plane, where it evolves for half of the first echo time, TE1/2. The first 180° pulse inverts the magnetization in the transverse plane, which refocuses at a point TE1 between the two 180° pulses. At this point, the magnetization begins to dephase again before the application of the final 180°, which refocuses it at a point TE1 + TE2, the starting point for acquisition. The echo times, TE1 and TE2 can be adjusted to vary the amount of time evolution the spins undergo between pulses, and can be tailored for specific target metabolites. In addition, in vivo metabolite concentrations are very small compared to the residual water signal in human brain, requiring a water suppression routine to be incorporated into the sequence. Typically, this is accomplished with spectrally selective pulses targeting the water frequency followed by crusher gradients (CHESS, CHEmical Shift Selective) (71) to dephase the water signal prior to the main PRESS sequence. The two major types of water suppression for PRESS are DRY (Drastic Reduction of water signals in spectroscopY) (72) and WET (Water suppression Enhanced through T1 effects) (73). The two methods differ in the number of CHESS pulses and the RF power for each, as well as the crusher gradient strength. DRY typically uses 3 CHESS pulses with equal power, whereas WET uses 4 CHESS pulses with varying power and subsequent gradient strength decreasing with each pulse. All experiments in this thesis use the PRESS sequence with WET water suppression exclusively for localization.

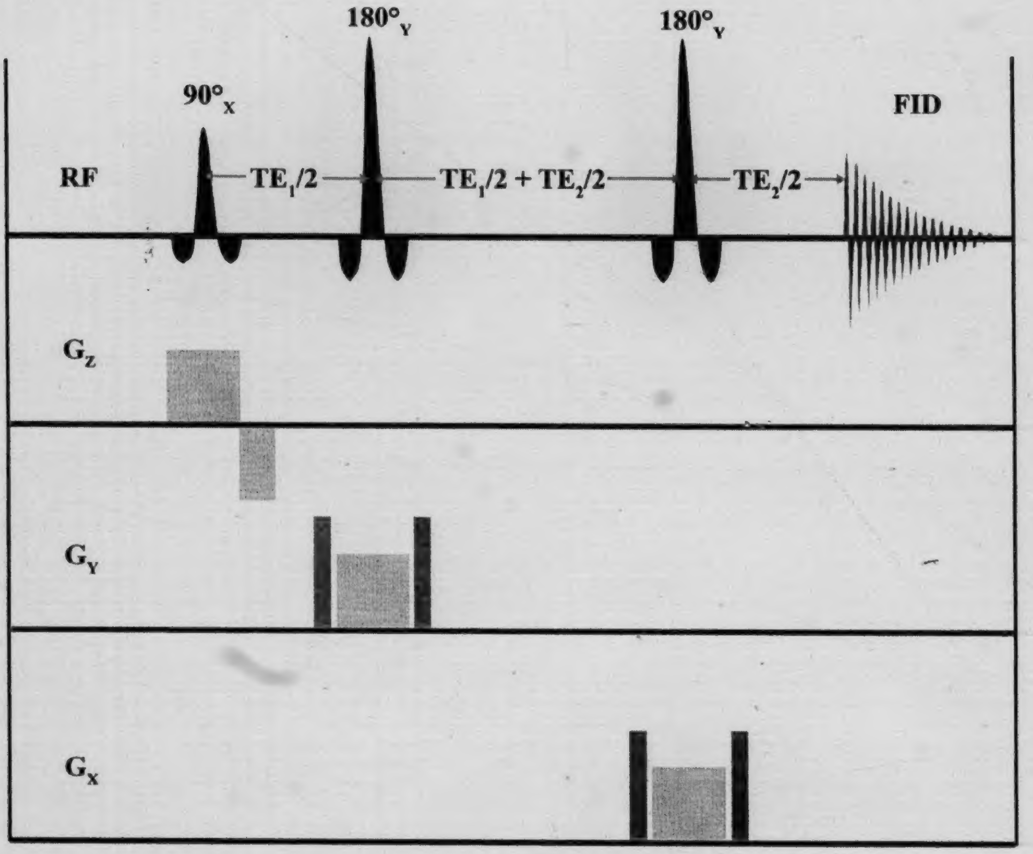

***Figure 1-8**: Diagram of a basic PRESS localization sequence.*

1.5.2.2 STEAM

The STEAM sequence is similar to PRESS in the slice selection scheme, but the two 180° pulses are replaced with 90° pulses. The spins evolve in the transverse plane for a period of TE/2 after the initial 90°, followed by a mixing time (TM) between the final 90°

pulses, and a final evolution of TE/2. The STEAM sequence creates a stimulated echo, in contrast to the spin echo in PRESS. In theory, the production of the stimulated echo results in half of the maximum total signal being lost compared to a spin echo equivalent. However, T2 relaxation is only present during the TE period, as the spins are longitudinal during the TM phase, which can effectively reduce the time for signal decay compared to the PRESS sequence.

The amount of observable magnetization following the sequence differs between PRESS and STEAM based on the flip angles of the three pulses. Defining the three arbitrary pulse flip angles as α, β, and γ and ignoring relaxation and signal modulation due to timing parameters, the response of the magnetization to the sequence can be calculated in a qualitative manner. In both PRESS and STEAM, the first pulse tips the magnetization toward the transverse plane, with the amount of transverse magnetization dependent on $\sin(\alpha)$. Each of the subsequent refocusing pulses in PRESS produce a cosine dependence, and therefore the final observable magnetization can be described by:

$$M_{XY,PRESS} = M_0 \sin(\alpha)\cos(\beta)\cos(\gamma). \tag{1.100}$$

In STEAM, the final two pulses have the same effect as the initial excitation pulse, and therefore:

$$M_{XY,STEAM} = \frac{M_0}{2}\sin(\alpha)\sin(\beta)\sin(\gamma). \tag{1.101}$$

The factor of 1/2 in eqn. (1.101) is due to the production of a stimulated echo in STEAM in contrast to the spin echo in PRESS. In typical situations, $\beta = \gamma = 2\alpha$ in PRESS, and $\beta = \gamma = \alpha$ in STEAM, producing the following relations:

$$M_{XY,PRESS} = M_0 \sin(\alpha)\cos^2(2\alpha),$$
$$M_{XY,STEAM} = \frac{M_0}{2}\sin^3(\alpha). \quad (1.102)$$

This equation is illustrated in Figure 1-9, with M_0 normalized to 1.

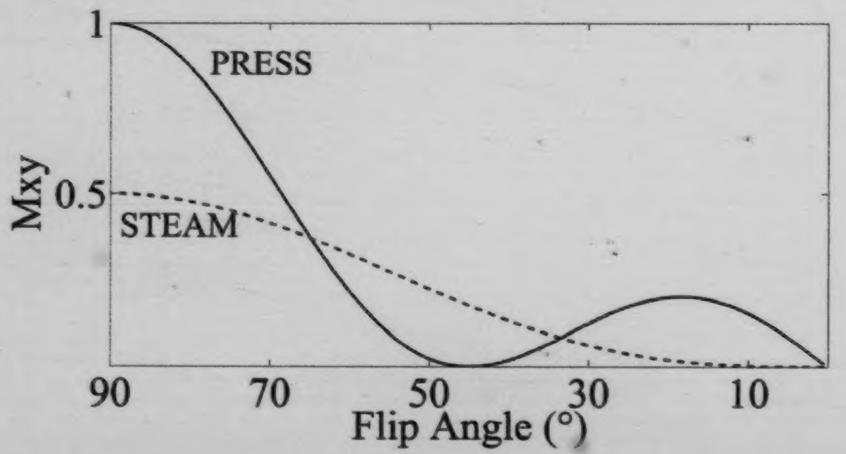

Figure 1-9: *Flip angle dependence of the transverse magnetization following the PRESS (solid line) and STEAM (dashed) sequences based on eqn.* (1.102). *Relaxation effects are considered in the analysis. The maximum value of M_{XY} is M_0, which has been normalized to 1.*

The decline in signal is rapid for the PRESS sequence due to the 5th order trigonometric terms in the expansion of eqn. (1.102). At higher values of α ($\alpha > 65°$) however, the signal resulting from the PRESS sequence remains greater than STEAM.

1.5.2.3 Spectroscopic Imaging

Spectroscopic imaging is a combination of single voxel (SV) spectroscopy and imaging, which produces multiple, localized spectra in one sequence. This is accomplished by exciting a large region in the sample or volume of interest (VOI) with a PRESS or STEAM sequence, and introducing phase encoding before acquisition (see Figure 1-10).

The phase encode gradients effectively divide the VOI into voxels based on position. Metabolic maps can be constructed to investigate the variation of a particular metabolite over a large region. Note the water suppression segment has been omitted from the diagram below.

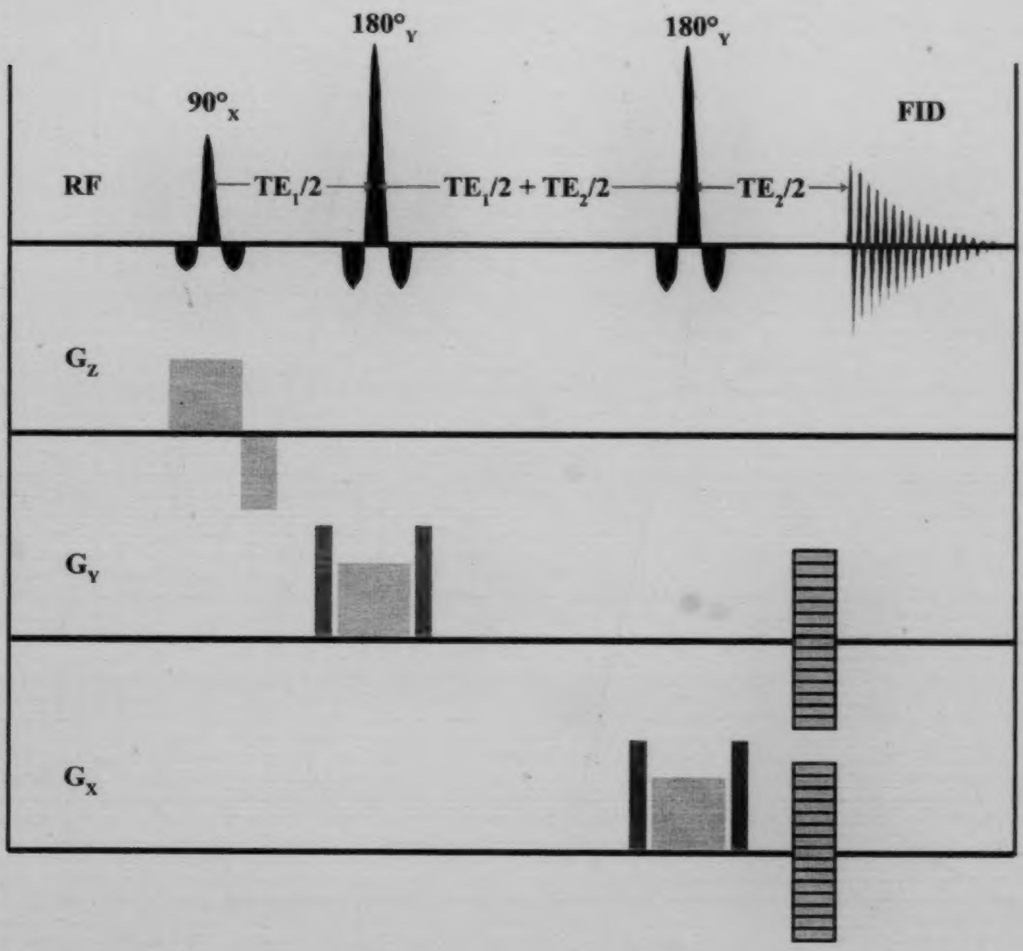

***Figure 1-10**: Spectroscopic imaging sequence based on PRESS. The addition of phase encode gradients (segmented rectangles) near the end of the sequence allows multiple spectra to be acquired from localized voxels.*

1.6 Techniques for Evolution of a Weakly Coupled System Under PRESS

The relevant Hamiltonians describing the PRESS and STEAM sequences have been illustrated in previous sections, along with the density operator evolution for each Hamiltonian. At this point, it is instructive to determine the effects of a SV experiment on spin evolution. For example, the simple, weakly coupled AX system will be used with a coupling constant J_{AX} and resonant frequencies of ω_A and ω_X. Because there is only one coupling constant for this particular system, the AX subscript will be dropped for brevity, however, it is necessary in more complex systems to differentiate between the different coupling constants. The PRESS sequence can be segmented into a number of sections described by different Hamiltonians (see Figure 1-11). After each section, the density operator can be calculated and used in subsequent sections. At any point in the sequence, particularly at the end, the observable magnetization, M_+, can be calculated using eqn. (1.29), where the expectation value we want to calculate is the transverse magnetization, proportional to $A_+ + X_+$, *i.e.*:

$$M_+ \propto \langle A_+ + X_+ \rangle = Tr\left[\rho\left(A_+ + X_+\right)\right]. \tag{1.103}$$

To simplify the treatment, precise hard pulses will be used with exact flip angles of 90° and 180°, and signal losses due to relaxation are ignored. Also, the raising and lowering operators will be used instead of the Cartesian x and y operators. The transformations used in the calculations can be found in Appendix 2.

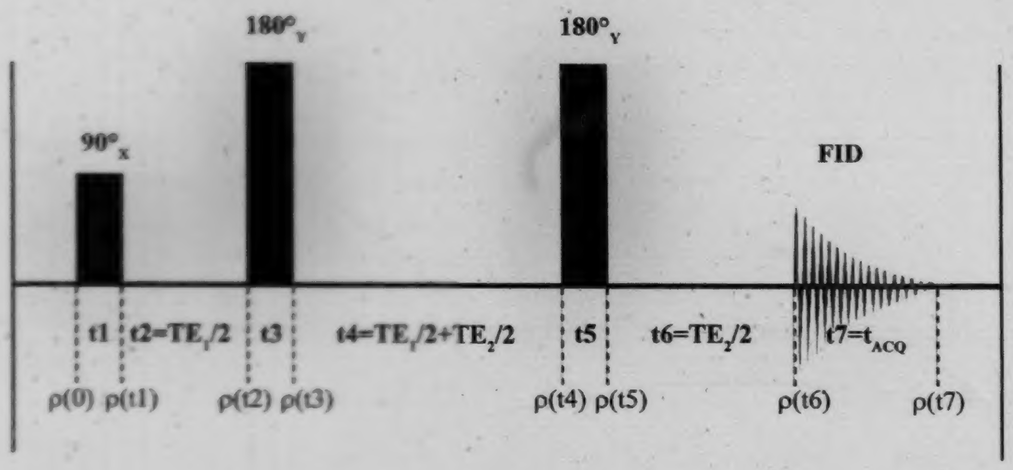
180°$_Y$
180°$_Y$
90°$_X$
FID
t1
t2=TE$_1$/2
t3
t4=TE$_1$/2+TE$_2$/2
t5
t6=TE$_2$/2
t7=t$_{ACQ}$
ρ(0) ρ(t1)
ρ(t2) ρ(t3)
ρ(t4) ρ(t5)
ρ(t6)
ρ(t7)

Figure 1-11: Timing diagram for a standard PRESS sequence. The relevant density operators are listed below each timing interval.

The starting point for the calculation is the thermal equilibrium density operator, given by a summation of density operators for each spin – in this case, of A_Z and X_Z. In general, for a system of N spins, the collective action of projection operators along a particular axis can be defined as a total momentum operator (74):

$$F_Z = I_{Z1} + I_{Z2} \ldots = \sum_{k=1}^{N} I_{Zk}, \tag{1.104}$$

where the numerical subscript denotes a particular spin. The action of the RF Hamiltonian can be described by a similar approach. In this manner, the equilibrium density matrix for the AX system is given by:

$$\rho(0) = F_Z = A_Z + X_Z, \tag{1.105}$$

with a corresponding density matrix, σ(0), of:

$$\sigma(0)=\begin{bmatrix}1&0&0&0\\0&0&0&0\\0&0&0&0\\0&0&0&-1\end{bmatrix}. \tag{1.106}$$

As alluded to earlier, the diagonal elements of σ are population terms, and therefore, at thermal equilibrium, we expect the density matrix to be comprised of two population entries for both spins having 'spin up' or 'spin down' orientations. The random phases of an ensemble of spins ensures that the probabilities of states having combinations of spin up or spin down are summed to zero.

1.6.1 The First 90° Pulse

The RF pulse section is governed by the Hamiltonian in eqn. (1.65). For a 90° pulse polarized in the x-direction, $t1 = \pi/2\gamma B_1$, and therefore the density operator immediately following the pulse is:

$$\rho(t1)=\frac{1}{2i}\left(A_+ - A_- + X_+ - X_-\right). \tag{1.107}$$

This step assumes that both species are irradiated equally and that $\mathcal{H}_{RF} >> \mathcal{H}_Z$ such that the chemical shift evolution and scalar coupling effects can be ignored. At this point, the density matrix, σ(t1), has the following form:

$$\sigma(t1)=\frac{i}{2}\begin{bmatrix}0&-1&-1&0\\1&0&0&-1\\1&0&0&-1\\0&1&1&0\end{bmatrix}. \tag{1.108}$$

The population elements in σ have been removed, and new, off-diagonal elements produced. Returning to the +/– representation of the two spin system, we can investigate possible interpretations for these elements. For example, the element $\sigma_{21}(t1)$ can be written as:

$$\sigma_{21}(t1) = \langle ++|\rho|+-\rangle = -1. \tag{1.109}$$

The fact that this element is non-zero suggests an interaction (coherence) between the two spin states, and only involves one spin, and consequently a change equal to one quantum of energy. This type of coherence between the states involving only one spin is called single quantum coherence, or SQC (74). Thus, the entire thermal equilibrium density matrix has been converted to SQCs following the 90° pulse. A coherence between two or more spins is denoted as MQC, or multiple quantum coherence. Only SQCs contribute to observable magnetization. The expectation value for the magnetization at this point is:

$$M_+ \propto \langle A_+ + X_+ \rangle = 2i. \tag{1.110}$$

The magnetization is at the maximum absolute value of 2 for a two spin system, and has a 90° phase shift from the measured plane.

1.6.2 The First Evolution Period

The spins are now allowed to evolve in the static magnetic field for a period t2 = 1/2 TE1, with Hamiltonian contributions from the Zeeman and J-coupling interactions, *i.e.*:

$$\mathcal{H}_{t2} = \mathcal{H}_Z + \mathcal{H}_J = -\omega_A A_Z - \omega_X X_Z + 2\pi J A_Z X_Z. \tag{1.111}$$

All parts of the Hamiltonian commute, allowing us to compute the relevant time evolution during the t2 period individually. Dealing with the J-coupling part first and applying the necessary transformations gives:

$$\begin{aligned}\rho_J(t2) = \frac{1}{2i}&(A_+ - A_- + X_+ - X_-)\cos(\pi Jt2)\\ &+(A_- - A_+)X_Z\sin(\pi Jt2)+(X_- - X_+)A_Z\sin(\pi Jt2),\end{aligned} \tag{1.112}$$

where ρ_J denotes the density operator after the J-coupling evolution. The operators, A_-X_Z, A_+X_Z, X_-A_Z and X_+A_Z also produce SQCs, but are termed antiphase operators as they do not contribute immediately to the observable magnetization, but can however after J-coupling evolution. For example, the operator A_+X_Z has matrix form:

$$A_+X_Z = \frac{1}{2}\begin{bmatrix} 0 & 0 & 1 & 0 \\ 0 & 0 & 0 & -1 \\ 0 & 0 & 0 & 0 \\ 0 & 0 & 0 & 0 \end{bmatrix}, \tag{1.113}$$

and upon taking the trace as in eqn. (1.103), the observable magnetization is zero.

The second part of the transformation is due to the Zeeman Hamiltonian, and produces the complete density operator at the end of the t2 period:

$$\begin{aligned}\rho(t2) = \frac{1}{2i}&\left(A_+e^{-i\omega_A t2} - A_-e^{i\omega_A t2} + X_+e^{-i\omega_X t2} - X_-e^{i\omega_X t2}\right)\cos(\pi Jt2)\\ &+\left(A_-e^{i\omega_A t2} - A_+e^{-i\omega_A t2}\right)X_Z\sin(\pi Jt2)\\ &+\left(X_-e^{i\omega_X t2} - X_+e^{-i\omega_X t2}\right)A_Z\sin(\pi Jt2).\end{aligned} \tag{1.114}$$

Effectively, the Zeeman Hamiltonian causes a rotation of the spin operators at the relevant Larmor frequency. The Zeeman and J-coupling Hamiltonians do not produce new elements in the density matrix, but add oscillations at the Larmor and coupling constant frequencies.

1.6.3 The First 180° Pulse

The subsequent 180° pulse 'flips' the magnetization in the xy-plane, and converts '+' operators to '–' operators and vice versa, while tipping longitudinal operators to the opposite axis. Consequently, no new entries are produced in the density matrix. Note that in terms of the tables, the pulse is polarized along the y-direction and has a flip angle of $\pi/\gamma B_1$. Applying the transformations, the density operator following the pulse is:

$$\begin{aligned}\rho(t4) &= \frac{1}{2i}\left(-A_{-}e^{-i\omega_A t2} + A_{+}e^{i\omega_A t2}\right)\cos(\pi J t2) \\ &+ \frac{1}{2i}\left(-X_{-}e^{-i\omega_X t2} + X_{+}e^{i\omega_X t2}\right)\cos(\pi J t2) \\ &+ \left(A_{+}e^{i\omega_A t2} - A_{-}e^{-i\omega_A t2}\right)X_Z \sin(\pi J t2) \\ &+ \left(X_{+}e^{i\omega_X t2} - X_{-}e^{-i\omega_X t2}\right)A_Z \sin(\pi J t2).\end{aligned} \tag{1.115}$$

1.6.3.1 Spoiler Gradients

In a general spectroscopy sequence, spoiler gradients are placed around the 180° pulses to ensure clean refocusing. The overall effects of the spoiler gradients remove terms from the density operator, and do not have a lasting effect on the evolution of the spins. The spoiler gradients add a phase evolution to the transverse operators A_+, A_-, X_+ and X_-, in a similar manner to the effect of the Zeeman Hamiltonian. In this particular example, it is not necessary to include the spoilers as perfect pulses are assumed. If a refocusing pulse other than 180° is used, each operator will be transformed into varying amounts of the three projection operators, depending on the flip angle. Using the A_+ operator as an example, the effect of the spoiler gradient is:

$$A_+ \xrightarrow{\theta t_G} A_+ e^{-i\theta t_G}, \tag{1.116}$$

where $\theta = -\gamma Gr$, and t_G is the time the gradient is left on. Consequently, the phase angle the spins accumulate due to the gradient is determined by the t_G period. Following an arbitrary pulse polarized in the y-direction, we have:

$$A_+ e^{-i\theta t_G} \xrightarrow{\phi I_Y} e^{-i\theta t_G} \left\{ \frac{1}{2}\left[A_+(1+\cos\phi) - A_-(1-\cos\phi)\right] - iA_Z \sin\phi \right\}, \tag{1.117}$$

where $\phi = -\gamma B_1 t$. The second spoiler gradient follows the pulse and has the same strength and duration as the first, giving the final expression for the spoiler gradient/pulse evolution:

$$\begin{aligned} A_+ \xrightarrow{total} & e^{-i\theta t_G} \left\{ \frac{1}{2}\left[A_+ e^{-i\theta t_G}(1+\cos\phi) - A_- e^{i\theta t_G}(1-\cos\phi)\right] - iA_Z \sin\phi \right\}, \\ &= \frac{1}{2}\left[A_+ e^{-i2\theta t_G}(1+\cos\phi) - A_-(1-\cos\phi) - iA_Z e^{-i\theta t_G} \sin\phi\right]. \end{aligned} \tag{1.118}$$

The A_+ term is destroyed by excessive phase accumulation (2θ) and does not refocus. The A_Z operator is only affected by one gradient, and could possibly produce observable magnetization if a subsequent, equal spoiler reverses the phase and an RF pulse converts it to A_+ and A_-. However, spoiler gradient pairs for different 180° pulses are typically in different directions corresponding to the current slice selection, and therefore this particular A_Z term should not be refocused. Only the A_- term remains due to phase cancellation, multiplied by the $(1 - \cos\phi)$ scaling factor determined by the flip angle.

Thus, non-ideal pulses can result in significant signal loss if the refocusing flip angle is not near 180°.

1.6.4 The Remainder of the Sequence

Following the first 180°, the spins evolve for a period of $(TE_1 + TE_2)/2$ in which in phase magnetization is converted to antiphase magnetization and vice versa. The second 180° pulse flips the magnetization about the y-axis again, and the final evolution for $TE_2/2$ determines the available observable magnetization at the end of the sequence. The expectation value for the observable magnetization at the beginning of acquisition is:

$$M_+ \propto 2i\cos\left(\pi JTE_1 + \pi JTE_2\right), \tag{1.119}$$

and if the PRESS sequence is symmetric, *i.e.* $TE_1 = TE_2$, and $TE_1 + TE_2 = TE$, then:

$$M_+ \propto 2i\cos\left(\pi JTE\right). \tag{1.120}$$

This equation is very similar to eqn. (1.110), except for the oscillating cosine term dependent on the coupling constant for the system and the choice of TE. During acquisition, the spins will continue to evolve under the Zeeman and J-coupling Hamiltonians, such that the observable magnetization at some time, t_p, will have an expectation value of:

$$M_+ \propto \frac{1}{2}i\left(e^{i\omega_A t_p} + e^{i\omega_X t_p}\right)\cos\left(\pi Jt_p + \pi JTE_1 + \pi JTE_2\right). \tag{1.121}$$

By sampling the magnetization many points during the t_p period, we can calculate an FID for this particular system, and determine the spectral information (Fig. 1-12)

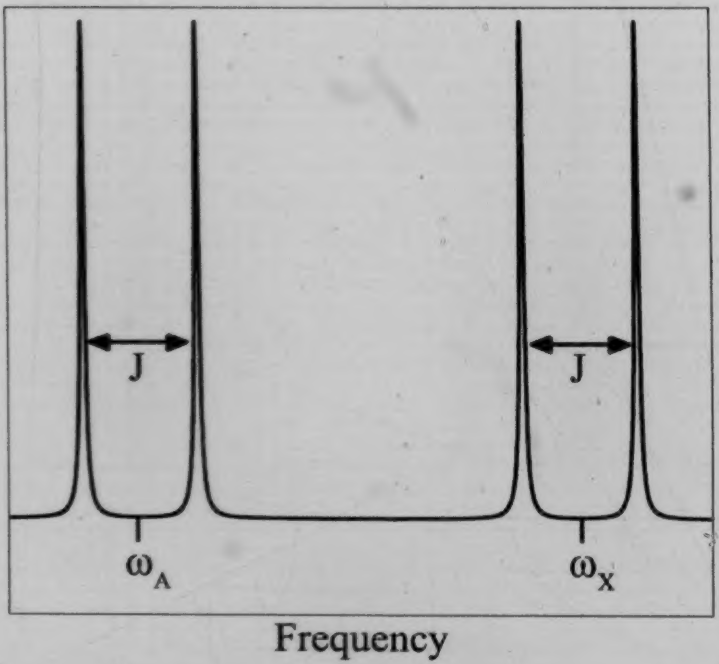

***Figure 1-12**: Sample spectrum of an AX weakly coupled system.*

As discussed in section 1.4.2, both the A and X peaks are split by J-coupling into doublets. Within a doublet, the individual peaks are spaced in frequency by the coupling constant, J. Depending on the strength B_0, the chemical shift difference ($\omega_A - \omega_X$) varies and consequently the spacing between the doublets. Also, depending on J and the choice of TE, the intensity and phase of the peaks will vary according to eqn. (1.121).

1.6.5 Contrasts to Strong Coupling

Acquisition following the 90° pulse and an evolution period t2 (following section 1.6.2) for the weakly coupled system in accordance with eqns. (1.103) and (1.114) is calculated to be:

$$M_+ \propto \frac{1}{2} i\left(e^{i\omega_A t2} + e^{i\omega_X t2}\right)\cos(\pi J t2), \tag{1.122}$$

and expansion of the cosine term gives:

$$\begin{aligned} M_+ &\propto \frac{1}{4} i\left(e^{i\omega_A t2} + e^{i\omega_X t2}\right)\left(e^{i\pi J t2} + e^{-i\pi J t2}\right) \\ &= \frac{1}{4} i\left(e^{i(\omega_A+\pi J)t2} + e^{i(\omega_A-\pi J)t2} + e^{i(\omega_X+\pi J)t2} + e^{i(\omega_X-\pi J)t2}\right). \end{aligned} \tag{1.123}$$

The frequencies of the spectral lines are therefore $\omega_A \pm \pi J$ and $\omega_X \pm \pi J$, with all having equal intensity (Figure 1-12).

In the case of an AB strongly coupled system, the A_Z and B_Z thermal equilibrium operators respond the same to the initial 90°, and evolve under the $\mathcal{H}_0$ and $\mathcal{H}_1$ Hamiltonians during the t2 period to yield an observable signal of:

$$\begin{aligned} M_+ \propto &\left(1 - \pi\frac{J_{AB}}{\Lambda}\right)\left(e^{i(\bar{\omega}+\Lambda+\pi J_{AB})t} + e^{i(\bar{\omega}-\Lambda-\pi J_{AB})}\right) \\ &+ \left(1 + \pi\frac{J_{AB}}{\Lambda}\right)\left(e^{i(\bar{\omega}+\Lambda-\pi J_{AB})t} + e^{i(\bar{\omega}-\Lambda+\pi J_{AB})}\right) \end{aligned} \tag{1.124}$$

where $\delta\omega = (\omega_A - \omega_B)/2$, $\bar{\omega} = (\omega_A + \omega_B)/2$, $\Lambda = \sqrt{(\delta\omega)^2 + (\pi J)^2}$, and J_{AB} is the strong coupling constant. In this case, the lines have differing intensities depending on their frequency, unlike the weak coupling case. An example of a spectrum for a strongly coupled AB system is shown in Figure 1-13.

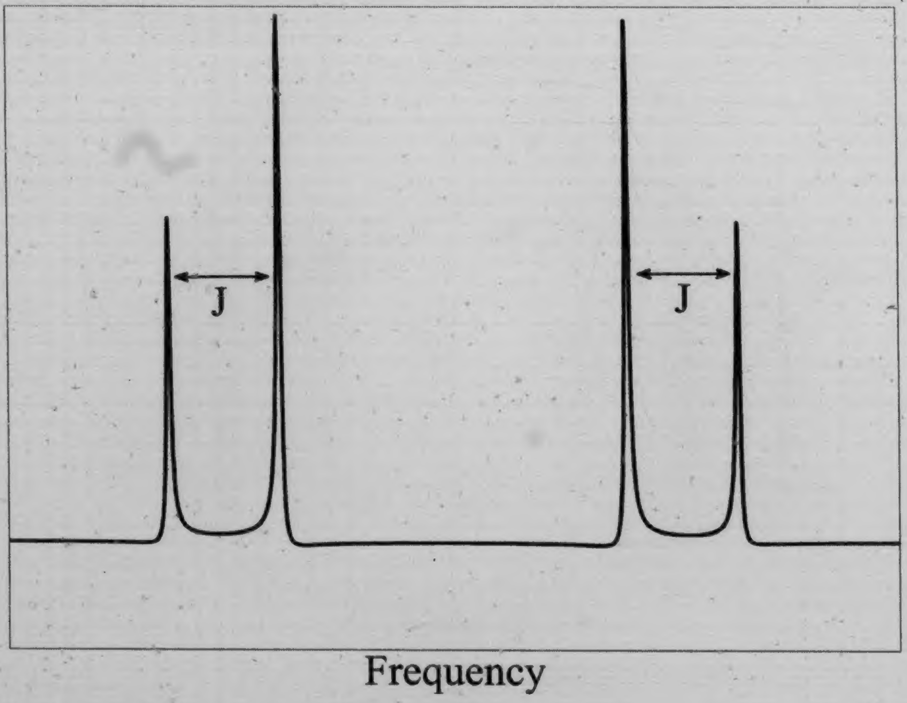

Figure 1-13: *Sample spectrum of a strongly coupled AB system*

It is apparent from eqn. (1.124) that the outermost peaks are always separated from the innermost peaks by a value of J.

1.6.6 Other PRESS Aspects and Numerical Simulation

In contrast to STEAM, it should be noted that in a properly spoiled standard PRESS sequence, MQCs (operator terms involving A_+X_+, A_-X_-, A_-X_+, and A_+X_-) are not produced, and therefore only SQCs can contribute to the observable magnetization. The amount of signal available at the end of the sequence also depends heavily on the choice of flip angle for the pulses, as the signal can suffer significantly from non-ideal pulses. The complexity of the analytical approach increases incredibly with increased number of spins in the system, but provides valuable information between two interacting spins in any system.

Most interesting in vivo metabolites have more than two spins and some aspect of strong coupling, and therefore numerical simulations are generally used to describe these interactions. In the case of this thesis, an in-house, MATLAB numerical spin simulation program (75) was used to determine spin response to the PRESS sequence. The program partitions the sequence into segments characterized by a pulse, time delay or gradient, and calculates the density matrix based on the time-independent Hamiltonian for each segment. The density matrix is then used for the calculation of the subsequent segment. At the end of the sequence, a spectrum can be calculated from the FID produced. In the case of a segment with a time-dependent Hamiltonian, such as a soft RF pulse, it is further divided into multiple, short sections which can then be treated as time-independent. The simulator can incorporate strong and weak coupling effects and up to six spins, as well as multiple TEs and B_0 field strengths.

1.7 Common In Vivo Metabolites

The in vivo metabolites important to this project are listed below, in acid form (if applicable). All metabolites have sufficient in vivo concentrations to be NMR visible, albeit at higher field strengths in some cases. The stick and three dimensional forms for each are provided to illustrate the locations of protons detected by NMR spectroscopy. Also, spectra are shown using a short PRESS sequence (TE = 20 ms) simulation for each metabolite, with an exponential line broadening filter of 1 Hz applied. This linewidth is not typical in in vivo experiments, but is used to better demonstrate the multiplicity of peaks in coupled systems. Chemical shifts and J-coupling constants are also listed for each metabolite (76). Table 1-3 lists the range of metabolite concentrations in normal human brain derived from NMR spectroscopy and other methods, as reported in the literature and compiled in Ref. (76), and includes other metabolites not studied directly in this thesis. Figure 1-14 shows a high resolution spectrum obtained at 14.1 T from rat brain extract (76).

Aspartate (Asp)

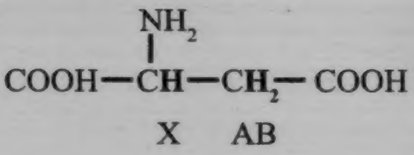

$$\mathrm{COOH-\underset{X}{\overset{NH_2}{\overset{|}{CH}}}-\underset{AB}{CH_2}-COOH}$$

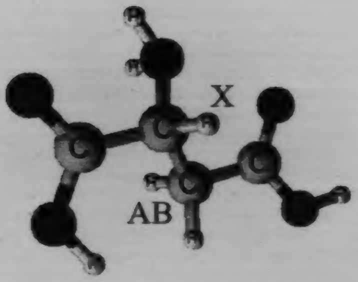

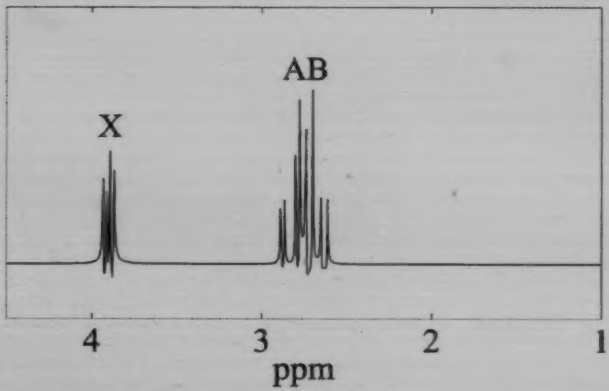

ω (ppm)	J (Hz)
A 2.801	AB -17.426
B 2.653	AX 9.107
X 3.891	BX 3.647

Choline (Cho)

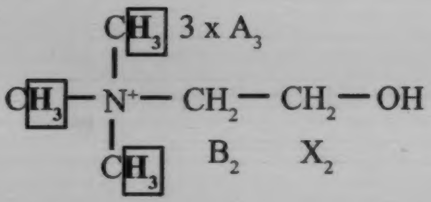

$$\mathrm{C\boxed{H_3}-\overset{\overset{C\boxed{H_3}\ 3\ x\ A_3}{|}}{\underset{\underset{C\boxed{H_3}}{|}}{N^+}}-\underset{B_2}{CH_2}-\underset{X_2}{CH_2}-OH}$$

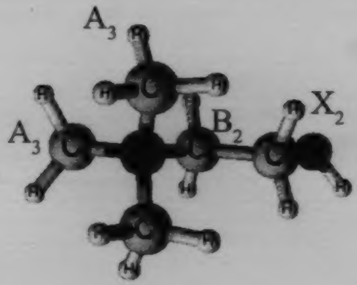

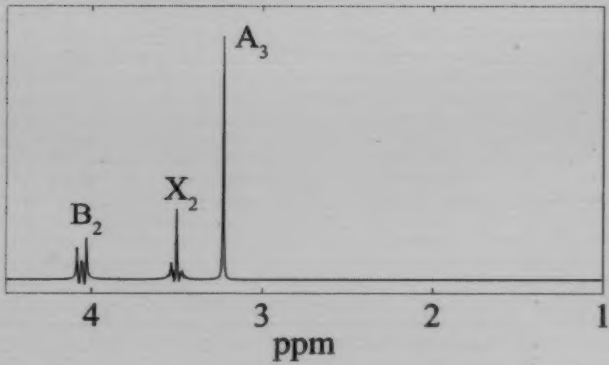

ω (ppm)	J (Hz)
A_3 3.185	B_1X_1 3.140
B 4.050	B_1X_2 6.979
X 3.506	B_2X_1 3.168
	B_2X_2 7.011

Citrate (Cit)

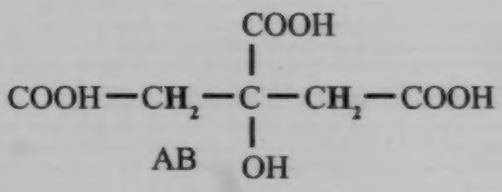

$\mathrm{COOH-CH_2-\overset{COOH}{\underset{OH}{C}}-CH_2-COOH}$

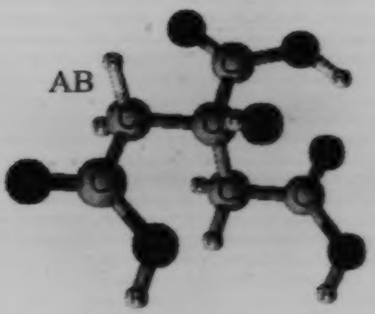

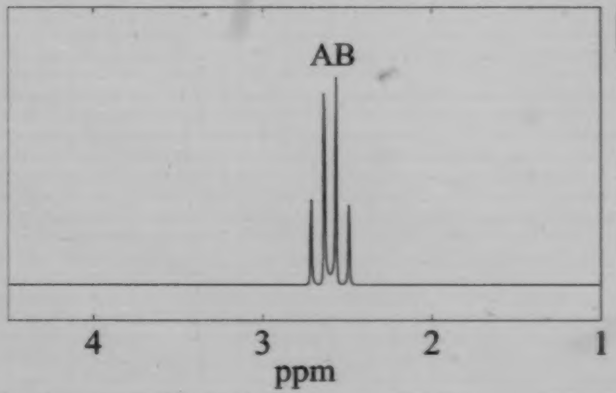

ω (ppm)	J (Hz)
A 2.536	AB 15.4
B 2.663	

Creatine (Cr)

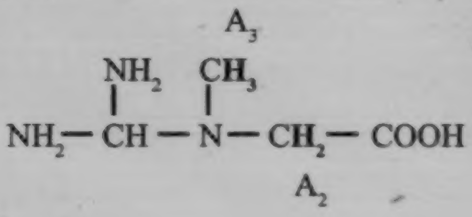

$\mathrm{NH_2-\overset{NH_2}{CH}-\overset{CH_3}{N}-CH_2-COOH}$

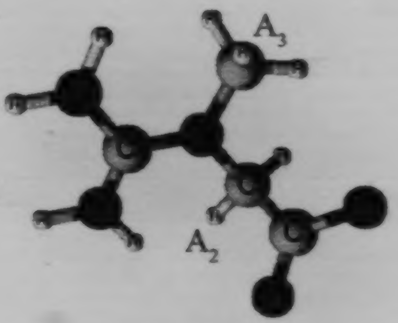

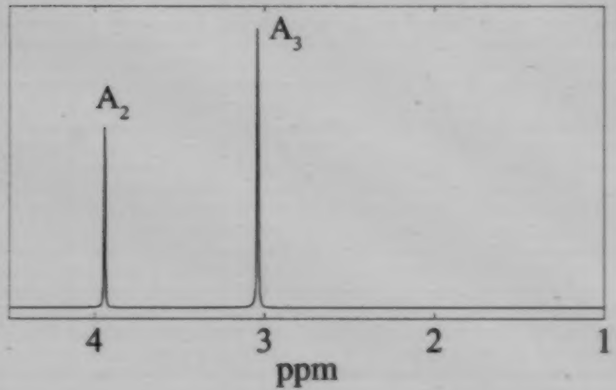

ω (ppm)	J (Hz)
A_3 3.027	-
A_2 3.913	

γ-Aminobutyric acid (GABA)

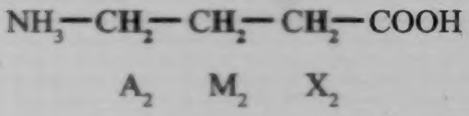

$$\mathrm{NH_3-\underset{A_2}{CH_2}-\underset{M_2}{CH_2}-\underset{X_2}{CH_2}-COOH}$$

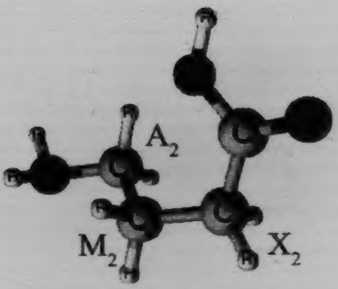

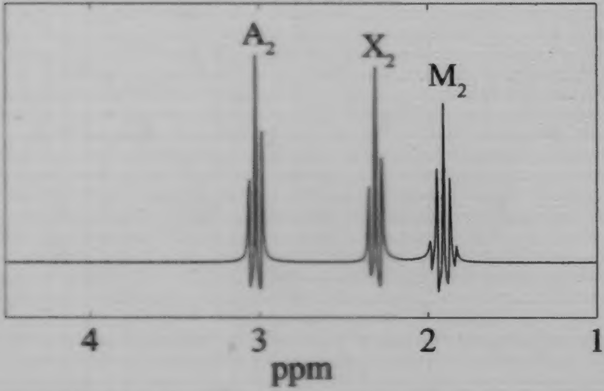

ω (ppm)		J (Hz)	
A	3.013	A_1M_1	5.372
M	1.889	A_1M_2	7.127
X	2.284	A_2M_1	10.578
		A_2M_2	6.982
		M_1X_1	7.755
		M_1X_2	7.432
		M_2X_1	6.173
		M_2X_2	7.933

Glutamate (Glu)

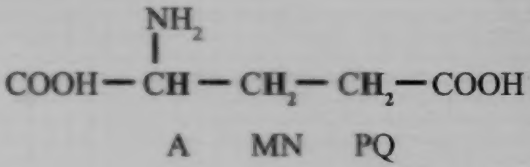

$$\mathrm{COOH-\underset{A}{\overset{NH_2}{\overset{|}{CH}}}-\underset{MN}{CH_2}-\underset{PQ}{CH_2}-COOH}$$

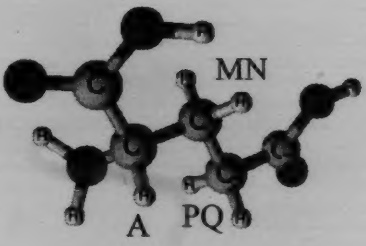

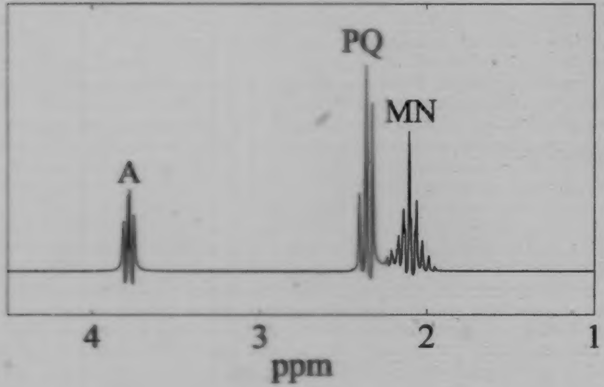

ω (ppm)		J (Hz)	
A	3.743	AM	7.331
M	2.038	AN	4.651
N	2.120	MN	-14.849
P	2.338	MP	6.413
Q	2.352	MQ	8.406
		NP	8.478
		NQ	6.875
		PQ	-15.915

Glutamine (Gln)

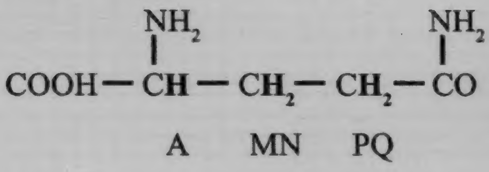

$$\mathrm{COOH-\underset{A}{\overset{NH_2}{CH}}-\underset{MN}{CH_2}-\underset{PQ}{CH_2}-\overset{NH_2}{CO}}$$

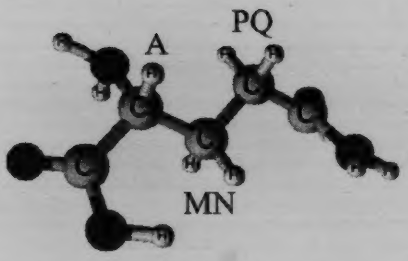

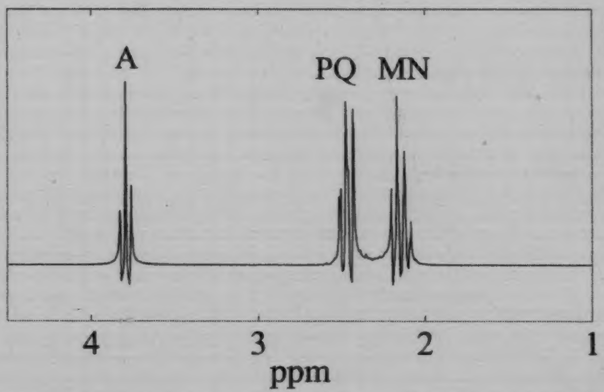

ω (ppm)		J (Hz)	
A	3.753	AM	5.847
M	2.129	AN	6.500
N	2.109	MN	-14.504
P	2.432	MP	9.165
Q	2.454	MQ	6.347
		NP	6.324
		NQ	9.209
		PQ	-15.371

Lactate (Lac)

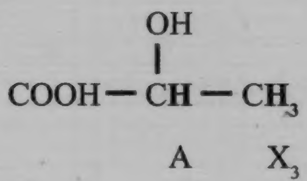

$$\mathrm{COOH-\underset{A}{\overset{OH}{CH}}-\underset{X_3}{CH_3}}$$

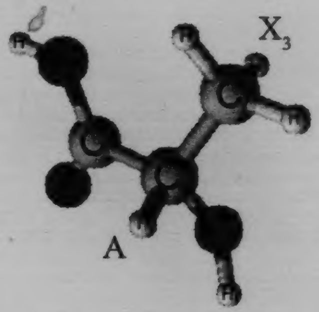

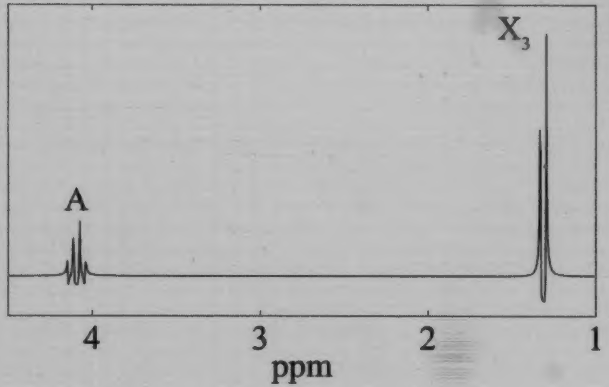

ω (ppm)		J (Hz)	
A	4.097	AX	6.933
X_3	1.314		

myo-Inositol (mI)

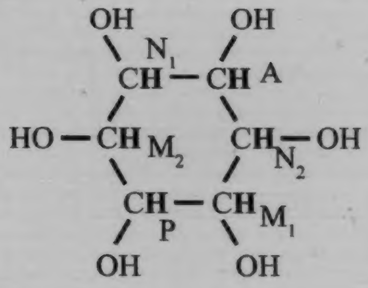
OH
OH
N_1
CH — CH
A
HO — CH
M_2
CH — OH
N_2
CH — CH
M_1
P
OH
OH

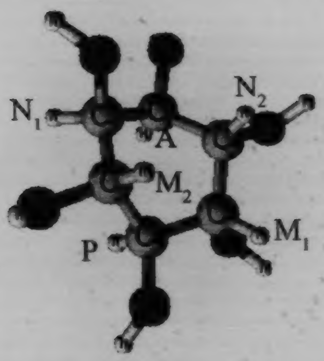
N_1
N_2
A
M_2
P
M_1

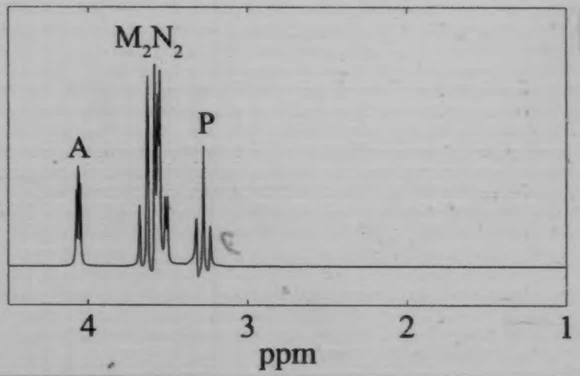

ω (ppm)		J (Hz)	
A	4.054	AN_1	2.889
M	3.614	AN_2	3.006
N	3.522	M_1N_2	9.997
P	3.269	M_1P	9.485
		M_2N_1	9.998
		M_2P	9.482

N-acetylaspartate (NAA)

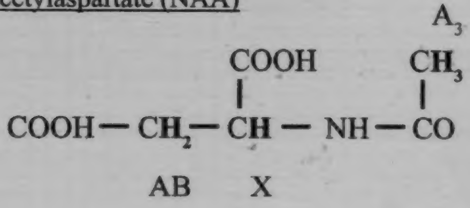

$$\begin{array}{ccccccccc} & & & & \overset{A_3}{CH_3} \\ & & COOH & & | \\ COOH - & CH_2 - & CH & - NH - & CO \\ & AB & X & & \end{array}$$

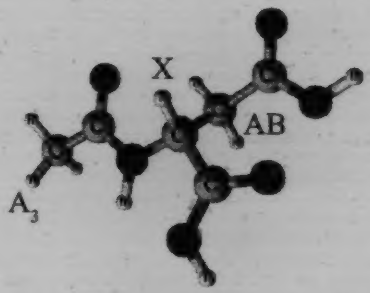

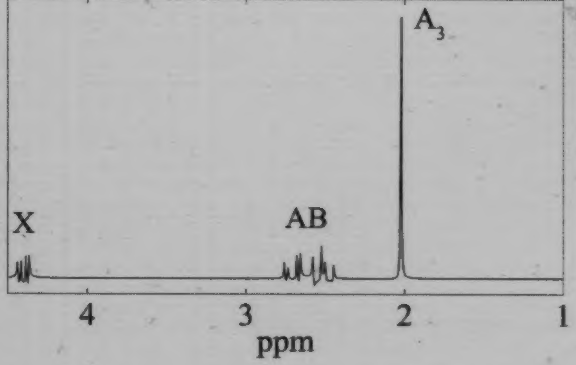

ω (ppm)		J (Hz)	
A_3	2.008	AB	-15.592
A	2.673	AX	3.861
B	2.486	BX	9.821
X	4.382		

Table 1-3: Metabolite concentration ranges in the human brain (76)

Metabolite	Abbreviation	Concentration (mmol/kg)
Acetate	Ace	0.4-0.8
N-acetylaspartate	NAA	7.9-16.6
N-acetylaspartylglutamate	NAAG	0.6-2.7
Adenosine triphosphate	ATP	3.0
Alanine	Ala	0.2-1.4
γ-Aminobutyric acid	GABA	1.3-1.9
Aspartate	Asp	1.0-1.4
Choline	Cho	0.9-2.5
Creatine	Cr	5.1-10.6
Glucose	Glc	1.0
Glutamate	Glu	6.0-12.5
Glutamine	Gln	3.0-5.8
Glutathione	GSH	2.0
Glycerol	-	<0.1
Glycerophosphorylcholine	GPC	1.0
Glycine	Gly	0.4-1.0
Histidine	His	0.09
Homocarnosine	-	0.23
Myo-inositol	mI, m-Ins	3.8-8.1
Scyllo-inositol	s-Ins	0.3-0.6
Lactate	Lac	0.4
Phenylalanine	Phe	<0.1
Phosphocreatine	PCr	3.2-5.5
Phosphorylcholine	PC	0.6
Phosphorylethanolamine	PE	1.1-1.5
Pyruvate	-	0.2
Serine	Ser	0.4
Succinate	Suc	0.4
Taurine	Tau	0.9-1.5
Threonine	Thr	0.3
Tryptophan	Trp	<0.1
Tyrosine	Tyr	<0.1
Valine	Val	0.1

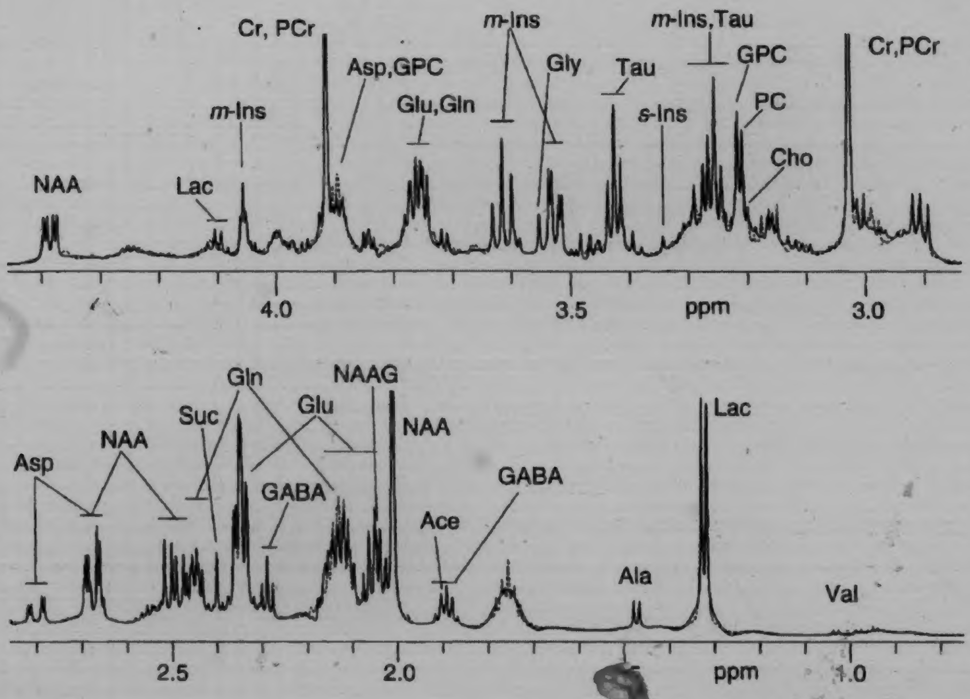

Figure 1-14: *High resolution spectrum acquired at 14.1 T from an extract of rat brain. The peaks are labeled according to the abbreviation definitions in Table 1-3.*

1.8 References

1. Destefano N, Matthews PM, Arnold DL. Reversible decreases in N-acetylaspartate after acute brain injury. Magn Reson Med 1995;34(5):721-727.

2. Graham GD, Blamire AM, Howseman AM, Rothman DL, Fayad PB, Brass LM, Petroff OAC, Shulman RG, Prichard JW. Proton magnetic resonance spectroscopy of cerebral lactate and other metabolites in stroke patients. Stroke 1992;23(3):333-340.

3. Gideon P, Henriksen O, Sperling B, Christiansen P, Olsen TS, Jorgensen HS, Arliensoborg P. Early time course of N-acetylaspartate, creatine and phosphocreatine, and compounds containing choline in the brain after acute stroke - a proton magnetic resonance spectroscopy study. Stroke 1992;23(11):1566-1572.

4. Barker PB, Gillard JH, Vanzijl PCM, Soher BJ, Hanley DF, Agildere AM, Oppenheimer SM, Bryan RN. Acute stroke - evaluation with serial proton MR spectroscopic imaging. Radiology 1994;192(3):723-732.

5. Sappeymarinier D, Calabrese G, Hetherington HP, Fisher SNG, Deicken R, Vandyke C, Fein G, Weiner MW. Proton magnetic resonance spectroscopy of human brain - applications to normal white matter, chronic infarction, and MRI white matter signal hyperintensities. Magn Reson Med 1992;26(2):313-327.

6. Nitkunan A, McIntyre DJO, Barrick TR, O'Sullivan M, Shen YJ, Clark CA, Howe FA, Markus HS. Correlations between MRS and DTI in cerebral small vessel disease. NMR Biomed 2006;19(5):610-616.

7. Cendes F, Andermann F, Preul MC, Arnold DL. Lateralization of temporal lobe epilepsy based on regional metabolic abnormalities in proton magnetic resonance spectroscopic images. Ann Neurol 1994;35(2):211-216.

8. Hugg JW, Laxer KD, Matson GB, Maudsley AA, Weiner MW. Neuron loss localizes human temporal lobe epilepsy by in vivo proton magnetic resonance spectroscopic imaging. Ann Neurol 1993;34(6):788-794.

9. Connelly A, Jackson GD, Duncan JS, King MD, Gadian DG. Magnetic resonance spectroscopy in temporal lobe epilepsy. Neurology 1994;44(8):1411-1417.

10. Petroff OAC, Pleban LA, Spencer DD. Symbiosis between in vivo and in vitro NMR spectroscopy - the creatine, N-acetylaspartate, glutamate, and GABA content of the epileptic human brain. Magn Reson Imaging 1995;13(8):1197-1211.

11. Ende GR, Laxer KD, Knowlton RC, Matson GB, Schuff N, Fein G, Weiner MW. Temporal lobe epilepsy: Bilateral hippocampal metabolite changes revealed at proton MR spectroscopic imaging. Radiology 1997;202(3):809-817.

12. Kuzniecky R, Hugg JW, Hetherington H, Butterworth E, Bilir E, Faught E, Gilliam F. Relative utility of H-1 spectroscopic imaging and hippocampal volumetry in the lateralization of mesial temporal lobe epilepsy. Neurology 1998;51(1):66-71.

13. Sanacora G, Mason GF, Rothman DL, Behar KL, Hyder F, Petroff OAC, Berman RM, Charney DS, Krystal JH. Reduced cortical gamma-aminobutyric acid levels in depressed patients determined by proton magnetic resonance spectroscopy. Arch Gen Psychiatry 1999;56(11):1043-1047.

14. Czeh B, Michaelis T, Watanabe T, Frahm J, de Biurrun G, van Kampen M, Bartolomucci A, Fuchs E. Stress-induced changes in cerebral metabolites, hippocampal volume, and cell proliferation are prevented by antidepressant treatment with tianeptine. Proc Natl Acad Sci U S A 2001;98(22):12796-12801.

15. Auer DP, Putz B, Kraft E, Lipinski B, Schill J, Holsboer F. Reduced glutamate in the anterior cingulate cortex in depression: An in vivo proton magnetic resonance spectroscopy study. Biol Psychiatry 2000;47(4):305-313.

16. Sanacora G, Gueorguieva R, Epperson CN, Wu YT, Appel M, Rothman DL, Krystal JH, Mason GF. Subtype-specific alterations of gamma-aminobutyric acid and glutamate in patients with major depression. Arch Gen Psychiatry 2004;61(7):705-713.

17. Davie CA, Hawkins CP, Barker GJ, Brennan A, Tofts PS, Miller DH, Mcdonald WI. Serial proton magnetic resonance spectroscopy in acute multiple sclerosis lesions. Brain 1994;117:49-58.

18. De Stefano N, Matthews PM, Fu LQ, Narayanan S, Stanley J, Francis GS, Antel JP, Arnold DL. Axonal damage correlates with disability in patients with relapsing-remitting multiple sclerosis - Results of a longitudinal magnetic resonance spectroscopy study. Brain 1998;121:1469-1477.

19. Arnold DL, Riess GT, Matthews PM, Francis GS, Collins DL, Wolfson C, Antel JP. Use of proton magnetic resonance spectroscopy for monitoring disease progression in multiple sclerosis. Ann Neurol 1994;36(1):76-82.

20. Matthews PM, Francis G, Antel J, Arnold DL. Proton magnetic resonance spectroscopy for metabolic characterization of plaques in multiple sclerosis. Neurology 1991;41(8):1251-1256.

21. Gonen O, Catalaa I, Babb JS, Ge Y, Mannon LJ, Kolson DL, Grossman RI. Total brain N-acetylaspartate - A new measure of disease load in MS. Neurology 2000;54(1):15-19.

22. Hiehle JF, Lenkinski RE, Grossman RI, Dousset V, Ramer KN, Schnall MD, Cohen JA, Gonzalezscarano F. Correlation of spectroscopy and magnetization transfer imaging in the evaluation of demyelinating lesions and normal appearing white matter in multiple sclerosis. Magn Reson Med 1994;32(3):285-293.

23. Davie CA, Wenning GK, Barker GJ, Tofts PS, Kendall BE, Quinn N, Mcdonald WI, Marsden CD, Miller DH. Differentiation of multiple system atrophy from idiopathic Parkinsons disease using proton magnetic resonance spectroscopy. Ann Neurol 1995;37(2):204-210.

24. Tedeschi G, Litvan I, Bonavita S, Bertolino A, Lundbom N, Patronas NJ, Hallett M. Proton magnetic resonance spectroscopic imaging in progressive supranuclear palsy, Parkinson's disease and corticobasal degeneration. Brain 1997;120:1541-1552.

25. Bowen BC, Block RE, Sanchezramos J, Pattany PM, Lampman DA, Murdoch JB, Quencer RM. Proton MR spectroscopy of the brain in 14 patients with Parkinsons disease. Am J Neurorad 1995;16(1):61-68.

26. Cruz CJ, Aminoff MJ, Meyerhoff DJ, Graham SH, Weiner MW. Proton MR spectroscopic imaging of the striatum in Parkinson's disease. Magn Reson Imaging 1997;15(6):619-624.

27. Schuff N, Amend D, Ezekiel F, Steinman SK, Tanabe J, Norman D, Jagust W, Kramer JH, Mastrianni JA, Fein G, Weiner MW. Changes of hippocampal N-acetyl aspartate and volume in Alzheimer's disease - A proton MR spectroscopic imaging and MRI study. Neurology 1997;49(6):1513-1521.

28. Miller BL, Moats RA, Shonk T, Ernst T, Woolley S, Ross BD. Alzheimer disease - depiction of increased cerebral myo-inositol with proton MR spectroscopy. Radiology 1993;187(2):433-437.

29. Kantarci K, Jack CR, Xu YC, Campeau NG, O'Brien PC, Smith GE, Ivnik RJ, Boeve BF, Kokmen E, Tangalos EG, Petersen RC. Regional metabolic patterns in mild cognitive impairment and Alzheimer's disease - A 1H MRS study. Neurology 2000;55(2):210-217.

30. Moats RA, Ernst T, Shonk TK, Ross BD. Abnormal cerebral metabolite concentrations in patients with probable Alzheimer disease. Magn Reson Med 1994;32(1):110-115.

31. Pfefferbaum A, Adalsteinsson E, Spielman D, Sullivan EV, Lim KO. In vivo brain concentrations of N-acetyl compounds, creatine, and choline in Alzheimer disease. Arch Gen Psychiatry 1999;56(2):185-192.

32. Buckley PF, Moore C, Long H, Larkin C, Thompson P, Mulvany F, Redmond O, Stack JP, Ennis JT, Waddington JL. 1H Magnetic resonance spectroscopy of the left temporal and frontal lobes in schizophrenia - clinical, neurodevelopmental, and cognitive correlates. Biol Psychiatry 1994;36(12):792-800.

33. Lim KO, Adalsteinsson E, Spielman D, Sullivan EV, Rosenbloom MJ, Pfefferbaum A. Proton magnetic resonance spectroscopic imaging of cortical gray and white matter in schizophrenia. Arch Gen Psychiatry 1998;55(4):346-352.

34. Mullins PG, Rowland L, Bustillo J, Bedrick EJ, Lauriello J, Brooks WM. Reproducibility of 1H MRS measurements in schizophrenic patients. Magn Reson Med 2003;50(4):704-707.

35. Rooney WD, Miller RG, Gelinas D, Schuff N, Maudsley AA, Weiner MW. Decreased N-acetylaspartate in motor cortex and corticospinal tract in ALS. Neurology 1998;50(6):1800-1805.

36. Pioro EP, Majors AW, Mitsumoto H, Nelson DR, Ng TC. H-1-MRS evidence of neurodegeneration and excess glutamate plus glutamine in ALS medulla. Neurology 1999;53(1):71-79.

37. Pohl C, Block W, Karitzky J, Traber F, Schmidt S, Grothe C, Lamerichs R, Schild H, Klockgether T. Proton magnetic resonance spectroscopy of the motor cortex in 70 patients with amyotrophic lateral sclerosis. Arch Neurol 2001;58(5):729-735.

38. Kim H, Wild JM, Allen PS. Strategy for the spectral filtering of myo-inositol and other strongly coupled spins. Magn Reson Med 2004;51(2):263-272.

39. Thompson RB, Allen PS. A new multiple quantum filter design procedure for use on strongly coupled spin systems found in vivo: Its application to glutamate. Magn Reson Med 1998;39(5):762-771.

40. Behar KL, Ogino T. Assignment of resonances in the 1H spectrum of rat brain by 2-dimensional shift correlated and J-resolved NMR spectroscopy. Magn Reson Med 1991;17(2):285-303.

41. Hurd R, Sailasuta N, Srinivasan R, Vigneron DB, Pelletier D, Nelson SJ. Measurement of brain glutamate using TE-averaged PRESS at 3T. Magn Reson Med 2004;51(3):435-440.

42. Mayer D, Spielman DM. Detection of glutamate in the human brain at 3 T using optimized constant time point resolved spectroscopy. Magn Reson Med 2005;54(2):439-442.

43. Ryner LN, Sorenson JA, Thomas MA. 3D localized 2D NMR spectroscopy on an MRI scanner. J Magn Reson B 1995;107(2):126-137.

44. Choi C, Coupland NJ, Bhardwaj PP, Malykhin N, Gheorghiu D, Allen PS. Measurement of brain glutamate and glutamine by spectrally-selective refocusing at 3 tesla. Magn Reson Med 2006;55(5):997-1005.

45. Lee HK, Yaman A, Nalcioglu O. Homonuclear J-refocused spectral editing technique for quantification of glutamine and glutamate by 1H NMR spectroscopy. Magn Reson Med 1995;34(2):253-259.

46. Pan JW, Mason GF, Pohost GM, Hetherington HP. Spectroscopic imaging of human brain glutamate by water-suppressed J-refocused coherence transfer at 4.1 T. Magn Reson Med 1996;36(1):7-12.

47. Rothman DL, Behar KL, Hetherington HP, Shulman RG. Homonuclear 1H double-resonance difference spectroscopy of the rat brain in vivo. Proc Natl Acad Sci U S A 1984;81(20):6330-6334.

48. Stern O. A method for the experimental examination of the directional quantization in magnetic fields. Zeitschrift Fur Physik 1921;7:249-253.

49. Gerlach W, Stern O. The directional quantisation in the magnetic field. Annalen Der Physik 1924;74(16):673-697.

50. Slichter CP. Principles of magnetic resonance. Berlin ; New York: Springer; 1996.

51. Hendee WR, Ritenour ER. Medical imaging physics. New York: Wiley-Liss; 2002.

52. Berliner LJ, Reuben J. Biological magnetic resonance, Volume 11, in vivo spectroscopy. New York,: Plenum Press; 1992.

53. Becker ED. High resolution NMR : theory and chemical applications. San Diego: Academic; 2000.

54. Chen CN, Hoult DI. Biomedical magnetic resonance technology. Bristol ; Philadelphia: A. Hilger; 1989.

55. Vlaardingerbroek MT, Boer JAd. Magnetic resonance imaging : theory and practice. New York: Springer; 1999.

56. Salibi N, Brown MA. Clinical MR spectoscopy: First principles. New York: Wiley-Liss; 1998.

57. Kettunen MI, Grohn OHJ, Kauppinen RA. Quantitative T1 rho NMR spectroscopy of rat cerebral metabolites in vivo: Effects of global ischemial. Magn Reson Med 2004;51(5):875-880.

58. Zaaraoui W, Fleysher L, Fleysher R, Liu ST, Soher BJ, Gonen O. Human brain-structure resolved T-2 relaxation times of proton metabolites at 3 Tesla. Magn Reson Med 2007;57(6):983-989.

59. Srinivasan R, Sailasuta N, Hurd R, Nelson S, Pelletier D. Evidence of elevated glutamate in multiple sclerosis using magnetic resonance spectroscopy at 3 T. Brain 2005;128:1016-1025.

60. Ethofer T, Mader I, Seeger U, Helms G, Erb M, Grodd W, Ludolph A, Klose U. Comparison of longitudinal metabolite relaxation times in different regions of the human brain at 1.5 and 3 Tesla. Magn Reson Med 2003;50(6):1296-1301.

61. Rutgers DR, van der Grond J. Relaxation times of choline, creatine and N-acetyl aspartate in human cerebral white matter at 1.5 T. NMR Biomed 2002;15(3):215-221.

62. Tsai SY, Posse S, Lin YR, Ko CW, Otazo R, Chung HW, Lin FH. Fast mapping of the T-2 relaxation time of cerebral metabolites using proton echo-planar spectroscopic imaging (PEPSI). Magn Reson Med 2007;57(5):859-865.

63. Cudalbu C, Rengle A, Beuf O, Cavassila S. Rat brain metabolite relaxation time estimates using magnetic resonance spectroscopy at two different field strengths. Comptes Rendus Chimie 2008;11(4-5):442-447.

64. Ramsey NF. Magnetic Shielding of Nuclei in Molecules. Physical Review 1950;78(6):699-703.

65. McMurry J. Organic chemistry. Pacific Grove: Brooks/Cole Pub. Co.; 1996.

66. Ramsey NF, Purcell EM. Interactions between nuclear spins in molecules. Physical Review 1952;85(1):143-144.

67. Pople JA, Schneider WG, Bernstein HJ. High-resolution nuclear magnetic resonance. New York: McGraw-Hill; 1959.

68. Kay LE, Mcclung RED. A product operator description of AB and ABX spin systems. J Magn Reson 1988;77(2):258-273.

69. Bottomley PA. Spatial localization in NMR spectroscopy in vivo. Ann N Y Acad Sci 1987;508:333-348.

70. Frahm J, Merboldt KD, Hanicke W. Localized proton spectroscopy using stimulated echoes. J Magn Reson 1987;72(3):502-508.

71. Haase A, Frahm J, Hanicke W, Matthaei D. 1H NMR chemical shift selective (CHESS) imaging. Phys Med Biol 1985;30(4):341-344.

72. Moonen CTW, Vanzijl PCM. Highly effective water suppression for in vivo proton NMR Spectroscopy (DRYSTEAM). J Magn Reson 1990;88(1):28-41.

73. Ogg RJ, Kingsley PB, Taylor JS. WET, a T1 insensitive and B1 insensitive water-suppression method for in vivo localized 1H NMR spectroscopy. J Magn Reson B 1994;104(1):1-10.

74. Sorensen OW, Eich GW, Levitt MH, Bodenhausen G, Ernst RR. Product operator formalism for the description of NMR pulse experiments. Prog NMR Spectrosc 1983;16:163-192.

75. Thompson RB, Allen PS. Sources of variability in the response of coupled spins to the PRESS sequence and their potential impact on metabolite quantification. Magn Reson Med 1999;41(6):1162-1169.

76. Govindaraju V, Young K, Maudsley AA. Proton NMR chemical shifts and coupling constants for brain metabolites. NMR Biomed 2000;13(3):129-153.

Chapter 2

Strongly Coupled Versus Uncoupled Spin Response to Radiofrequency Effects: Application to Glutamate and Glutamine in Spectroscopic Imaging[1]

2.1 Introduction

Proton Magnetic Resonance Spectroscopic Imaging (SI) (1) has been used to determine the distribution of metabolites in diseased brain (2). Previous studies have focused primarily on singlet resonances such as N-acetylaspartate (NAA), choline (Cho) and creatine (Cr) (2,3). Coupled spins have not been investigated as thoroughly, because complex coupling patterns can lead to difficulty in detection using standard spectroscopic imaging techniques. Nevertheless, some studies of coupled spins have examined glutamate (Glu) (4-6), glutamine (Gln) (4,6,7), myo-inositol (mI) (5,6), γ-aminobutyric acid (GABA) (8,9) and lactate (Lac) (10-12). In spectroscopic imaging, usually a two- or three-dimensional volume of interest (VOI) is defined by slice selection, and phase encoding is used to divide the VOI into localized voxels. Standard spectroscopic imaging sequences typically use soft pulses to perform slice selection (PRESS, STEAM), with inherent non-uniform excitation profiles (13). For a given slice, the distribution of flip angles across the slice profile will affect the amplitude and line shape of a given metabolite (14,15). This variation in flip angle makes metabolite quantification difficult, and methods have been proposed to correct for this effect for singlet resonances (16,17). Further studies have simulated and experimentally verified sources of signal loss for coupled spins in spectroscopic imaging experiments due to non-ideal flip angle distributions from soft pulses (15,18,19).

---

[1] A version of this chapter was published. Snyder JL, Thompson RB, Wild JM, Wilman AH. *NMR in Biomed.*, (in press, NBM 1214).

An advantage in SI compared to single voxel studies is the additional spatial information afforded by phase encoding, yielding localized spectra from which metabolic maps can be produced. At increasing magnetic field, imaging studies tend to yield significant advantages in spatial resolution and theoretically, signal-to-noise ratio (SNR). Spectroscopic imaging also benefits from application at high field, as spatial dimensions of individual voxels can be decreased in multi-voxel sets to achieve acceptable SNR values. Spectral resolution is also improved because of the increase in the field dependent chemical shift at higher magnetic fields. However, one problem more prevalent at higher field when using standard RF coils is RF interference that leads to a focusing of the radiofrequency distribution in the human head and an inhomogeneous RF field (20). At a static magnetic field strength of 4.7 T, the human head has similar dimensions to the radiation wavelength of ~20 cm (21). As a result, interference effects will decrease the flip angles significantly near the edge of the brain while maintaining the intended flip angle near the center. At 4.7 T, the RF magnitude received by areas near the edge of the brain can be reduced by 40% of the intended flip angle (21). The effect is less noticeable at lower fields, with only a reduction of 20% at 3 T (22), and no perceptible difference at 1.5 T. Consequently, voxels located away from the center of the brain will experience sub-optimal excitation, resulting in reduced intensity in a spectroscopic image that can be misinterpreted as a lower metabolite concentration. The significance of this effect has not been studied previously in spectroscopic imaging of strongly coupled spin systems.

Singlet resonances are expected to have a simple response to these RF distributions in a PRESS $(\alpha - 2\alpha - 2\alpha)$ spectroscopy sequence, with varying peak amplitudes corresponding to the deviation of the flip angle, α, from the normal 90°. Methods may be used to correct for this interference when identifying singlets in a similar manner to the field independent corrections for RF profile non-uniformity. The correction requires production of B_1 field maps and applying spatially dependent corrections to metabolite concentrations (23). However, in strongly coupled spin systems, signal variations resulting from flip angle deviations may be more complicated. In general, coupled spin multiplets are less intense than singlets in in vivo studies due to the splitting effects of scalar coupling and lower concentrations. Quantification of coupled spins becomes more challenging if coupled spins respond differently than singlets to flip angle variations. In particular, coupled spins may experience large signal variations and lineshape changes due to the addition of J-coupling at longer echo times that can make quantification challenging when flip angles vary. In a recent study, the effects of flip angle variation on the weakly coupled spin system of GABA were investigated (24), showing no major difference in singlet (Cr) and GABA variation. However, strongly coupled systems may respond differently than weakly coupled systems, as discussed in this paper.

This work investigates the effects of flip angle deviations due to RF inhomogeneities produced from high field interference effects on strongly coupled spins from a theoretical and experimental point of view. Singlet resonance Cho, and strongly coupled systems

Glu and Gln are investigated using the standard PRESS sequence for single voxel techniques and spectroscopic imaging. The strongly coupled PQ group of Glu and Gln is typically the target for in vivo quantification because of the lack of many overlapping metabolites, and therefore will be the primary focus of this study. It should also be noted that the coupled Cho resonances are not included, with analysis of the singlet resonance only.

2.2 Methods

2.2.1 Theoretical Simulations

Theoretical calculations were performed to determine the response of each spin system to the PRESS sequence using an in-house MATLAB™ numerical spin simulation program developed by Thompson (14). The simulation program was designed to accommodate arbitrary spin systems and included effects of strong coupling. Parameters incorporated into metabolite modeling included scalar coupling constants and chemical shifts. The program partitions the sequence into individual Hamiltonians (categorized as a delay, RF pulse, or gradient) and recalculates the density matrix after each section of the sequence, resulting in a final density matrix and free induction decay. RF pulses (based on experimental sinc pulses, 256 points, 5 lobes, 2500 Hz selective bandwidth for a 2 ms pulse length) were modeled along with corresponding slice selection gradients to simulate points in space. The program was run for each metabolite (Glu, Gln, Cho), varying the flip angle, α, according to the PRESS relation ($\alpha - 2\alpha - 2\alpha$). To determine PRESS sequence timings for the simulation (asymmetric PRESS, TE1 = first echo time, TE2 = second echo time), free induction decays were calculated for a range of values of

TE1 (10-200 ms) and TE2 (10-200 ms). **Figure 2-1** illustrates the simulated Glx PQ areas in TE space, without relaxation effects.

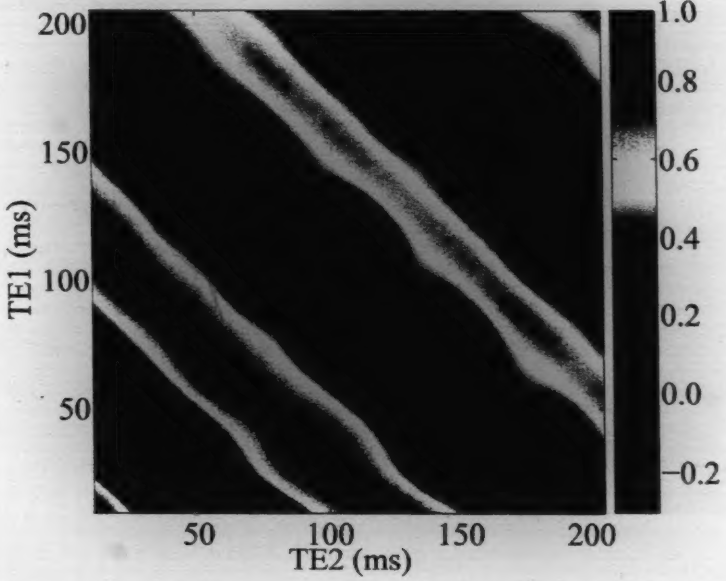

***Figure 2-1**: Glx PQ area calculations as a function of TE1 (vertical axis) and TE2 (horizontal axis). The areas are normalized to the maximum occurring at TE1 = TE2 = 10 ms. Relaxation effects are ignored in the calculated areas.*

Optimized timings were chosen to produce 100% peak height yield compared to a single pulse-acquire experiment (ignoring relaxation) and to simplify the lineshape of the Glx PQ multiplet, as well as reducing the contribution of macromolecules. These timings produced a lineshape with Glu and Gln peaks in phase with singlet peaks, allowing straightforward identification. From the simulation, optimized timings of TE1 = 20 ms and TE2 = 100 ms were used for all simulations and experiments in this work. In the case of Glu and Gln, the resulting spectra were added together to reflect the in vivo environment using a physiological Glu:Gln concentration ratio of 3:1 (25,26). In addition, a second simulation was produced assuming only weak coupling for Glu and

Gln, to compare to the strongly coupled case. Simulation linewidths were adjusted to fit experimental (phantom) data, and areas were computed for Cho and Glx (A and PQ multiplets).

In order to understand the effect of RF interference at 4.7 T on the human head, the field for an idealized, 16-element birdcage coil was calculated using a human head model created by Collins and Smith (22), showing decreasing RF intensity when moving away from the center of the brain (Figure 2-2).

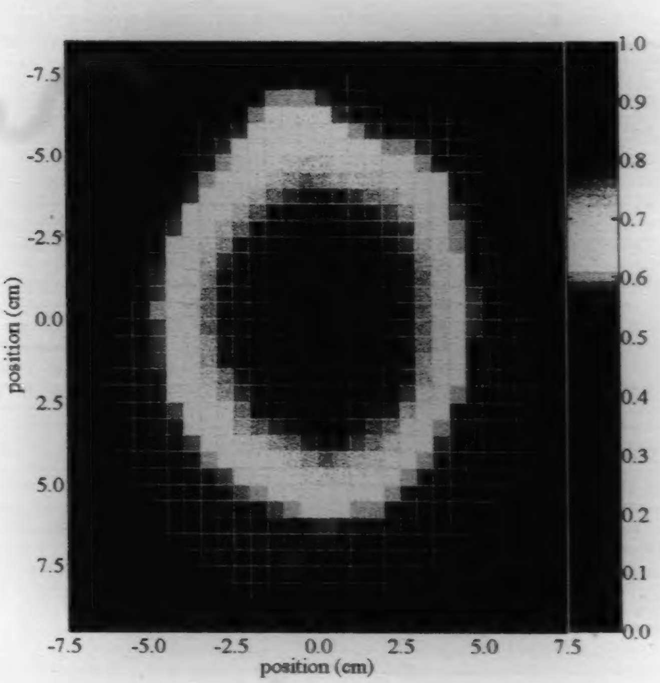

Figure 2-2: *Calculated B_1 map at 4.7 T using a 16-element birdcage coil (Collins), similar to the one used in experiments. The field focusing effect is due to RF interference. The axial slice is positioned 7 cm from the top of the skull. B_1 intensities are normalized to the highest value, occurring near the centre. In plane resolution is 5 mm in each direction. Positions displayed on each axis are relative to the area of highest B_1 intensity.*

Near the edge of the brain, the RF intensity is lowest with a value of 50 % compared to the center of the brain. The flip angles chosen for the simulation were derived from this data, with an angle of 65° corresponding to a position of 4.0 cm in the left-right direction from the center of the brain model, which receives 90°. Interference effects are minimal at the center of the field image, where full RF intensity is maintained.

2.2.2 Single Voxel Experiments

Phantom and volunteer experiments were performed to verify the theoretical findings. The spatial variation in flip angles arising from RF inhomogeneity effects was modeled in the single voxel case by using different values of α in the PRESS sequence. All experiments were performed using a 4.7 T Varian INOVA (Palo Alto, CA) whole body MRI system, equipped with a 4 kW RF amplifier, a maximum gradient strength of 35 mT/m and maximum slew rate of 117 T/m*s. Experiments were conducted using a quadrature, 16-element birdcage head coil (27 cm diameter) for transmission and reception.

Phantom experiments were performed on a cylindrical, pH balanced phantom (22 cm long, 8 cm diameter), keeping the ratio of concentrations equal to the physiological ratio (48 mM Glu, 16 mM Gln, 6 mM Cho). The phantom was placed at isocentre and the same voxel position was used for all experiments. The PRESS sequence employed WET (Water suppression Enhanced through T1 effects) water suppression (27), using four Gaussian shaped pulses of 20 ms length, each selecting a 50 Hz range centered on the water resonance, followed by crusher gradients. The optimized TE timings as determined via numerical simulation were used (TE1 = 20 ms, TE2 = 100 ms). Other sequence parameters included a 10 mm x 10 mm x 10 mm voxel size, 128 averages, pulse lengths of 3 ms (1660 Hz bandwidth) and a repetition time (TR) of 3000 ms. Pulse power was calibrated for the 90° – 180° – 180° case by adjusting the power until a maximum signal was produced in the water spectrum. The flip angle, α, was adjusted for each subsequent scan from 90° to 65° in 5° increments.

In vivo single voxel experiments were performed on 3 healthy volunteers with informed consent using a similar technique to the phantom experiments. A 2 cm x 2 cm x 2cm voxel was placed in parietal grey matter, with the power calibrated to produce maximum signal from the water peak for the voxel. Subsequent spectra were obtained while decreasing the flip angle, using the same procedure and increments as the phantom experiments, except a TR of 1500 ms and 256 averages were used.

2.2.3 Spectroscopic Imaging Experiments

Spectroscopic imaging was employed on three healthy volunteers (mean age 28 ± 2) with informed consent, using a standard PRESS sequence with WET water suppression. The images were used to provide anecdotal evidence of the results obtained in the single voxel and simulation experiments. In each case, a strip was prescribed across the head in the left-right direction, and divided into individual voxels by phase encoding. Two of the cases (case 1 and 2) had the strip in the occipital region (2 cm x 10 cm x 2 cm, 16 total voxels, 80 averages) while the third strip (case 3) was placed in the frontal region (2 cm x 10 cm x 2 cm, 32 total voxels, 40 averages). Pulse powers were calibrated in a similar manner to the single voxel in vivo experiments, defining a 90° pulse as an average over the slice. The total scan time for each case was 32 minutes, acquiring 2048 points per average, and a field of view of 18 cm in the left-right direction. No phase encoding was performed in the other two directions. The pulse lengths were 4 ms producing a spectral bandwidth of 1250 Hz. Peak area calculations were performed for each voxel for Cho and Glx PQ.

2.2.4 Area Calculations

In each experiment, area calculations were performed for the ppm range of the studied metabolites as obtained from the simulations. All spectra were phase and baseline corrected to the singlet resonances. The experimental data was broadened using an exponential filter of 1 Hz for the phantom study, and 2 Hz for the in vivo studies. Integration was used to calculate the areas. For each metabolite, the areas are normalized to the $\alpha = 90°$ case to show individual metabolite variations.

2.3 Results

Figure 2-3a-c shows the phantom spectra for Glx and Cho produced by the flip angles 90°, 80°, and 65° using a PRESS sequence with TE1 = 20 ms and TE2 = 100 ms.

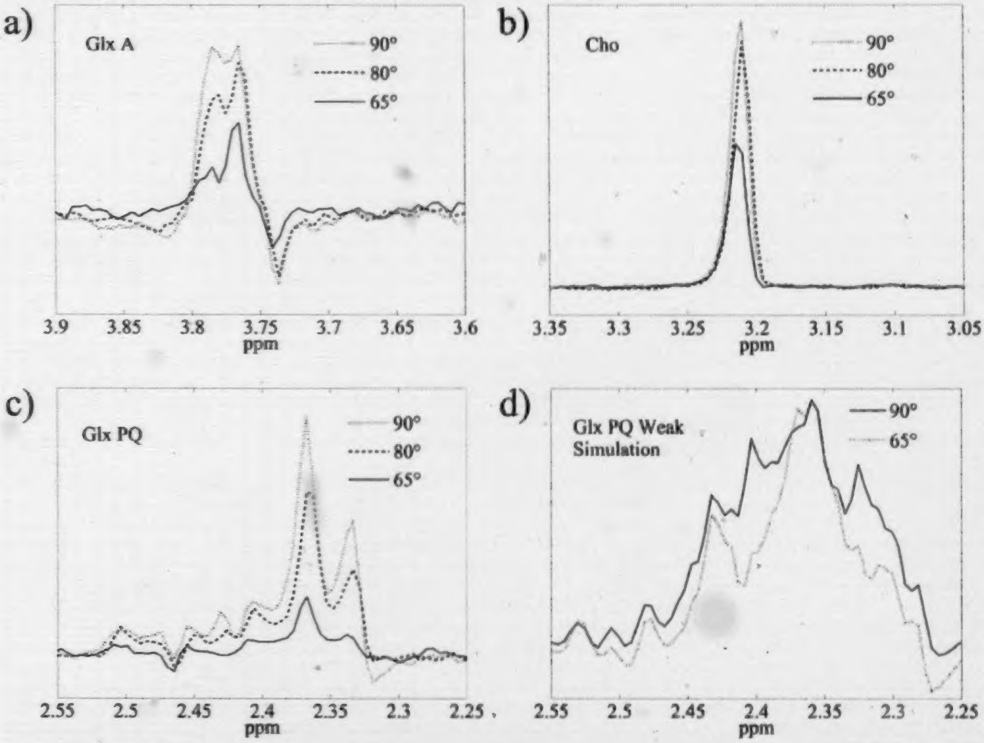

***Figure 2-3**: a-c) Spectra from phantom experiments at flip angles of 90° (dotted line), 80° (dashed) and 65° (solid) for investigated metabolite peaks: a) Glx A, b) Cho, and c) Glx PQ. d) Weak coupling approximation simulation of Glx PQ, illustrating flip angles of 90° (solid) and 65° (dotted). Peak amplitudes are in arbitrary units.*

Note the simple in phase appearance of the PQ multiplet (2.35 – 2.47 ppm) due to the optimized timings. The PQ multiplet height is most affected from the decrease in flip angle, and also experiences a significant lineshape change. As expected, the Cho peak has no apparent lineshape change, and a signal decrease that is not as severe as Glx. Figure 2-3d shows the limiting weak coupling case simulation of Glx, where there is only a small decrease in Glx PQ area compared to the strongly coupled case. This is consistent with Cho variation and the findings for GABA variation in ref. (24). Figure 2-4 shows the areas for Cho and Glx at different flip angles for both simulation and experiment. All calculated areas shown in Fig. 2-4 are normalized to the α = 90° case for each metabolite.

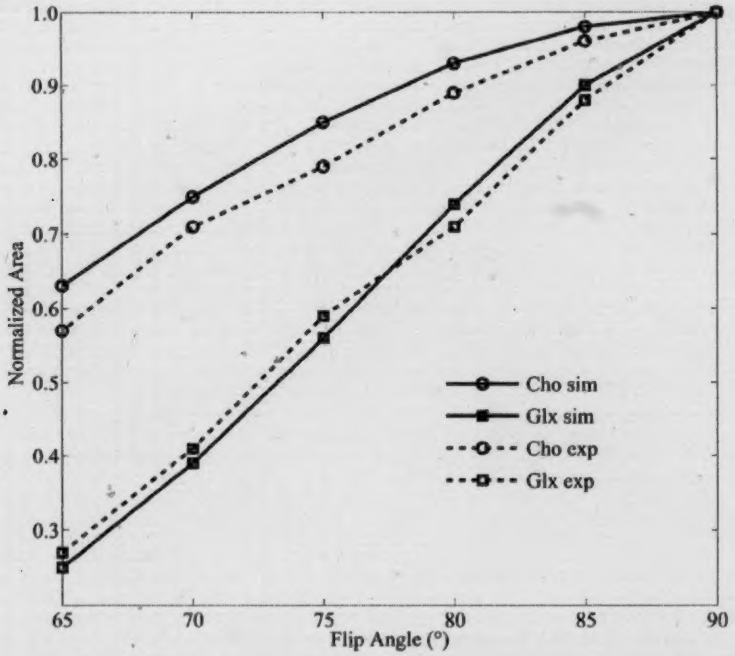

Figure 2-4: *Graph of simulated and experimental (phantom) areas for the Glx PQ and Cho peaks. In each case, the areas are normalized to the value occurring when α = 90°. Solid lines represent theoretical values (simulation), dashed lines are experiment.*

The graph also shows good agreement between theory (simulation) and experiment (phantom). When α is reduced to a value of 65° in the phantom experiment, the Glx PQ area is reduced to 27% of its maximum value at α = 90°, compared to 57% for Cho. In both cases, the Glx peak experiences the same drastic reduction in area with varying flip angle, unlike the Cho case. Even minor deviation in flip angle from optimal produces major differences in yield between the coupled and uncoupled spins in this case. For example, between α = 85° and α = 80°, a difference of 7% in intensity occurs for Cho, compared to 17% for Glx for the phantom study. When the flip angle is increased above 90°, a mirrored effect is produced consisting of similar values to flip angles below 90°, consistent with previous studies (24).

Table 2-1 shows the area calculations for the in vivo single voxel experiment. Choline areas have much lower variance than the corresponding Glx areas. The data follows the same general trend shown in the simulation and phantom experiments. Representative spectra are shown in Figure 2-5, at three different values of α (90°, 80°, and 65°).

Table 2-1: *In vivo normalized areas for Glx PQ, and Cho at different flip angles.*

Flip Angle (°)	**Glx PQ**	**Cho**
90	1.00	1.00
85	0.91±0.07	0.95±0.01
80	0.67±0.15	0.88±0.02
75	0.54±0.06	0.76±0.02
70	0.47±0.08	0.68±0.02
65	0.23±0.04	0.53±0.04

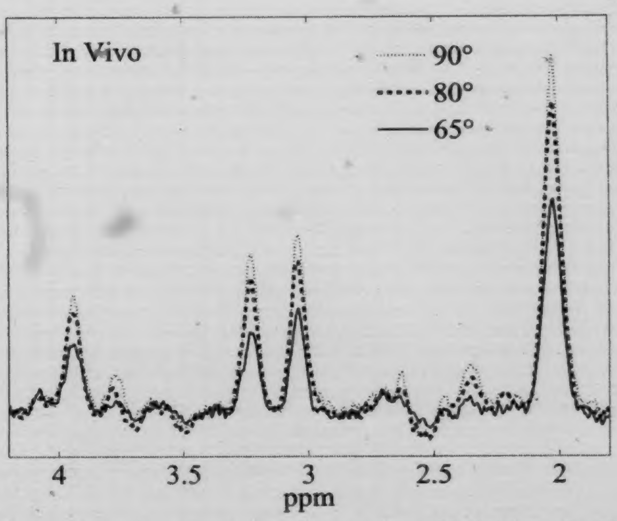

Figure 2-5: *Single voxel in vivo spectra at flip angles of 90° (dotted), 80° (dashed) and 65° (solid). The spectra represent the general trend supporting the phantom and simulation experiments.*

Spectroscopic imaging data is presented in Figure 2-6. This data supports the conclusions of the single voxel investigations. The region in the brain where the spectroscopic imaging data was acquired is shown in Fig. 2-6a. The rectangle denotes the volume of interest, overlaid on a standard gradient echo reference image. The spectroscopic imaging grid is overlaid on the VOI. The strip was prescribed in the left-right direction because of the symmetric RF distribution in this direction, although the strip could also be oriented in the anterior-posterior direction to produce the same effect, but would probably transect parts of the ventricles, producing partial volume effects. The three voxels chosen to compare peak areas are denoted by v1, v2 and v3.

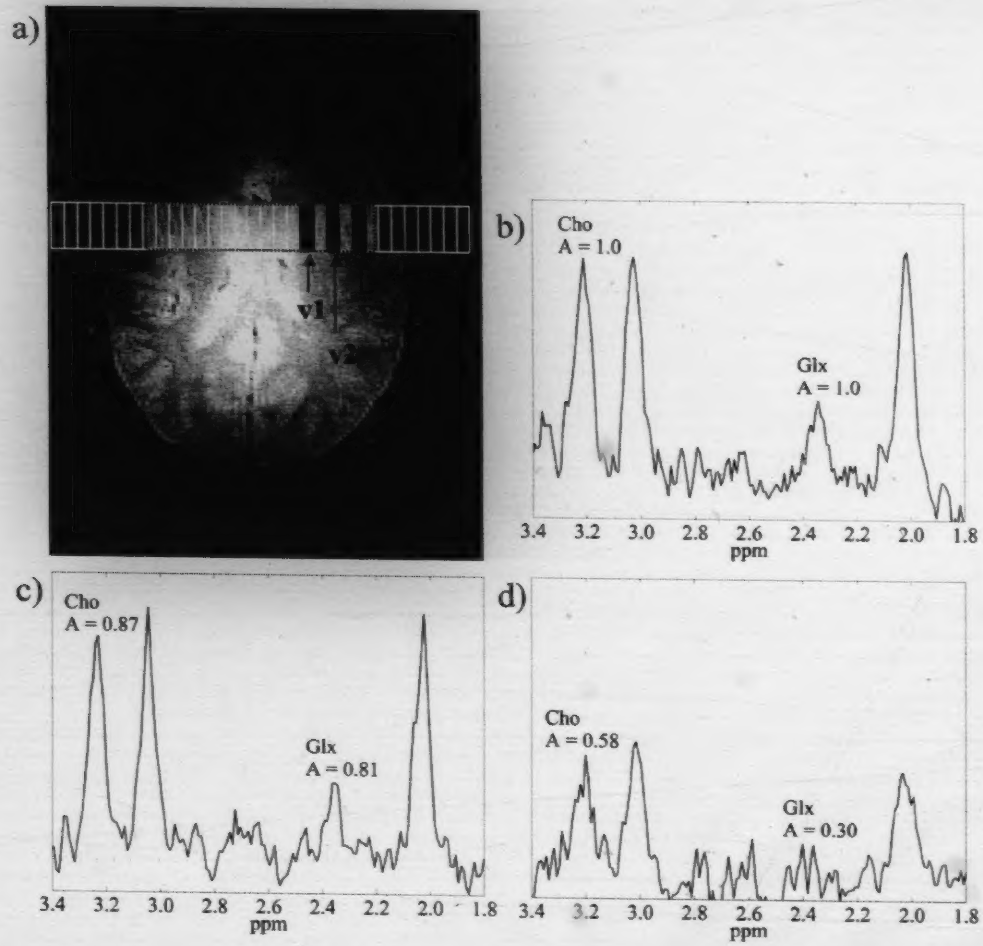

Figure 2-6: *a) Volume of interest (shaded rectangle) overlaid on the reference image, showing placement of the spectroscopic strip used. The 32 individual voxels are shown in white. Each voxel measured 5.6 mm (left-right) and 20 mm (anterior-posterior and superior-inferior). The corresponding spectra for voxels labeled v1, v2 and v3 are shown in b), c) and d), respectively. Areas shown are normalized to the v1 case for each metabolite.*

Figures 2-6b-d show spectra from these voxels v1, as indicated in Fig. 2-6a. The v1 voxel is located nearest to the center of the brain, 2 cm from the area calculated to have the maximum RF intensity, with a corresponding calculated flip angle of ~80°. The location of v3 is 4.2 cm from the area of maximum intensity, corresponding to a calculated flip angle of ~65°. Flip angles are calculated based on the position of the voxel relative to the B_1 map. The measured Glx SNRs for the v1, v2 and v3 voxels are 7.7, 6.5 and 4.6, respectively. Even at these relatively small SNRs, the large decrease in Glx PQ area compared to the smaller decrease in Cho is readily apparent. Between voxels v1 and v3, there is an area decrease of 42% for Cho and 70% for Glx PQ. These intensity variations show agreement with the trends illustrated in the phantom studies and simulation. In the simulation, the Cho area at 80° was 93% and 63% at 65°, resulting in a relative signal loss of 32% between these two flip angles. Also for the simulation, the relative signal loss for Glx PQ was 66% between 80° and 65°.

2.4 Discussion

The differences in yield between coupled and uncoupled spin systems due to RF destructive interference has been clearly illustrated for Glx and Cho. The Cho singlet area was significantly less affected than the Glx PQ area in the spectroscopic imaging study (Fig. 2-6), as predicted by single voxel simulation, phantom, and in vivo experiments (Figs. 2-3, 2-4 and 2-5). Even a minor change in flip angle or a correspondingly small change in position produces a large deviation in yield between strongly coupled and uncoupled spins. These differences may lead to improper quantification of concentrations in spectroscopic imaging experiments. While previously published correction methods (23) will lessen RF interference effects in singlet quantification, this study shows that this approach is not applicable for the case of strongly coupled spin systems. A global correction factor will not alleviate differences in intensity due to RF variations because coupled spin systems may react differently than uncoupled systems when less than optimal excitation and refocusing is present.

It should be noted that the RF destructive interference effect is field dependent, and becomes more complicated at higher static magnetic field strengths. At 3 T, the effects are perceptible, but not as significant as at 4.7 T, with a RF reduction near the edge of the brain in the human head model at 3 T of 20%, compared to 50% at 4.7 T (22). For example, a flip angle of 65° occurs at 6 cm in the left-right direction from the center of the head (90°) for 3 T, whereas at 4.7 T, it occurs at only 4 cm from the center. Therefore, in an equal volume of interest, less flip angle variation will occur in the 3 T case. These effects will be even more significant at higher fields that are becoming increasingly available, most notably 7 T. Moreover, higher field systems offer increased signal yield and spectral discrimination as compared to lower fields. Therefore, strongly coupled spin systems such as Glu and Gln will be increasingly targeted, placing specific importance on RF interference effects. These effects are not limited to Glu and Gln, and are important in other strongly coupled spin systems such as mI, and Glutathione. As illustrated in Fig. 2d, the weakly coupled response of Glx does not vary significantly from the response of Cho. Others have also found similar trends due to flip angle variations for GABA (24). Therefore, it is important to restrict our conclusions to strongly coupled spins only, particularly Glu and Gln. In addition, the response of Glx tends to the singlet response at short echo time, and these results are further restricted to long echo time studies.

One potential solution to the yield problem between coupled and uncoupled spins would be to acquire the necessary variation patterns for each metabolite individually, and apply a correction factor for each metabolite. Most quantification schemes apply a fitting routine to fit metabolite peaks to the spectrum to be analyzed. A series of basis spectra need to be acquired for the fitting program to work. These spectra can be obtained from phantom experiments or simulations. However, the varying properties of the brain including dielectrics and tissue compartments make precise design of an experimental phantom model problematic to obtain the necessary RF variation.

A simpler solution that may lead to a more homogeneous RF distribution is the use of adiabatic pulses (28). While single adiabatic pulses perform well for inversion or excitation, composite adiabatic pulses or pairs of adiabatic pulses are needed to perform refocusing. To date, these pulses are not commonly used clinically because of the complexity of the pulse sequence design. Additionally, inclusion of these pulses can increase the sequence length and SAR (Specific Absorption Rate) if not employed properly. Nevertheless, in addition to correcting the RF distribution, adiabatic pulses typically have a well-defined pulse profile, and can also compensate for flip angle variations due to slice imperfection. A sequence such as LASER (Localization by Adiabatic SElective Refocussing) (28) may be modified into a spectroscopic imaging sequence to produce adequate results. To decrease the sequence length, slice selection can be performed in less than 3 directions, as well as choosing a non-adiabatic pulse for excitation. However, use of a non-selective hard pulse for excitation limits the sequence to single slice experiments. A study investigating the use of LASER in spectroscopic imaging of glutamate has been recently published (29), in which Glu concentrations are shown with small variability in similar tissues. It should be noted that the effects of adiabatic pulses on coupled systems have not been investigated thoroughly and should be quantified before implementing a LASER SI sequence as common practice. Lastly, hardware improvements and new coil technology, including the method of RF shimming may also help overcome RF interference in the future (30).

It must be noted that if full quantification of spectroscopic imaging data is needed, a proper tissue segmentation scheme is required. Differences in voxel composition due to cerebral spinal fluid and grey and white matter must be accounted for to provide accurate quantification. This work does not propose any absolute quantification scheme; merely it illustrates trend differences between a singlet resonance and strongly coupled spin systems that hold regardless of the voxel constitution. Tissue differences between grey and white matter alone do not justify the results presented which are supported by simulation, phantom, and in vivo single voxel experiments.

In conclusion, this study illustrates the effects of RF interference at 4.7 T on metabolite quantification in spectroscopic imaging. Phantom experiments and numerical simulations modeled the RF interference in single voxel spectroscopy using flip angle variation, which agreed with signal variation in in vivo single voxel experiments and spectroscopic imaging. This work illustrates the differences in peak area variations between Glx and Cho, particularly that the Glx peak area is affected much more by RF inhomogeneities due to destructive interference in the human head. Even minor deviations from optimal flip angles produced severe effects on strongly coupled spin yield compared to uncoupled spins. Therefore, in spectroscopic imaging at longer echo times, both the flip angle distribution and resulting coupled spin response must be accounted for to properly quantify strongly coupled spins.

2.5 References

1. Brown TR, Kincaid BM, Ugurbil K. NMR chemical-shift imaging in 3 dimensions. Proc Natl Acad Sci U S A 1982;79(11):3523-3526.

2. Pan JW, Hetherington HP, Vaughan JT, Mitchell G, Pohost GM, Whitaker JN. Evaluation of multiple sclerosis by 1H spectroscopic imaging at 4.1 T. Magn Reson Med 1996;36(1):72-77.

3. Holshouser BA, Tong KA, Ashwal S. Proton MR spectroscopic imaging depicts diffuse axonal injury in children with traumatic brain injury. AJNR Am J Neuroradiol 2005;26(5):1276-1285.

4. Mason GF, Pan JW, Ponder SL, Twieg DB, Pohost GM, Hetherington HP. Detection of brain glutamate and glutamine in spectroscopic images at 4.1 T. Magn Reson Med 1994;32(1):142-145.

5. Srinivasan R, Vigneron D, Sailasuta N, Hurd R, Nelson S. A comparative study of myo-inositol quantification using LCmodel at 1.5 T and 3.0 T with 3 D 1H proton spectroscopic imaging of the human brain. Magn Reson Imaging 2004;22(4):523-528.

6. Posse S, Tedeschi G, Risinger R, Ogg R, Lebihan D. High-Speed H-1 Spectroscopic Imaging in Human Brain by Echo-Planar Spatial-Spectral Encoding. Magnetic Resonance in Medicine 1995;33(1):34-40.

7. Hetherington HP, Chu WJ, Gonen O, Pan JW. Robust fully automated shimming of the human brain for high-field H-1 spectroscopic imaging. Magnetic Resonance in Medicine 2006;56(1):26-33.

8. Jensen JE, Frederick BD, Wang L, Brown J, Renshaw PF. Two-dimensional, J-resolved spectroscopic imaging of GABA at 4 Tesla in the human brain. Magn Reson Med 2005;54(4):783-788.

9. Shen J, Shungu DC, Rothman DL. In vivo chemical shift imaging of gamma-aminobutyric acid in the human brain. Magn Reson Med 1999;41(1):35-42.

10. Bito Y, Ebisu T, Hirata S, Takegami T, Yamamoto Y, Tanaka C, Naruse S. Lactate discrimination incorporated into echo-planar spectroscopic imaging. Magn Reson Med 2001;45(4):568-574.

11. Duijn JH, Matson GB, Maudsley AA, Hugg JW, Weiner MW. Human Brain Infarction - Proton Mr Spectroscopy. Radiology 1992;183(3):711-718.

12. Nelson SJ. Analysis of volume MRI and MR spectroscopic imaging data for the evaluation of patients with brain tumors. Magnetic Resonance in Medicine 2001;46(2):228-239.

13. Gruber S, Stadlbauer A, Mlynarik V, Gatterbauer B, Roessler K, Moser E. Proton magnetic resonance spectroscopic imaging in brain tumor diagnosis. Neurosurg Clin N Am 2005;16(1):101-114, vi.

14. Thompson RB, Allen PS. Sources of variability in the response of coupled spins to the PRESS sequence and their potential impact on metabolite quantification. Magn Reson Med 1999;41(6):1162-1169.

15. Shen J. Slice-selective J-coupled coherence transfer using symmetric linear phase pulses: applications to localized GABA spectroscopy. J Magn Reson 2003;163(1):73-80.

16. Wild JM, Marshall I. Normalisation of metabolite images in 1H NMR spectroscopic imaging. Magn Reson Imaging 1997;15(9):1057-1066.

17. Thompson RB, Allen PS. Response of metabolites with coupled spins to the STEAM sequence. Magn Reson Med 2001;45(6):955-965.

18. Marshall I, Wild J. A systematic study of the lactate lineshape in PRESS-localized proton spectroscopy. Magnetic Resonance in Medicine 1998;40(1):72-78.

19. Wild JM, Thompson RB, Allen PS. Automated Quantitative Spectroscopic Imaging of Coupled Spins at 3 T - Influence of Realistic Volume Selective Pulse Sequences. Proc 8th ISMRM, 2000, #1847.

20. Van de Moortele PF, Akgun C, Adriany G, Moeller S, Ritter J, Collins CM, Smith MB, Vaughan JT, Ugurbil K. B(1) destructive interferences and spatial phase patterns at 7 T with a head transceiver array coil. Magn Reson Med 2005;54(6):1503-1518.

21. Thomas DL, De Vita E, Roberts S, Turner R, Yousry TA, Ordidge RJ. High-resolution fast spin echo imaging of the human brain at 4.7 T: implementation and sequence characteristics. Magn Reson Med 2004;51(6):1254-1264.

22. Collins CM, Smith MB. Signal-to-noise ratio and absorbed power as functions of main magnetic field strength, and definition of "90 degrees " RF pulse for the head in the birdcage coil. Magn Reson Med 2001;45(4):684-691.

23. Pan JW, Twieg DB, Hetherington HP. Quantitative spectroscopic imaging of the human brain. Magn Reson Med 1998;40(3):363-369.

24. Choi IY, Lee SP, Merkle H, Shen J. In vivo detection of gray and white matter differences in GABA concentration in the human brain. Neuroimage 2006;33(1):85-93.

25. Provencher SW. Estimation of metabolite concentrations from localized in vivo proton NMR spectra. Magn Reson Med 1993;30(6):672-679.

26. Pouwels PJW, Brockmann K, Kruse B, Wilken B, Wick M, Hanefeld F, Frahm J. Regional age dependence of human brain metabolites from infancy to adulthood as detected by quantitative localized proton MRS. Pediatr Res 1999;46(4):474-485.

27. Ogg RJ, Kingsley PB, Taylor JS. WET, a T1- and B1-insensitive water-suppression method for in vivo localized 1H NMR spectroscopy. J Magn Reson B 1994;104(1):1-10.

28. Garwood M, DelaBarre L. The return of the frequency sweep: Designing adiabatic pulses for contemporary NMR. J Magn Reson 2001;153(2):155-177.

29. Pan JW, Venkatraman T, Vives K, Spencer DD. Quantitative glutamate spectroscopic imaging of the human hippocampus. NMR Biomed 2006;19(2):209-216.

30. Mao WH, Smith MB, Collins CM. Exploring the limits of RF shimming for high-field MRI of the human head. Magn Reson Med 2006;56(4):918-922.

Chapter 3

Difference Spectroscopy Using PRESS Asymmetry: Application to Glutamate, Glutamine and Myo-inositol[1]

3.1 Introduction

Magnetic Resonance Spectroscopy (MRS) has been used extensively to quantify metabolite concentrations in the human brain in healthy and diseased states. Identification and quantification of singlet resonances is straightforward and provides information on several diseases. In contrast, coupled spin systems such as glutamate (Glu), glutamine (Gln) and myo-inositol (mI), are typically harder to quantify, but are also important in understanding brain function. The study of Glu is of particular interest as it is the major excitatory neurotransmitter in the brain, and is involved in neurodegenerative disease and psychiatric disorders, as illustrated in previous spectroscopy studies (1-3).

At typical clinical field strengths many coupled spin systems are obscured by stronger, overlapping resonances. In addition, coupled spin systems are generally less intense than singlets, due to complex coupling patterns. The quantification of Glu and Gln in spectroscopy can be problematic, as these strongly coupled systems exhibit complex spectra (both AMNPQ systems), and similar molecular composition which results in comparable spectral patterns and resonant frequencies that inhibit their discrimination at lower field strengths. The precise detection of mI is primarily hindered in vivo due to spectral overlap with other resonances. Several methods to aid detection of Glu, Gln and mI have been proposed including multiple quantum filtering (4,5), J-resolved spectroscopy (6-9) and other editing techniques (10-13). However, these techniques are not generally used on clinical systems due to their complexity in design. Instead, standard localization produced by PRESS (Point RESolved Spectroscopy) and STEAM (STimulated Echo Acquisition Mode) is typically used. More clinically viable Glu/Gln studies were performed using an optimized STEAM, which produced results applicable at 3 T (14) and 4 T (15), although the complementary MN peaks (2.04-2.14 ppm) were not addressed in these investigations.

---

[1] A version of this chapter has been submitted for publication (in revision). Snyder J, Thompson RB, Wilman AH. *NMR in Biomed.*

A new spectral editing technique for citrate using constant echo time (TE) PRESS was recently described in (16) and applied to spectroscopy of the prostate. Our work investigates the application of a similar technique to the human brain, to provide discrimination between the Glu and Gln resonances as well as mI visualization. The sequence design is simple and can be used with any PRESS sequence, allowing clinical applications. The method relies on strongly coupled signal modulation at constant TE when varying the timing between refocusing pulses. With 180° refocusing pulses, singlets and weakly coupled systems are not affected by the degree of PRESS asymmetry at a given TE. However, with appropriate choice of TE, strongly coupled systems may exhibit substantial variation as TE1 (first echo time) and TE2 (second echo time) are varied. The technique utilizes a constant echo time with two (or more) different TE1 and TE2 values chosen to optimize the signal variation. In this manner, subtracting the two signals results in a spectrum with only the metabolites that display these signal modulations along the chosen constant TE, therefore removing singlets and other resonances. An addition spectrum can also be produced that retains all spectral information from singlets and weakly coupled spins. The advantages of this editing approach lie largely in its simplicity and effectiveness. Unlike TE-averaged techniques, a constant TE is used throughout making the secondary addition spectrum a pure echo time; unlike most difference spectroscopy, there is no spectrally selective pulses needed so the whole spectrum is maintained, and unlike general multiple quantum filter techniques, unedited species can be recovered in the addition spectrum. The method can be applied to any strongly coupled spin system that exhibits significant signal modulation in TE space. This work investigates the discrimination of the strongly coupled metabolites of Glu and Gln and detection of mI using constant echo time difference spectroscopy in simulation as well as phantom and in vivo experiments. Additionally, analytical simplifications of these spin systems are introduced to provide a more general interpretation of the technique at any field strength.

3.2 Methods

3.2.1 Theory

3.2.1.1 Numerical Simulations

Theoretical simulations were performed to determine metabolite response to a standard PRESS sequence. The sequence was modeled using an in-house numerical spin system program developed by Thompson (17). The program segments the sequence into individual Hamiltonians characterized as a delay, radiofrequency (RF) pulse or gradient, calculates the density matrix after each segment, and produces a final free induction decay (FID). RF pulses (based on experimental sinc pulses, 256 points, 5 lobes, 2500 Hz selective bandwidth for a 2 ms pulse length) were modeled along with corresponding slice selection gradients to simulate points in space.

The program was run for a range of TE1 and TE2 values (10-200 ms each, 5 ms increments, totaling 1600 FIDs per metabolite) for Glu, Gln and mI. For each spectrum produced, peak area and height calculations were performed for each spin group of each metabolite, resulting in area maps illustrating signal modulation in TE space. In order to identify possible parameters for Glu/Gln discrimination, a constant TE line that maximizes the Glu variation while simultaneously minimizing Gln variation must be isolated. Once the optimized constant TE line was identified, two sets of time points (TE1, TE2) were chosen to maximize the Glu signal variation. At these particular echo times, simulated spectra were produced to show Glu/Gln signal variation, assuming a relative physiological concentration of 3:1 Glu:Gln (18,19). Each spectrum was broadened using a 3 Hz exponential filter to better approximate experimental data.

3.2.1.2 Analytical Approximations

The complexity of the Glu and Gln AMNPQ and mI AM_2N_2P systems inhibit construction of simple analytical product operator solutions to completely understand spin evolution during the PRESS sequence. However, it may be possible to model some of the spins individually to investigate signal trends due to PRESS asymmetry by focusing on the strongest J-couplings since weakly coupled spins will not be affected. In the case of Glu and Gln, both AMNPQ systems, the largest effects due to strong coupling should be realized in the PQ and MN groups. These groups are very strongly coupled at clinical field strengths, and all couplings to other spins in the molecule are much weaker. Specifically, the MN group of Glu has a J-coupling constant of –14.85 Hz, and a chemical shift frequency difference between the M and N spins, Δ, of 0.08 ppm, or 16 Hz at 4.7 T, resulting in Δ/J = 1.1. The couplings between M and N and other spins in the molecule are much weaker, and therefore we consider the MN group separately and neglect the weaker couplings to all other spins. Similarly, the PQ group is considered separately. Therefore, the PQ and MN groups individually have solutions equivalent to the strongly coupled AB group, with variation in signal (S) in terms of TE1 and TE2 given by (20):

$$S = \frac{1}{\Theta^2}\left(\begin{array}{l} \frac{2(\pi J)^3}{\Theta}\sin(\Theta TE)\sin(\pi JTE) + 2(\pi J)^2\cos(\Theta TE)\cos(\pi JTE) \\ +\frac{\pi J\Delta^2}{2\Theta}\sin(\pi JTE)\left(\sin(\Theta TE1)+\sin(\Theta TE2)\right) + \frac{\Delta^2}{2}\cos(\pi JTE) \end{array}\right), \tag{3.1}$$

where

$$\Theta = \frac{1}{2}\sqrt{\Delta^2 + (2\pi J)^2}. \tag{3.2}$$

The frequency difference between the A and B spins, ω_A - ω_B, is denoted by Δ (rad/s), and J (Hz) is the coupling constant. Further simplification of Eqn. (3.1) can be made to elucidate TE1 and TE2 effects on the signal by truncating all terms that do not involve TE1 or TE2 explicitly. The resulting truncated signal, S_t, incorporates the variable terms only (Eqn. (3.3))

$$S_t = \frac{\pi J\Delta^2}{2\Theta^3}\sin(\pi JTE)\left(\sin(\Theta TE1)+\sin(\Theta TE2)\right). \tag{3.3}$$

By evaluating Eqns. (3.1) and (3.3) the effects on the signal in TE space can be investigated for a strong AB system under PRESS excitation. Comparison of these results to the simulation calculations of the actual spin representation for each metabolite provides further insight into J, Δ, and TE1 and TE2 dependence.

3.2.2 Experimental

3.2.2.1 Phantom Experiments

Constant TE difference spectroscopy experiments were performed to validate the theory used to describe possible Glu/Gln discrimination. Both the analytical and simulation results were used to find the best constant TE line in TE space, and choose timings for the pair of experiments. As shown in the results section, the optimized timings used for phantom experiments were (TE1, TE2) = (125, 30) ms subtracted from (TE1, TE2) = (80, 75) ms, keeping the total echo time constant at 155 ms. These timings proved to have the greatest signal variation along a constant TE line and also a relatively simple lineshape allowing cleaner subtraction.

A cylindrical, pH-balanced phantom was constructed with dimensions of 22 cm length and 8 cm diameter containing in vivo physiological ratios of six metabolites (N-acetylaspartate (NAA), Glu, Gln, mI, creatine (Cr) and choline (Cho)). The phantom was placed at isocentre and the same voxel position was used for all experiments. Localization was produced by the PRESS sequence with WET (Water suppression

Enhanced through T1 effects) water suppression (21), using four Gaussian shaped pulses of 20 ms length, each selecting a 50 Hz range centered on the water resonance, followed by crusher gradients. The two sets of asymmetric PRESS timings used were interleaved into one sequence, with alternating FIDs acquired to minimize frequency drift and sequence specific abnormalities that may occur when subsequently acquiring two complete averaged FIDs at different asymmetries. Other sequence parameters included a 10 mm x 10 mm x 10 mm voxel size, 256 averages, sinc pulse lengths of 3 ms (1660 Hz bandwidth) and a repetition time (TR) of 1500 ms, resulting in a total acquisition time of 12 min, 48 s. As stated above, the echo times used were (TE1, TE2) = (80, 75) ms and (125, 30) ms, maintaining a total TE of 155 ms. All interleaved FIDs were individually phased, and then averaged, using the Cho resonance as a reference. In addition, two supplementary phantoms, containing Cho+Glu and Cho+Gln were constructed to investigate amounts of Glu and Gln remaining after subtraction to determine efficacy of Glu/Gln discrimination using this technique. The inclusion of Cho in the phantoms was valuable in evaluating the accuracy of the subtraction by minimizing residual signal at the Cho frequency.

3.2.2.2 In Vivo Experiments

In vivo experiments performed on 3 healthy volunteers with informed consent were conducted to verify the theoretical predictions. The PRESS sequence used was similar to the phantom case, except 512 averages and a 1.5 cm x 1.5 cm x 1.5 cm voxel were used. The voxel was placed in parietal grey matter to ensure maximal Glu concentration. The 90° RF pulse power was calibrated by adjusting the flip angle until a maximum water signal was achieved in the unsuppressed spectrum. All experiments were performed using a 4.7 T Varian INOVA (Palo Alto, CA) whole body MRI system, equipped with a 4 kW RF amplifier, a maximum gradient strength of 35 mT/m and maximum slew rate of 117 T/m*s. A quadrature, 16-element birdcage head coil (27 cm diameter) was used for transmission and reception.

3.3 Results

3.3.1 Glutamate/Glutamine Discrimination

The signal variation in TE space for Glu and Gln at 4.7 T is such that this particular method produces a spectrum with only the Glu MN multiplet (2.06-2.14 ppm) visible while other resonances are removed or substantially reduced, including Gln MN and glutamate/glutamine (Glx) PQ (2.35-2.47). Consequently, Glu can be quantified by the unobstructed signal from the MN group. In addition, the M_2N_2 multiplet of mI (3.5-3.7 ppm) is preserved for the specific timings used, with overlapping signals removed.

Signal variation in TE space for Glu MN produced by the simulator is illustrated in Fig. 3-1a. As stated previously, the simulator incorporates the entire AMNPQ system and is therefore a precise representation of the TE space variation. All area maps are normalized to the case approximating the pulse acquire experiment (TE1 = TE2 = 10 ms).

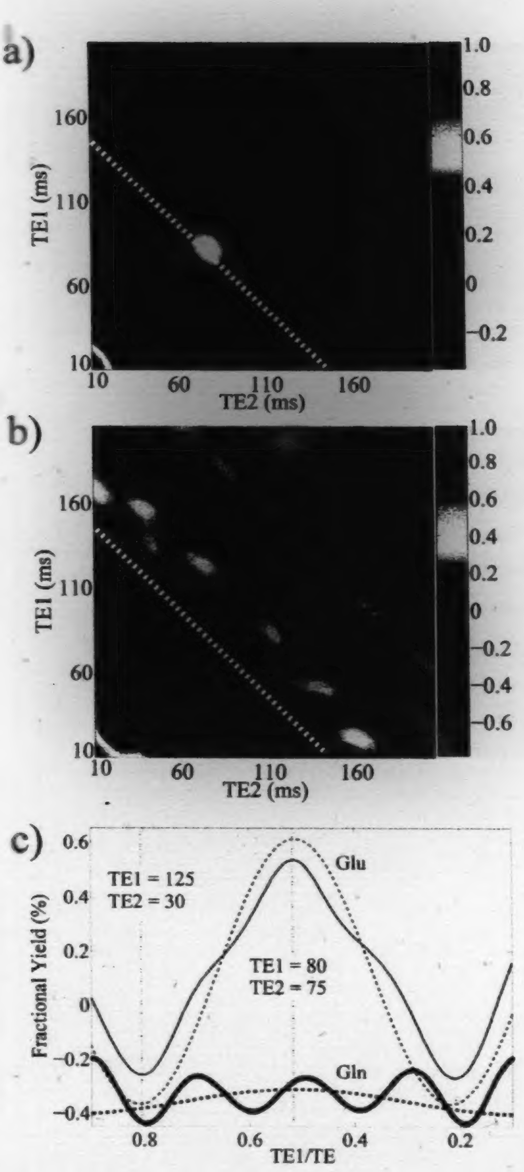

Figure 3-1: *TE space analysis for the MN group of Glu and Gln. Area maps are shown as a function of TE1 and TE2 for a) Glu MN and b) Gln MN. The dotted white line denotes a constant TE line of 155 ms with maximum signal variation. c) Fractional yield as a function of TE1/TE for Glu MN (top traces) and Gln MN (bottom traces) along the constant TE line of 155 ms. Dashed lines are the fractional yields computed from the analytical approximation in Eqn. (3.1). The two points used for the subtraction experiments are highlighted by vertical dotted lines. All TE maps are normalized to the area occurring at TE1 = TE2 = 10 ms, and relaxation effects are not considered.*

Note the large variation in signal along the TE = 155 ms line (highlighted). The corresponding TE space map for Gln MN is shown in Fig. 3-1b. Along the same constant TE line of 155 ms, the signal variation is negligible compared to the Glu MN case, allowing a difference experiment to discriminate between the two metabolites. Specifically, by choosing the time points (TE1, TE2) = (80, 75) ms and (TE1, TE2) = (125, 30) ms, difference spectroscopy yields a large Glu MN area and negligible Gln MN area. The graph of normalized areas along TE = 155 ms further illustrates the extreme differences between signal variation of Glu MN and Gln MN (Fig. 3-1c). The time points chosen to maximize the signal variation in Glu and minimize the variation in Gln are shown. Using the analytical approximation from Eq. (3.1), the signal variations along TE = 155 ms have also been computed (dashed lines in Fig. 3-1c), illustrating similar trends to the complete numerical simulation. Simulated spectra for Glu (solid lines) and Gln (dashed) using the optimized time points for the subtraction experiment are shown in Fig. 3-2.

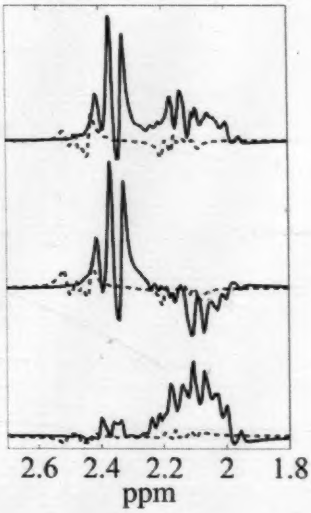

***Figure 3-2**: Simulated spectra for Glu (solid) and Gln (dashed) at timings of TE1 = 80 ms and TE2 = 75 ms (top) and TE1 = 125 ms and TE2 = 30 ms (middle). The resultant subtractions are shown in the bottom spectra.*

Note the large remaining signal in the MN region (2.0-2.3 ppm) and minimal Gln, as well as a large reduction in the Glx PQ multiplet (2.3-2.5 ppm). In the bottom spectra, calculated areas reveal a 96% contribution of Glu MN to the overall Glx MN peak, validating the time points chosen for Glu/Gln discrimination. Figure 3-3 shows phantom (left panel) and volunteer (right panel) spectra acquired at the same time points as in Fig. 3-2. Both subtraction spectra exhibit similar lineshapes in the Glx MN range, displaying a strong and remnant Glu MN resonance. In addition, the myo-inositol peak at 3.58 ppm maintains a large signal in the subtraction spectra, and therefore has variation patterns in TE space that produce reasonable results at the same time points.

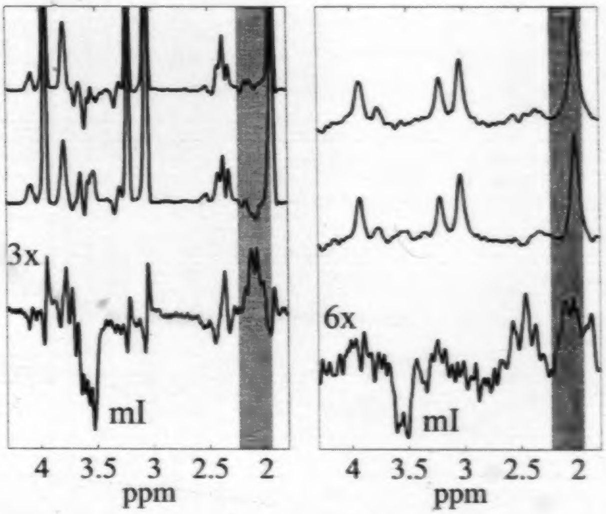

***Figure 3-3**: Phantom (left) and volunteer (right) spectra taken at time points of TE1 = 80 ms and TE2 = 75 ms (top) and TE1 = 125 ms and TE2 = 30 ms (middle). The bottom spectra show the resultant subtraction. The subtraction spectra have been magnified in the phantom and in vivo cases by 3 and 6 times, respectively. The shaded area shows the target Glu/Gln MN region. The large resultant mI peak is also labeled.*

3.3.2 Analytical Approximations

The utility of the analytical approximation has already been demonstrated for Glu and Gln above. Considering the M_2N_2 group of mI as a further example, the signal variation in TE space based on S_t in Eqn. (3.3) is illustrated in Fig. 3-4a. The illustration only shows trends in TE space and not absolute values for the extrema. The spacing of the extrema is very similar to the full AM_2N_2P treatment presented in Fig. 3-4b, showing a large signal variation along a constant TE line of 155 ms.

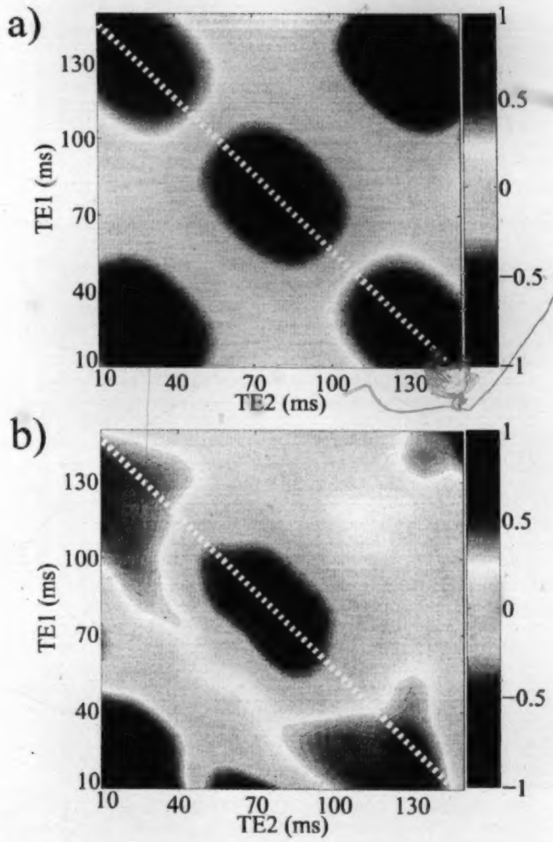

***Figure 3-4**: Myo-inositol M_2N_2 TE space signal map using a) truncated AB approximation (Eqn. (3.3)) and b) full simulation. The constant TE line with greatest signal variation is shown by the dotted line (TE = 155 ms).*

The extrema are regularly spaced at 1/J intervals (J = 9.8 Hz) in both the TE1 and TE2 directions. Figure 3-4 also displays a high degree of symmetry, as TE1 and TE2 values can be interchanged along a constant TE line with no discernable change in the result. The symmetry is also apparent in the full simulation maps (Figs. 3-1a and 3-1b), and is derived from the similar sine terms in Eqn. (3.3). The equation is useful to predict the frequency of the signal variation in TE space, although other strong coupling effects present in the full equation may conceal the underlying signal variation.

Considering the AB system more generally, we can determine the importance of Δ and J using Eqn. (3.1) for production of adequate yield in difference spectroscopy using PRESS asymmetry. For each combination of Δ and J, TE space area maps can be calculated to reveal any signal variation and asymmetric PRESS timings along the constant TE line exhibiting the largest variation chosen. To determine values suitable for a difference spectroscopy experiment, yields for multiple combinations of Δ and J were calculated in Fig. 3-5, where the amplitude is the signal difference between two optimal time points along the constant TE line that exhibits greatest variation for a specific Δ and J.

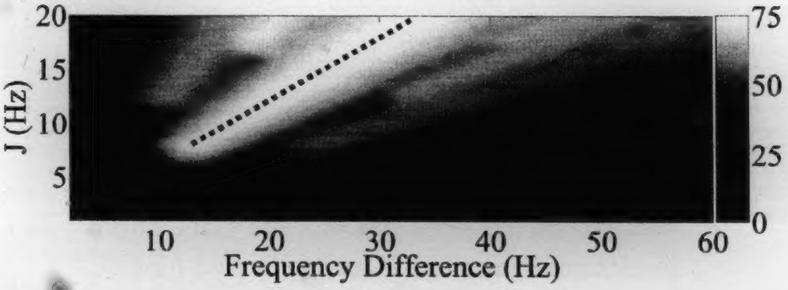

***Figure 3-5**: Maximum signal variation along the optimal constant TE line for a strongly coupled AB system as a function of the coupling constant and frequency difference. The dotted line denotes parameter sets to produce favorable subtraction spectroscopy experiments. Bright areas indicate greater signal variation, and therefore greater yield. The percentage yield (colorbar) is normalized to the maximum produced from 2 averages of a pulse acquire experiment.*

The y- and x-axis denote the coupling constant and frequency difference (Δ) in Hz, respectively, between the A and B spins. The region of greatest signal variation occurs in the neighborhood of the line:

$$\frac{J}{\Delta} = 0.6, \quad J > 6\,Hz. \tag{3.4}$$

Subtraction spectroscopy experiments with parameters conforming to the above equation will yield the best results for an AB system. Using this approximation, certain field strengths are preferable for certain metabolites. In terms of the metabolites studied in this work, Glu MN (Δ = 16 Hz, J = -14.85 Hz) has a resulting J/Δ magnitude of 0.93, and Gln MN (Δ = 4 Hz, J = -14.45) has a ratio of 3.61 at 4.7 T. Therefore, we expect a subtraction spectroscopy experiment involving Glu and Gln to have reasonable variation in Glu MN, and minimal variation in Gln MN, as shown in Fig. 3-2. The yield for Glu at 4.7 T was calculated to be 53%. In addition, the J/Δ ratio for the myo-inositol M_2N_2 multiplet (3.5-3.7 ppm) is (Δ = 16 Hz, J = 9.8) 0.61 at 4.7 T. Consequently, we expect a large signal variation in TE space for this particular resonance that has also been observed (Fig. 3-3), with a corresponding calculated yield of 75%. For specific spin groups, the required field strength for achieving favorable subtraction spectroscopy experiments can also be calculated from Eqn. (3.4). The optimal field for the typical Glu PQ target is calculated to be ~18.8 T, supporting the results in this work of utilizing the MN group for subtraction spectroscopy. Table 3-1 lists other possible metabolites and their optimized field strengths for viable difference spectroscopy based on Eqn. (3.1) using the common fields of 1.5, 3, 4, 4.7, and 7 T (22). The table only includes the best field for a particular group; however, other field strengths may produce satisfactory results. Metabolites with spin groups possessing optimal fields greater than 7 T have been excluded. The yield is also included, and is calculated as a percentage of the yield available for 2 averages of a pulse acquire experiment. Figure 3-6 shows the yield variation relative to the field strength for selected metabolites. The graph correlates well with the results for Glu MN and mI discussed above.

Table 3-1: *Optimal field strengths for subtraction spectroscopy for strongly coupled metabolites, based on the AB approximation in Eqn. (3.1).*

Metabolite	**Group**	**Δ (ppm)**	**J (Hz)**	**Optimal Field (T)**	**Yield (%)**
Aspartate (ABX)	AB	0.13	17.6	4.7	72
Glutamate (AMNPQ)	MN	0.08	-14.85	7	74
Myo-inositol (AM_2N_2P)	MN	0.08	9.8	4.7	75
N-acetylaspartate (ABX)	AB	0.18	15.5	3	71
Taurine (A_2B_2)	AB	0.17	6.7	1.5	53
Citrate (AB)	AB	0.14	15.4	4.7	73
N-acetylaspartylglutamate	AB	0.20	-15.9	3	74
(ABX, $AMNP_2$)	MN	0.16	-14.0	4	69

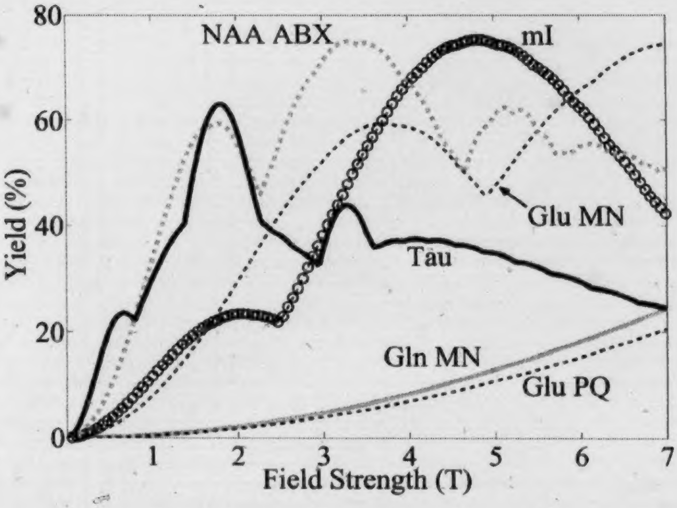

Figure 3-6: *Calculated yields as a percentage of 2 averages of a pulse acquire experiment based on the AB approximation (Eqn. (3.1)) for selected spin groups.*

3.4 Discussion

These results show that at a constant TE of 155 ms, the large signal variation in Glu MN and much lower Gln MN variation due to varied PRESS echo asymmetry allows discrimination between the two metabolites using subtraction spectroscopy at 4.7 T (Fig. 3-3). Phantom and simulation produced a yield of 53% for Glu and total contribution of 96% Glu to the Glx MN (2.0-2.3 ppm) signal upon subtraction. In addition, based on the analytical approximation, reasonable results for a similar Glu/Gln experiment at 3 T should be obtainable as signal variations are comparable to those at 4.7 T. The general analytical approach predicted best results for subtraction spectroscopy of mI (75% yield) at a field strength of 4.7 T (Fig. 3-6), with phantom and in vivo data (Fig. 3-3) supporting this conclusion.

Typically, the Glx PQ peak is the target for most in vivo studies, because of the greater amount of signal available compared to the MN peak. However, similar simulations performed for Glu and Gln PQ groups did not yield the necessary signal variation to perform subtraction spectroscopy. Based on the analytical equations, the variation required for subtraction of Glx PQ does not occur until a static field strength of 18.8 T (800 MHz) is obtained. The proximity of the NAA A_3 to the Glx MN peaks can also be problematic in in vivo experiments because of the larger linewidths. Therefore, regions in the brain that are difficult to shim may suffer more subtraction errors than those with higher field homogeneity.

The analytical equations can also be used to identify other systems with AB configurations that may display similar signal variations in TE space, as illustrated in Fig. 3-5. The plot is applicable to all field strengths, and therefore, the optimal field can be chosen to conduct subtraction experiments. Notable metabolites (and their optimized field strengths) conforming to the J/Δ ratio as in Eqn. (3.4) are: aspartate (4.7 T), myo-inositol (4.7 T), NAA (3 T), taurine (Tau, 1.5 T), citrate (4.7 T), and N-acetylaspartylglutamate (NAAG, 3 T and 4 T) (Table 3-1). The results for citrate are supported by previous work (16) that calculated an optimal field in the range of 3 – 4.7 T. It is also apparent that 4.7 T is close to the optimal field for myo-inositol as the subtraction spectrum in Fig. 3-3 shows good signal yield. It is possible that other fields for the previously mentioned metabolites may work for subtraction spectroscopy, although optimal yields will not be obtained. For example, in the current investigation of Glu and Gln, the optimal field strength for Glu subtraction as based on Figs. 3-5 and 3-6 and Table 3-1 is 7 T, with adequate results at 3 and 4.7 T. In order to determine sequence timings, full simulations incorporating the entire spin structure of the specific metabolite need to be performed, as was the case for Glu/Gln in this study.

Subtraction spectroscopy is of particular interest when other resonances overlap the signal of interest, which is the case with the Glu/Gln MN and NAA A_3 peak. This type of technique may also prove useful to remove the glycine contamination from the myo-inositol resonance around 3.54-3.62 ppm, as well as removing Cho from the Tau spectrum. Other possibilities for overlap removal include NAAG, NAA, citrate, and aspartate in the 2-3 ppm region. In comparison to other editing techniques, most notably multiple quantum filtering (4), no spectral information of singlets is lost, as the addition spectrum contains all singlet and non-varying coupled spin data. A recent study incorporated the constant TE approach in two-dimensional spectroscopy (S-PRESS, (23)) which provided valuable results in detecting the strongly coupled citrate system at 3 T. Similar to our experiment, the optimization of the total echo time is needed for each target metabolite, although sequence times in the 2D case may be longer to acquire the necessary SNR. Difference spectroscopy at constant TE also does not require a priori knowledge of relaxation parameters or application of spectrally selective pulses. Therefore, in conjunction with the addition spectrum, it is possible the subtraction spectrum may improve the confidence of automated spectral fitting programs for quantification.

In conclusion, this work illustrates the discrimination of Glu and Gln by subtraction spectroscopy of the MN groups and detection of mI in simulation, phantom and in vivo in human brain. The possibility of further exploration in subtraction spectroscopy for other metabolites at multiple field strengths is also discussed from an analytical point of view based on a strongly coupled AB system. The signal variation in TE space for strongly coupled spin groups provides a simple spectral editing technique based on subtraction spectroscopy. This technique is straightforward and requires no changes to the common PRESS sequence except for inter-echo times, and is therefore readily available for clinical use with some prior knowledge of coupled spin signal variation.

3.5 References

1. Woermann FG, McLean MA, Bartlett PA, Parker GJ, Barker GJ, Duncan JS. Short echo time single-voxel H-1 magnetic resonance spectroscopy in magnetic resonance imaging negative temporal lobe epilepsy: Different biochemical profile compared with hippocampal sclerosis. Ann Neurol 1999;45(3):369-376.

2. Moats RA, Ernst T, Shonk TK, Ross BD. Abnormal Cerebral Metabolite Concentrations in Patients with Probable Alzheimer Disease. Magn Reson Med 1994;32(1):110-115.

3. Castillo M, Kwock L, Courvoisie H, Hooper SR. Proton MR spectroscopy in children with bipolar affective disorder: Preliminary observations. American Journal of Neuroradiology 2000;21(5):832-838.

4. Thompson RB, Allen PS. A new multiple quantum filter design procedure for use on strongly coupled spin systems found in vivo: Its application to glutamate. Magn Reson Med 1998;39(5):762-771.

5. Kim H, Wild JM, Allen PS. Strategy for the spectral filtering of myo-inositol and other strongly coupled spins. Magn Reson Med 2004;51(2):263-272.

6. Ryner LN, Sorenson JA, Thomas MA. 3D Localized 2D NMR Spectroscopy on an MRI Scanner. J Magn Reson B 1995;107(2):126-137.

7. Behar KL, Ogino T. Assignment of resonances in the 1H spectrum of rat brain by two-dimensional shift correlated and j-resolved NMR spectroscopy. Magn Reson Med 1991;17(2):285-303.

8. Mayer D, Spielman DM. Detection of glutamate in the human brain at 3 T using optimized constant time point resolved spectroscopy. Magn Reson Med 2005;54(2):439-442.

9. Hurd R, Sailasuta N, Srinivasan R, Vigneron DB, Pelletier D, Nelson SJ. Measurement of brain glutamate using TE-averaged PRESS at 3T. Magn Reson Med 2004;51(3):435-440.

10. Pan JW, Mason GF, Pohost GM, Hetherington HP. Spectroscopic imaging of human brain glutamate by water-suppressed J-refocused coherence transfer at 4.1 T. Magn Reson Med 1996;36(1):7-12.

11. Lee HK, Yaman A, Nalcioglu O. Homonuclear J-Refocused Spectral Editing Technique for Quantification of Glutamine and Glutamate by 1H NMR Spectroscopy. Magn Reson Med 1995;34(2):253-259.

12. Rothman DL, Behar KL, Hetherington HP, Shulman RG. Homonuclear 1H Double Resonance Difference Spectroscopy of the Rat Brain In vivo. Proc Natl Acad Sci USA 1984;81(20):6330-6334.

13. Choi C, Coupland NJ, Bhardwaj PP, Malykhin N, Gheorghiu D, Allen PS. Measurement of brain glutamate and glutamine by spectrally-selective refocusing at 3 tesla. Magn Reson Med 2006;55(5):997-1005.

14. Schubert F, Gallinat J, Seifert F, Rinneberg H. Glutamate concentrations in human brain using single voxel proton magnetic resonance spectroscopy at 3 Tesla. Neuroimage 2004;21(4):1762-1771.

15. Hu JN, Yang SL, Xuan Y, Jiang Q, Yang YH, Haacke EM. Simultaneous detection of resolved glutamate, glutamine, and gamma-aminobutyric acid at 4 T. J Magn Reson 2007;185(2):204-213.

16. Gambarota G, van der Graaf M, Klomp D, Mulkern RV, Heerschap A. Echo-time independent signal modulations using PRESS sequences: A new approach to spectral editing of strongly coupled AB spin systems. J Magn Reson 2005;177(2):299-306.

17. Thompson RB, Allen PS. Sources of variability in the response of coupled spins to the PRESS sequence and their potential impact on metabolite quantification. Magn Reson Med 1999;41(6):1162-1169.

18. Provencher SW. Estimation of metabolite concentrations from localized in vivo proton NMR spectra. Magn Reson Med 1993;30(6):672-679.

19. Pouwels PJW, Brockmann K, Kruse B, Wilken B, Wick M, Hanefeld F, Frahm J. Regional age dependence of human brain metabolites from infancy to adulthood as detected by quantitative localized proton MRS. Pediatr Res 1999;46(4):474-485.

20. Wilman AH, Allen PS. The Response of the Strongly Coupled AB System of Citrate to Typical 1H MRS Localization Sequences. J Magn Reson B 1995;107(1):25-33.

21. Ogg RJ, Kingsley PB, Taylor JS. WET, a T1- and B1-insensitive water suppression method for in vivo localized 1H NMR spectroscopy. J Magn Reson B 1994;104(1):1-10.

22. Govindaraju V, Young K, Maudsley AA. Proton NMR chemical shifts and coupling constants for brain metabolites. NMR Biomed 2000;13(3):129-153.

23. Lange T, Trabesinger AH, Schulte RF, Dydak U, Boesiger P. Prostate spectroscopy at 3 tesla using two-dimensional S-PRESS. Magn Reson Med 2006;56(6):1220-1228.

Chapter 4

Spectral Editing of Weakly Coupled Spins Using Variable Flip Angles in PRESS Constant Echo Time Difference Spectroscopy

4.1 Introduction

The utility of Magnetic Resonance Spectroscopy (MRS) in quantifying brain chemical metabolites and investigating disease has been shown in previous studies. At standard clinical field strengths in proton MRS, the relatively narrow bandwidth of visible metabolites can be problematic as it can lead to overlapping of resonances, and therefore, difficulty in quantification. Coupled spin systems may suffer more drastic quantification problems, as coupling patterns produce complex spectra in addition to signal overlap with strong singlet resonances. Due to these hindrances, the quantification of coupled spin systems typically requires more advanced spectroscopy methods for spectral editing.

One metabolite in particular, γ-aminobutyric acid (GABA), has been investigated using many types of spectrally edited MRS. In the human brain, GABA acts as an inhibitory neurotransmitter, and its quantification aids in understanding many neurological disorders. GABA is a six-spin, weakly coupled system ($A_2M_2X_2$) at 4.7 T, with resonant frequencies occurring at chemical shifts of 3.01, 1.89 and 2.28 ppm. Detection via proton MRS is inhibited due to spectral overlap with other metabolites. Specifically, the X_2 peak at 2.28 ppm is obscured by glutamate, glutamine, and N-acetylaspartate (NAA) resonances, the A_2 resonance at 3.01 ppm is overshadowed by the strong singlet peak of creatine (Cr), and fat and other macromolecule contamination primarily affects the M_2 multiplet at 1.89 ppm with secondary contamination due to the NAA A_3 peak at 2.01 ppm in poorly shimmed samples. A typical target for spectral editing of GABA is the A_2 group, which only has one strong overlapping resonance. Several spectral editing techniques have been proposed including multiple quantum filtering and application of spectrally selective pulses (1-4). These methods improve previous quantification schemes, but may be difficult to implement clinically due to complex sequence design.

A new spectral editing method, based on constant echo time (TE) difference spectroscopy in PRESS (Chapter 3, (5)), relies on signal variation between two time points along a line of constant TE. In Chapter 3, a method for implementing this technique was illustrated for strongly coupled spin systems, which exploited the signal variations in TE space due to strong coupling in a molecule. This particular implementation of the technique does not apply to weakly coupled systems, as the necessary signal variation is not achieved in TE space. Rather, we propose a modification of the constant TE difference spectroscopy technique by inclusion of variable flip angles for the refocusing pulses. By changing the flip angle of one of the 180° pulses, it is possible to introduce enough signal variation between two time points with the same TE to allow difference spectroscopy experiments. The method is described theoretically using numerical simulation, as well as in preliminary phantom experiments to detect the A_2 resonance of GABA while minimizing the contribution of the overlapping Cr peak. In addition, an analytical explanation is provided assuming weak coupling parameters, to illustrate the effects of flip angle change to the density operator. It should be noted that the PRESS sequence uses no spectrally selective pulses as in previous difference spectroscopy (6), and maintains spectral information in the addition spectrum of non-varying singlet and coupled spin systems which are removed in the difference spectrum.

4.2 Methods

4.2.1 Theory

A two spin system, with spins labelled A and X, coupled via hyperfine interactions (J-coupling) can be classified by the Hamiltonian, $\mathcal{H}_J$:

$$\begin{aligned}\mathcal{H}_J &= 2\pi J_{AX}\left(\boldsymbol{A}\boldsymbol{\cdot}\boldsymbol{X}\right)\\ &= 2\pi J_{AX}\left(A_X X_X + A_Y X_Y + A_Z X_Z\right),\end{aligned} \tag{4.1}$$

where **A** and **X** are the vector product operators of the two spins, and J_{AX} is the coupling constant between them. When the system is deemed to be weakly coupled, the transverse components of Eqn. (4.1) are negligible and the Hamiltonian reduces to:

$$\mathcal{H}_J = 2\pi J_{AX}\left(A_Z X_Z\right). \tag{4.2}$$

This definition of the coupling operator is used exclusively to describe weakly coupled systems in the analytical approximations. The full simulations use the entire Hamiltonian as described in Eqn. (4.1) regardless of coupling strength.

4.2.1.1 Numerical Simulations

Constant TE difference spectroscopy relies on signal variations in TE space (TE1, TE2) along lines of constant TE. As stated previously, these variations are not produced for weakly coupled systems using the standard 90°-180°-180° PRESS sequence, unless one of the refocusing pulse flip angles is changed. For each weakly coupled system, signal variations in TE space were calculated by a numerical spin simulation program developed by Thompson (7). The program segments the sequence into individual Hamiltonians characterized as a delay, radiofrequency (RF) pulse or gradient, calculates the density matrix after each segment, and produces a final free induction decay (FID). RF pulses (based on experimental sinc pulses, 256 points, 5 lobes, 2500 Hz selective bandwidth for a 2 ms pulse length) were modeled along with corresponding slice selection gradients to simulate points in space. In the case of soft pulses, they were divided into many sections with each section encompassing a small time interval with a complementary Hamiltonian. The small time interval for each pulse section allows the continued use of time-independent Hamiltonians.

The program was run for a range of TE1 and TE2 values (10-200 ms each, 5 ms increments, totaling 1600 FIDs per metabolite). In addition, the same number of FIDs were acquired for each flip angle adjustment to a refocusing pulse according to a PRESS scheme of 90°-180°-α, where α was varied from 90° to 180° in increments of 5°. For each spectrum produced, peak area and height calculations were performed for each spin group of each metabolite, resulting in area maps illustrating signal modulation in TE space. In the case of the GABA experiment, the maps were used to determine the largest signal difference along a constant TE line, and therefore, the optimal value for the flip angle, α. Two time points from the optimal α map were chosen to simulate constant TE difference spectroscopy. The simulated spectra were broadened using a 3 Hz exponential filter, and GABA and Cr were combined using a parietal gray matter physiological concentration ratio of 5:1 (8).

4.2.1.2 Analytical Approximations

Although metabolites typically investigated in MRS spectroscopy are simple biological units compared to proteins and other complex molecules, the spin characteristics can be difficult to explain analytically. Consequently, this approach outlines the simplest weak coupling interaction between two spins in a PRESS sequence with variation of one of the refocusing pulse flip angles. In weakly coupled systems, this approach is feasible as a pair of coupled spins can be treated independent from the entire system.

In the case of GABA, it is weakly coupled at 4.7 T, with coupling between the A and M groups as well as between the M and X groups. This particular coupling of AM and MX can be modeled as a weak coupled system. The product operator solution of a weakly coupled system with coupling constant J and resonant frequencies ω_A and ω_X under PRESS excitation has been developed previously, with corresponding signal S:

$$\begin{aligned} S &\propto 2\cos(\pi J_{AX} TE1 + \pi J_{AX} TE2) \\ &= \cos(\pi J_{AX} TE), \end{aligned} \tag{4.3}$$

where TE1 and TE2 are the first and second echo times in the PRESS sequence, respectively and TE1+TE2 = TE. The addition of a variable final refocusing pulse flip angle introduces greater complexity in the solution:

$$\begin{aligned} S \propto \frac{1}{2}\left(1+\cos\left(\frac{1}{2}\Delta TE2\right)\right)&\left(\cos(\pi J_{AX} TE) - \cos(\pi J_{AX} TE1)\right)\left(\cos^2\alpha - 1\right) \\ &+ \left(\cos(\pi J_{AX} TE)\right)(1-\cos\alpha), \end{aligned} \tag{4.4}$$

where $\Delta = \omega_A - \omega_X$, and α is the flip angle of the final refocusing pulse. In the case when α is equal to 180°, Eqn. (4.4) reduces to the standard PRESS equation (4.3). Equation

(4.4) can be used to investigate any weakly coupled spin system. In the case of GABA, the signal computed from the above equation for the AM coupling is compared to the more accurate approach given by the simulator, which incorporates the entire spin structure.

4.2.2 Phantom Experiments

Both the analytical and simulation results were used to find the best constant TE line in TE space as well as the optimal flip angle, and to choose timings for the pair of experiments. The optimized timings used for phantom experiments were (TE1, TE2) = (120, 10) ms subtracted from (TE1, TE2) = (20, 110) ms, keeping the total echo time constant at 130 ms.

Two cylindrical, pH-balanced phantoms were constructed with dimensions of 22 cm length and 8 cm diameter containing 1) 100 mM GABA and 2) 100 mM Cr and 100 mM GABA. The first phantom was used to demonstrate the lineshape obtained at the particular TE. The second phantom contained double the in vivo Cr:GABA ratio (10:1) (8) to test the sequence under rigorous conditions. In each case, the phantom was placed at isocentre and the same voxel position was used for all experiments. Localization was produced by the PRESS sequence with WET (Water suppression Enhanced through T1 effects) water suppression (9), using four Gaussian shaped pulses of 20 ms length, each selecting a 50 Hz range centered on the water resonance, followed by crusher gradients. The two sets of asymmetric PRESS timings used were interleaved into one sequence, with alternating FIDs acquired to minimize frequency drift and sequence specific abnormalities that may occur when subsequently acquiring two complete averaged FIDs at different asymmetries. Prior to alternating between echo times, the FIDs were grouped into 8 average bins to allow for CYCLOPS (CYCLically Ordered Phase Sequence, (10,11)) phase cycling. Other sequence parameters included a 15 mm x 15 mm x 15 mm voxel size, 512 averages, pulse lengths of 3 ms (1660 Hz bandwidth) and a repetition time (TR) of 1500 ms, resulting in a total acquisition time of 25 min, 36 s. Each spectrum was phase corrected using Cr as the reference, or in the absence of Cr, the GABA resonance at 3.01 ppm. The spectra were also frequency corrected to increase the subtraction accuracy.

All experiments were performed using a 4.7 T Varian INOVA (Palo Alto, CA) whole body MRI system, equipped with a 4 kW RF amplifier, a maximum gradient strength of 35 mT/m and maximum slew rate of 117 T/m*s. A quadrature, 16-element birdcage head coil (27 cm diameter) was used for transmission and reception.

4.3 Results

4.3.1 Analytical Calculations

Based on Eqn. (4.4), TE space maps were produced for a coupling constant of 7.3 Hz, and a chemical shift difference of 226 Hz, equivalent to the AM coupling in GABA at 4.7 T. The effects of reduced flip angle on this weakly coupled system is shown in Fig. 4.1b with $\alpha = 120°$, and compared to the case when $\alpha = 180°$ (Fig 4.1a). The constant TE line with greatest signal variation occurs at TE = 1/J (136 ms), and with a repeating pattern proportional to 1/J. The signal along this line decreases steadily as the TE2 time is increased, due to incomplete refocusing. Rapid fluctuations in the TE2 direction are caused by the chemical shift difference, Δ, and are spaced every 2/Δ*1000 ms. The introduced signal variation due to the decreased flip angle will allow difference spectroscopy experiments to discriminate between coupled spins and singlets, which do not experience the same signal variations in TE space.

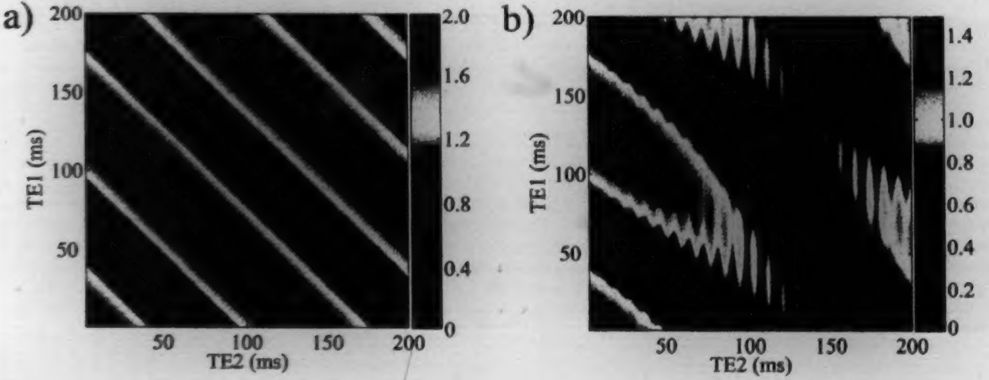

Figure 4-1: *TE space area maps calculated by Eqn.* (4.4) *for the A spin of a weakly coupled AX system with parameters of* $J = 7.3$ *Hz and* $\Delta = 226$ *Hz and a final refocusing flip angle of a)* $\alpha = 180°$, *and b)* $\alpha = 120°$.

The maximum available signal for a PRESS sequence with α = 180° for a two spin system is based on Eqn. (4.3), and decreases with flip angle according to Eqn. (4.4). At a value of α = 120°, the maximum available signal is 1.5. Therefore, the reduction in flip angle produces a 25% loss in the yield due to incomplete refocusing. In a difference spectroscopy experiment, the theoretical maximum yield without flip angle reduction is 4 compared to a maximum of 3 (75 %) at α = 120°. The obvious choice for TE1 and TE2 based on Fig. 4-1 is near either axis to maximize the signal difference. The optimization of the flip angle will be a combination of reducing losses due to decreased flip angle and maximizing the signal variation in TE space by flip angle reduction. Eqn. (4.4) predicts an optimized flip angle of 90° for the second refocusing pulse (Figure 4-2). The figure is computed from two points on the constant TE line with maximum variability for a particular α that produce the largest signal upon subtraction. It should be noted that in the case of GABA which involves more spins than the simple AX system, the full simulation should be used for optimization of the flip angle and timing parameters. The preceding results illustrate how a weakly coupled system is affected by reduced flip angle of one of the refocusing pulses.

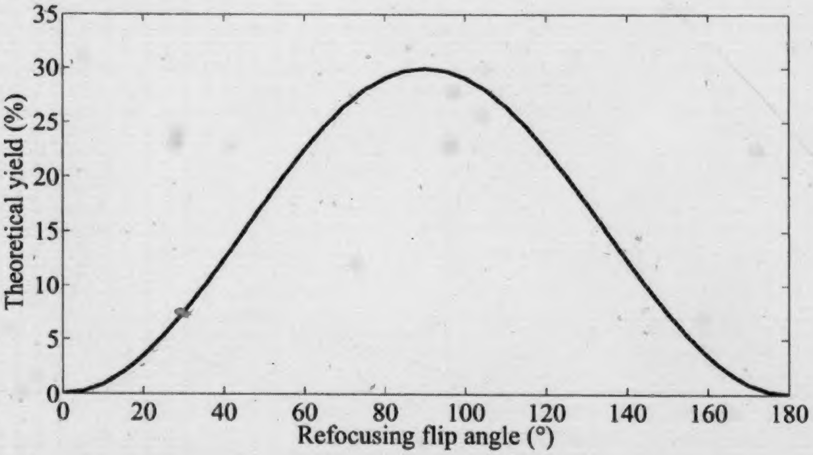

Figure 4-2: *Maximum difference spectroscopy yield based on a two spin system with J = 7.3 Hz and Δ = 226 Hz.*

The maximum theoretical yield for the GABA weakly coupled system difference spectroscopy experiment is 30 % at $\alpha = 90°$. At $\alpha = 120°$, the maximum yield is 23%. In addition, the values of J and Δ contribute to the amount of yield available for a difference spectroscopy experiment. In the case of a weaker system, such as an AX approximation of Lac, with J = 6.93 Hz and Δ = 556 Hz (12) there is a mild signal increase of 2 %. However, weak approximations of strongly coupled systems, for example the PQ group of Glu (J = -15.5, Δ = 2.8 Hz) show signal losses of 7 % compared to the GABA modeling case.

4.3.2 Simulations

Figure 4-3 illustrates TE space area maps for the A_2 multiplet of GABA. The values are normalized to the case when TE1 = TE2 = 10 ms, and relaxation effects are not considered. In a), $\alpha = 180°$, resulting in a symmetric pattern in TE space. The period between two similar points in the map is 1/J (J = 7.3 Hz) or 137 ms in either the TE1 or TE2 direction, similar to the analytical description. The optimal flip angle for signal variation along a line of constant TE was determined to be $\alpha = 120°$, to provide sufficient signal while maximizing the signal variation. The TE space map for GABA A_2 is shown in b) for this particular case.

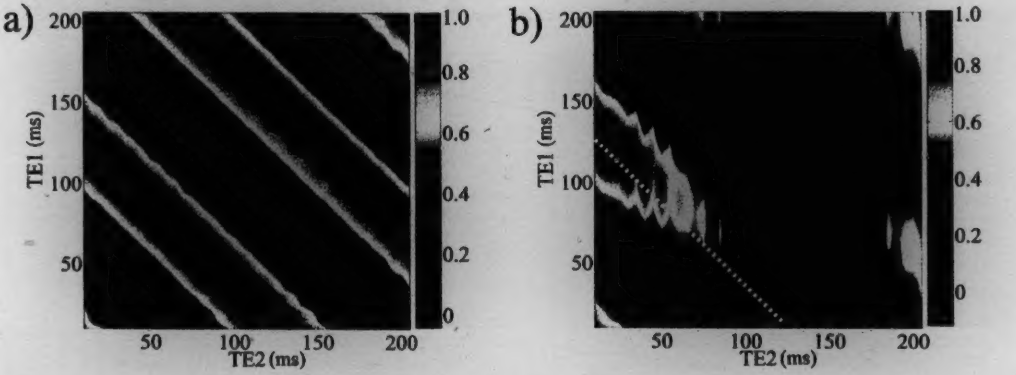

Figure 4-3: *TE space area maps produced by the simulator at 4.7 T for the A_2 group of GABA under PRESS excitation and flip angles of 90°-180°-α with a) $\alpha = 180°$, and b) $\alpha = 120°$. The dotted line denotes the line of constant TE with greatest signal variation (TE = 131 ms).*

The period along the TE1 direction remains 1/J as in a) due to complete refocusing, but is altered along the TE2 direction. The dotted white line shows a constant TE line with good asymmetry (TE = 131). Two time points from this line were chosen to simulate difference spectroscopy. Similar TE space maps were constructed for the A_3 singlet of Cr, and no signal variation was observed in the simulations, as expected. Figure 4-4 shows spectra from the subtraction simulation for GABA (solid lines) and Cr (dashed). The spectrum in a) shows the full Cr A_3 signal obscuring the relatively small GABA signal at 3 ppm at timings of TE1 = 120 ms, TE2 = 11 ms. Timings for spectra in b) and c) are taken from the map in Fig. 4-3b as mentioned above. The subtraction spectra are shown in d).

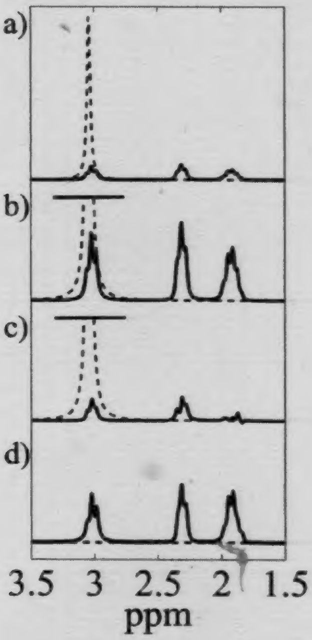

***Figure 4-4**: Spectra from the subtraction simulations with $\alpha = 120°$ at timings of a,b) TE1 = 120 ms, TE2 = 11 ms, and c) TE1 = 21 ms, TE2 = 110 ms. The subtraction spectra are shown in d). The Cr peak has been truncated in b and c.*

Note the large signal variation between GABA spectra in b) and c), producing a large remnant in the difference spectrum. The Cr signal does not have attributable variation in TE space, and is therefore negligible in d). Analysis of the GABA A_2 areas in b) and c) result in a 30% GABA yield in the subtraction spectrum compared to the equivalence of two pulse acquire experiments.

4.3.2.1 Phantom Experiments

The feasibility for GABA detection at 4.7 T has been established above, and is tested in vitro in phantom experiments. The spectra for the phantom containing only GABA is shown in Fig. 4-5. Fig. 4-5a shows the two spectra obtained at identical time points to the simulation, while 4-5b shows the difference spectrum. A short echo (TE = 24 ms) is shown in Fig. 4-5c for comparative purposes, and is not drawn to the same scale as 4-5a,b.

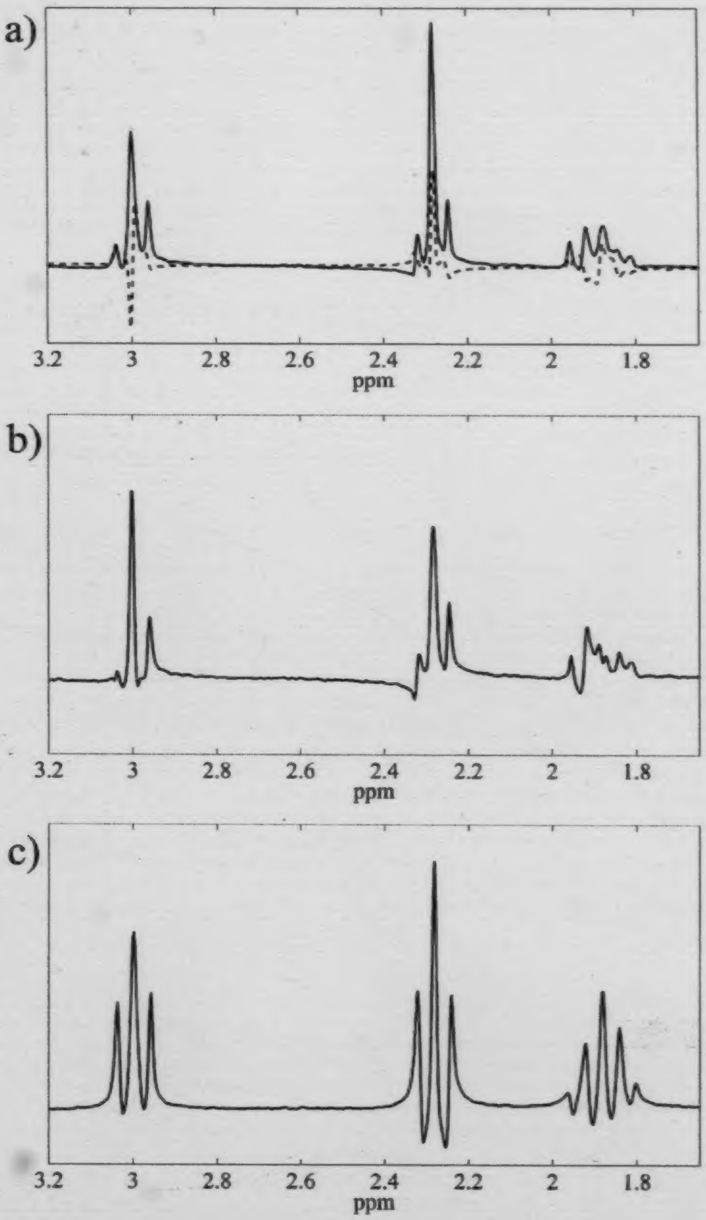

Figure 4-5: *Spectra acquired with a phantom containing only GABA. a) Both timings used in the difference spectroscopy experiment: TE1 = 120 ms, TE2 = 11 ms (solid) and TE1 = 21 ms, TE2 = 110 ms (dashed). b) Resultant subtraction spectrum. c) A short echo spectrum (TE = 24 ms) for lineshape comparison. All spectra were line broadened using a 1 Hz exponential filter. Note a) and b) are to the same scale, c) is not.*

The timings chosen have the effect of maximizing the central peak of the A_2 (3.01 ppm) and X_2 (2.28 ppm) resonances, which reduces the outer wings of the multiplets, compared to the multiplets in 4-5c which are broad and contain large wings. This type of in-phase shape will have less overlap with other, contaminating peaks and also lends in the subtraction process. In the subtraction spectrum, the major A_2 peak is larger than in either spectrum in a), resulting in an overall increase in yield to 45 % compared to that calculated in the simulation and analytical approaches.

Spectra from the phantom containing both GABA and Cr are shown in Fig. 4-6. Similar to Fig. 4-5, a) contains spectra at both timings, b) the subtraction spectrum, and c) a short echo spectrum. The subtraction and short echo spectra from 4-5 are overlayed in 4-6 as well.

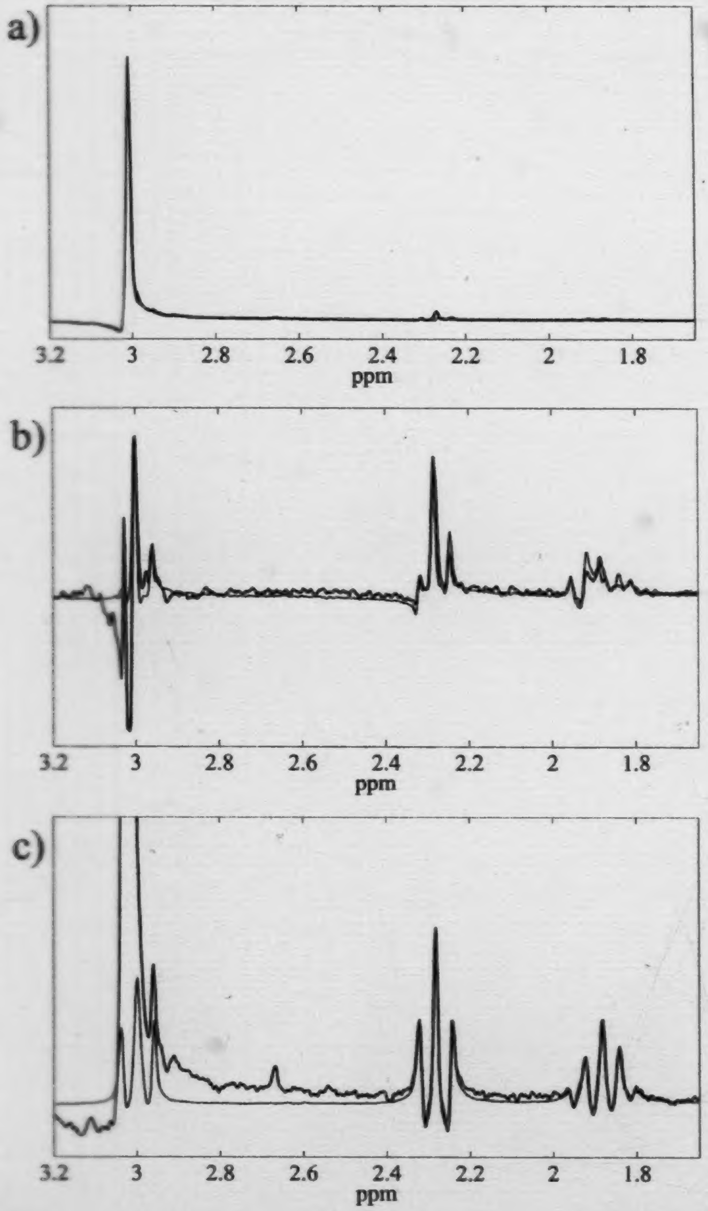

Figure 4-6: *Spectra acquired from the phantom containing GABA and Cr. a) Spectra from both timings used in the experiment: TE1 = 120 ms, TE2 = 11 ms (black) and TE1 = 21 ms, TE2 = 110 ms (red). b) Resultant subtraction spectrum (black) with the results from the GABA only phantom (red). c) A short echo spectrum (TE = 24 ms) for comparison with the similar spectrum from the GABA only phantom in red. All spectra were line broadened using a 1 Hz exponential filter.*

In Fig. 4-6a, the GABA signal at 3.01 is completely obscured by the strong Cr peak at both timings, rendering quantification difficult. The subtraction spectrum in 4-6b shows many similarities to the subtraction spectrum from 4-5b, although there is some residual contamination in the 3.04 – 3.10 range from the Cr signal. However, the dominant peak in the A_2 GABA multiplet is not entirely affected by the Cr residual, and affords the possibility of quantification. The height of this particular peak is very similar to that of the GABA only phantom spectrum, and therefore it is most likely that this peak is composed almost entirely of GABA signal. The spectra in 4-6c are also very similar in shape, and the strong Cr peak envelopes the GABA signal, except for a lesser A_2 peak outside of the Cr range. The remainder of the spectrum matches well with the GABA only spectrum.

4.4 Discussion

These results show that it may be possible to detect GABA at 3 ppm via constant TE difference spectroscopy at 4.7 T, by varying the flip angle of the second refocusing pulse and producing signal asymmetries in TE space. This technique is simple to implement with a standard PRESS sequence, and is therefore available for clinical use. The same results are obtained if the first refocusing pulse is varied, although the asymmetries are flipped in TE space. The addition spectrum maintains all spectral information resulting in a method with no lost information, as can be the case in multiple quantum filtering.

The analytical approximations provided a useful starting point in analyzing the effects of reduced refocusing pulse flip angles in the PRESS sequence, proving useful in the optimization of the flip angle and timings. However, the full simulation method used for GABA incorporates the entire spin structure, and confirmed some results obtained from the analytical model, although deviated in the percent yield and optimal flip angle calculations. The simulator also incorporates soft pulses, which increase the inherent signal loss due to pulse imperfections, which could account for the discrepancies in optimal flip angle calculations with the analytical method. Further simulations have illustrated that an A_2X_2 spin system better approximates the effects of flip angle reduction in case of GABA than a simple AX. The AX approximations shown here are useful in describing the basic properties in TE space due to reduced flip angle, but cannot fully describe the entire A_2X_2 interactions in GABA and therefore should not be used as a direct comparison.

The most sensible target for this type of difference spectroscopy experiment is the GABA A_2 peaks, although it may be possible that overlapping resonance due to glutamate, glutamine and aspartate could be removed from the M_2 multiplet range, as these strongly coupled spin systems respond differently to the flip angle reduction. Preliminary TE space investigations of glutamate have shown a favourable outcome for this approach. Another target for the experiment is the lactate resonance at 1.31 ppm, which is primarily contaminated by macromolecule and fat resonances. Fat is typically modeled as a number of CH_2 constituents forming a long chain, with strong coupling (A_2B_2) between protons on adjacent carbon atoms. These strongly coupled signals could be removed by the proposed method, and could help in lactate quantification in stroke and neurological disease.

This method for GABA detection requires small linewidths for successful subtraction. In this particular experiment, linewidths of 2.8 Hz were achieved after a 1 Hz exponential filter was applied. Linewidths produced by difficult to shim areas will cause contamination of the GABA A_2 signal as the Cr peak broadens. Also, to prevent unnecessary line broadening, a rigorous frequency correction method is needed to align each spectrum acquired. It is possible that narrower linewidths could be achieved by reduction of the number of FIDs needed for phase cycling, as frequency mismatches within the bins tend to broaden the lines artificially.

In addition, the signal to noise ratio (SNR) is the major drawback for future in vivo investigations. The inherent losses in a subtraction spectroscopy experiment coupled with the small GABA concentration in the human brain (1.4 – 2.2 mM (8)) result in more required averages for substantial SNR. However, in these studies, the large concentrations and number of averages produced ample SNR, and therefore, a comparable scanning time (~25 min) may produce viable results at 4.7 T in vivo. Also, a larger voxel could be used to increase SNR, although the linewidth would also increase and may be a detriment to the experiment. As stated previously, the yield is dependent on J and Δ, and other metabolites may produce better subtraction results than GABA

For precise quantification, the macromolecule contribution to the GABA signal needs to be measured (13). A recent study identified a multiple quantum filtering technique for quantifying macromolecules in the human brain (1), but the sequence did not maintain any spectral information other than the macromolecule targets and GABA resonances. The number of averages were also comparable to those employed in this experiment.

Recently, a study investigated the use of an optimized STEAM sequence without spectrally selective pulses or multiple quantum filtering for the simultaneous detection of GABA, glutamate and glutamine in the range of the GABA X_2 resonance (2.28 ppm) (14). The overall contamination of the targeted metabolites by nearby resonances is substantial, even after optimization of the timing parameters to reduce GABA, glutamate and glutamine overlap. This may be partially due a combination of larger voxel sizes (1.9 x 1.9 x 2.0 cm^3) and the voxel chemical shift artefact (15). Also, the SNR is relatively small which may increase quantification discrepancies. However, the study produced valuable results for a standard spectroscopy experiment applied in vivo.

In conclusion, difference spectroscopy of weakly coupled spin systems with reduction of refocusing flip angle provides a new technique for GABA detection. The method requires no spectrally selective pulses and maintains all spectral information. The technique is simple to use with a standard PRESS sequence, and is therefore available for clinical use.

4.5 References

1. Choi CH, Bhardwaj PP, Kalra S, Casault CA, Yasmin US, Allen PS, Coupland NJ. Measurement of GABA and contaminants in gray and white matter in human brain in vivo. Magn Reson Med 2007;58(1):27-33.

2. Shen J, Rothman DL, Brown P. In vivo GABA editing using a novel doubly selective multiple quantum filter. Magn Reson Med 2002;47(3):447-454.

3. Hetherington HP, Newcomer BR, Pan JW. Measurements of human cerebral GABA at 4.1 T using numerically optimized editing pulses. Magn Reson Med 1998;39(1):6-10.

4. Ryner LN, Sorenson JA, Thomas MA. 3D Localized 2D NMR Spectroscopy on an MRI Scanner. Journal of Magnetic Resonance Series B 1995;107(2):126-137.

5. Gambarota G, van der Graaf M, Klomp D, Mulkern RV, Heerschap A. Echo-time independent signal modulations using PRESS sequences: A new approach to spectral editing of strongly coupled AB spin systems. J Magn Reson 2005;177(2):299-306.

6. Rothman DL, Behar KL, Hetherington HP, Shulman RG. Homonuclear H-1 Double-Resonance Difference Spectroscopy of the Rat-Brain Invivo. Proceedings of the National Academy of Sciences of the United States of America-Biological Sciences 1984;81(20):6330-6334.

7. Thompson RB, Allen PS. Sources of variability in the response of coupled spins to the PRESS sequence and their potential impact on metabolite quantification. Magn Reson Med 1999;41(6):1162-1169.

8. Pouwels PJW, Brockmann K, Kruse B, Wilken B, Wick M, Hanefeld F, Frahm J. Regional age dependence of human brain metabolites from infancy to adulthood as detected by quantitative localized proton MRS. Pediatr Res 1999;46(4):474-485.

9. Ogg RJ, Kingsley PB, Taylor JS. WET, a T1- and B1-insensitive water suppression method for in vivo localized 1H NMR spectroscopy. J Magn Reson B 1994;104(1):1-10.

10. Stejskal EO, Schaefer J. Data routing in quadrature FT NMR. J Magn Reson 1974;13(2):249-251.

11. Stejskal EO, Schaefer J. Comparisons of quadrature and single-phase fourier transform NMR. J Magn Reson 1974;14(2):160-169.

12. Govindaraju V, Young K, Maudsley AA. Proton NMR chemical shifts and coupling constants for brain metabolites. NMR Biomed 2000;13(3):129-153.

13. Behar KL, Rothman DL, Spencer DD, Petroff OAC. Analysis of macromolecule resonances in 1H NMR spectra of human brain. Magn Reson Med 1994;32(3):294-302.

14. Hu JN, Yang SL, Xuan Y, Jiang Q, Yang YH, Haacke EM. Simultaneous detection of resolved glutamate, glutamine, and gamma-aminobutyric acid at 4 T. J Magn Reson 2007;185(2):204-213.

15. Wild JM, Marshall I. Normalisation of metabolite images in 1H NMR spectroscopic imaging. Magn Reson Imaging 1997;15(9):1057-1066.

Chapter 5

Determination of Optimal PRESS Timings for Discrimination of Glutamate and Glutamine at 1.5 T, 3 T and 4.7 T

5.1 Introduction

Nuclear magnetic resonance spectroscopy (MRS) is a valuable tool to investigate the metabolic properties of the human brain non-invasively. Within spectrometer limits, many different metabolites are NMR visible and provide insight into the functional pathways of metabolism. One of the primary goals in current research of spectroscopy is to increase the accuracy of metabolite quantification. Typically, an automated program such as LCModel (1,2) or AMARES (3) is used to fit a measured spectrum to a series of basis spectra describing the individual metabolites at the experimental parameters. The confidence of the reported metabolite concentrations from the program generally depends on spectral quality parameters including linewidth and signal to noise ratio (SNR) (4), as well as baseline macromolecular contributions. Most in vivo metabolites are coupled spin systems, and display a degree of spectral complexity, with phase and multiplet height dependent on timing parameters. In addition, the small range of metabolite Larmor frequencies inherent to clinical field strengths for proton spectroscopy results in resonance overlap between metabolites. This large number of intricacies present in spectroscopy makes the quantification of coupled spin systems problematic. Specifically, the similar chemical compositions of glutamate (Glu, an important neurotransmitter) and its inactive form, glutamine (Gln) result in similar resonance frequencies and spectral patterns, and a large overlapping region at standard, short echo timings and clinical field strengths. This overlap tends to decrease the accuracy of the fitting method, with a corresponding decrease in concentration accuracy (5).

Many spectral editing methods have been proposed to aid in quantification of coupled spin systems, such as multiple quantum filtering (6,7), subtraction spectroscopy (Chapters 3 and 4, (8,9)) and J-resolved methods (10). With the exception of difference spectroscopy, these editing techniques require specialized pulse sequences deviating from the standard PRESS and STEAM, which can affect their utility in clinical situations. In addition, multiple quantum filtering in general does not maintain all spectral information, and consequently the quantification of other metabolites can be affected. Difference spectroscopy requires rigorous post-processing schemes to correct for frequency drifts, suffers from low SNR, and is susceptible to dynamic spectrometer errors which reduce the accuracy of the subtraction. The simplest editing technique involves manipulating the timing parameters of the particular spectroscopy sequence (TE1, TE2 – PRESS; TE,TM – STEAM) to produce different J-coupling evolutions and reduce spectral complexity and/or overlap for the target metabolite. No spectral information is lost and this method can be used with standard sequences and processing schemes. In terms of the Glu/Gln resonances, this method has been explored to a limited extent at multiple field strengths using the STEAM sequence (11,12), and at 3T using the PRESS sequence (13).

The Glu and Gln spin systems are both strongly coupled (AMNPQ), with the PQ resonance (Glu: 2.33-2.35 ppm, Gln: 2.43-2.45 ppm) typically being the target for quantification in vivo. The MN peaks (2.03-2.13 ppm) are predominantly obscured by the strong NAA singlet resonance originating at 2.01 ppm, and the comparable resonant frequencies of the A peaks (~3.75 ppm) strongly hinders Glu/Gln discrimination. The overlap between the Glu and Gln PQ resonances is expected to decrease at higher field strengths, as the chemical shift difference (Hz) increases. Therefore, the quantification of Glu and Gln at higher field strengths should display a lower degree of uncertainty. However, the chemical shift difference between P and Q spins will also increase, resulting in a less intense signal as the various peaks in the PQ multiplet split apart. It is not certain how prevalent this effect is for the PQ spins of Glu and Gln at the investigated field strengths, as they are very strongly coupled with a chemical shift difference of ~2 ppm and a J-coupling constant of ~-15 Hz. The achievable shim will also play a role in the spectral overlap in Glu and Gln, and may detract from any gains made at higher field strengths.

In this study, we explore the optimization of timing parameters using a standard PRESS sequence in an effort to eliminate spectral overlap between Glu and Gln at field strengths of 1.5 T, 3 T and 4.7 T. The parameters were investigated first using a spin simulation program, with supporting in vivo experiments at 1.5 T and 4.7 T.

5.2 Methods

5.2.1 Numerical Simulations

Numerical simulations were performed to determine the response of Glu and Gln to a standard PRESS sequence, using an in-house spin simulation program (14) that incorporates chemical shifts, coupling constants, and strong coupling effects for each metabolite. The program segments the sequence into individual, time-independent Hamiltonians characterized as a radiofrequency (RF) pulse, gradient, or time delay. In the case of amplitude modulated soft pulses, the pulse was further divided into minute segments with individual Hamiltonians to maintain time independence. The sinc pulses used in the simulation were based on experimental specifications (256 points, 5 lobes, 2500 selective bandwidth for a 2 ms pulse). Following each segment, the density matrix was calculated and used as the starting point in subsequent segments, with the production of a free induction decay (FID) as the endpoint.

The program was run for various values in TE space with TE1 (first echo time) and TE2 (second echo time) ranging from 5 – 200 ms, totalling 1600 FIDs per metabolite. For each time point, spectra for Glu, Gln and Glx (Glu + Gln) were produced, with the Glx spectrum comprised of a 3:1 Glu:Gln physiological concentration ratio (1,15). TE space area maps were produced for the PQ resonances of Glu and Gln to determine the regions of maximum signal yield. At short TE, each PQ resonance is comprised of a multiplet with decreasing peak amplitude from its center. Therefore, in order to minimize the overlap, time points were investigated to reduce the amplitude of adjacent Glu and Gln outer wings for each multiplet – essentially collapsing the multiplet into a singlet (12) – by examining TE space area maps for individual PQ peaks. At these time points, the contributions of Glu and Gln to the total Glx signal was calculated in the 2.0 – 2.6 ppm range, as well as the total amount of overlap in set regions determined by the frequencies of the collapsed Glu and Gln. Based on these criteria, the optimal SNR and non-overlapping time point was chosen. The entire process was repeated for 1.5 T, 3 T and 4.7 T. Short echo time spectra were also calculated for Glu and Gln (TE = 30 ms) to compare to the optimized results, and demonstrate the metabolite overlap at field strengths of 1.5 T, 3 T, 4.7 T and 7 T.

5.2.2 In Vivo Experiments

Single voxel experiments were performed on healthy volunteers with informed consent using the optimized PRESS timings chosen from the simulation at 1.5 T and 4.7 T. A 2 cm x 2 cm x 2cm voxel was placed in parietal grey matter to maximize the Glu concentration, with the power calibrated to produce maximum signal from the water peak for the voxel. Other sequence parameters included 256 averages, and a repetition time of 1500 ms, resulting in a total acquisition time of 6 min, 24 s.

The 4.7 T experiments were performed using a Varian INOVA whole body MRI system, equipped with a 4 kW RF amplifier, a maximum gradient strength of 35 mT/m and maximum slew rate of 117 T/m*s. A Siemens Sonata equipped with a 15 kW RF amplifier, 40 mT/m gradient set and slew rate of 200 T/m*s was used for the 1.5 T experiments. Both employed a quadrature, 16-element birdcage head coil for transmission and reception.

5.3 Results

5.3.1 Optimized Timings

Figure 5-1 displays the Glu and Gln short echo time (TE = 30 ms) simulation spectra for 1.5 T, 3 T, and 4.7 T (a-c). At 1.5 T, Glu and Gln cannot be resolved as both the MN and PQ groups display a high degree of overlap. Discrimination between Glu and Gln in the 3 T and 4.7 T spectra may be possible, as both Glu and Gln multiplets include non-overlapping peaks in the PQ region (2.3-2.6 ppm). At 4.7 T, the PQ peaks suffer only minimal overlap. In Fig. 5-1d, the same spectra are shown for a field strength of 7 T, for comparison purposes, illustrating the near complete resolution of the Glu/Gln PQ multiplets. It should be noted that the linewidths used in the simulations may not be obtainable in vivo and the spectra are for comparison only.

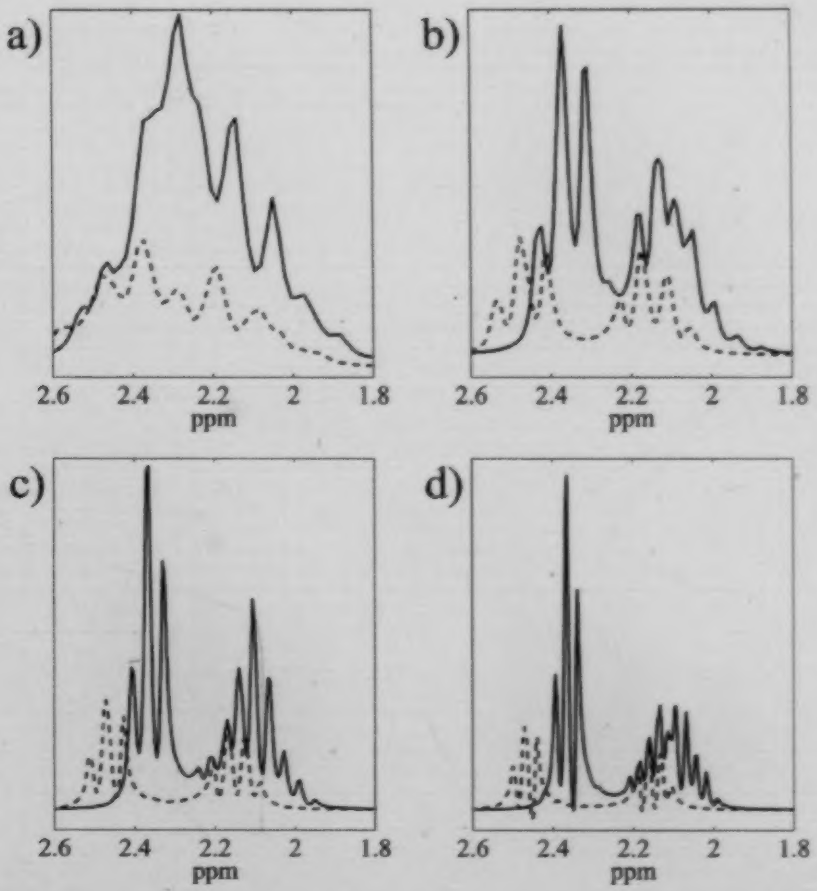

Figure 5-1: Simulated short echo time (TE = 30 ms) spectra of Glu (solid line) and Gln (dashed) at field strengths of a) 1.5 T, b) 3 T, c) 4.7 T, and d) 7 T. All spectra were line broadened to 3 Hz. Relaxation effects are not included. The spectra are not to scale.

The simulated Glu and Gln spectra at the optimal timings determined are shown in Figure 5-2a-c for 1.5 T, 3 T and 4.7 T, respectively. Each plot contains the Glu (blue) and Gln (red) spectrum, and the resultant Glx (black). The shaded regions correspond to the PQ regions calculated from the simulation to be predominantly Gln (red box) and Glu (blue box). The signal composition was then calculated in these two regions to determine the extent of Glu/Gln discrimination. Table 5-1 shows the percentage yield for each metabolite comprising the total Glx signal in each of the highlighted regions.

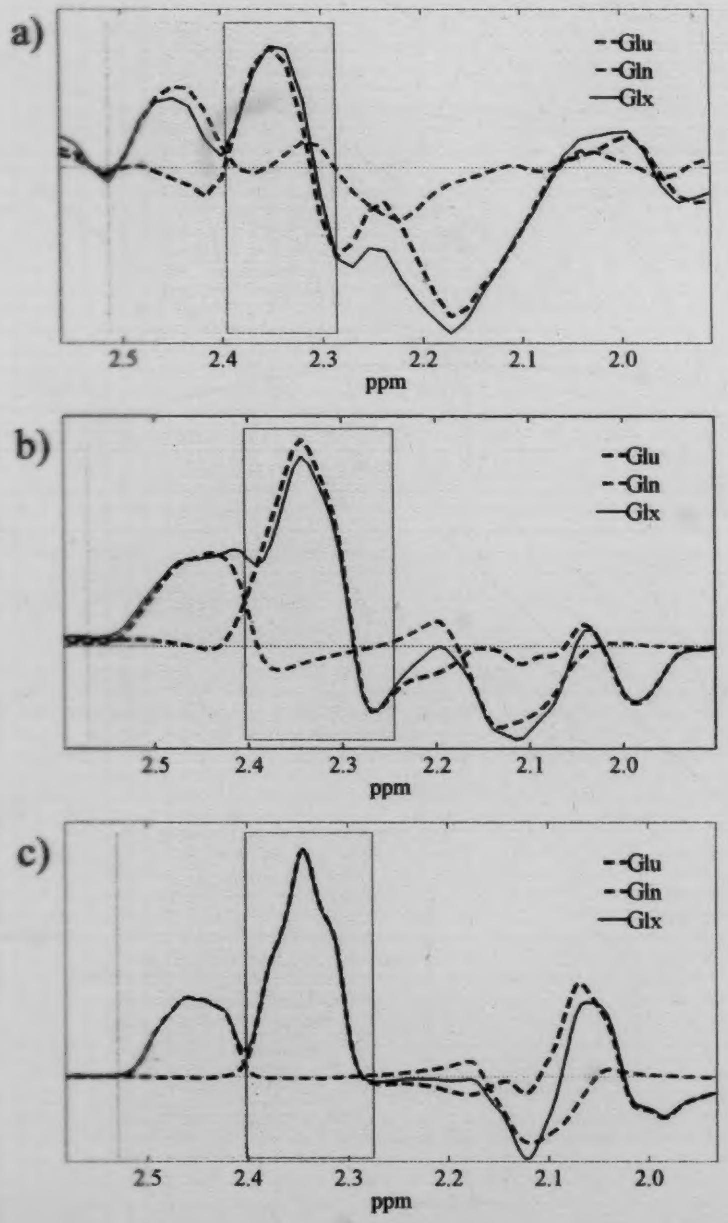

Figure 5-2: *Simulated spectra at optimized timings for Glu (blue line), Gln (red line) and the resultant Glx (black) for a) 1.5 T, b) 3 T and c) 4.7 T. The shaded region denotes the area where the overlap between Glu and Gln is computed, with Glu and Gln PQ ranges determined prior to the calculation (blue and red outlined boxes, respectively).*

Table 5-1: *Calculations of percent metabolite area composition for Glu and Gln at 1.5 T, 3 T, and 4.7 T *.*

Region Type	1.5 T		3 T		4.7 T	
	Glu	Gln	Glu	Gln	Glu	Gln
Blue (Glu region)	83.5	16.5	89.6	10.4	98.8	1.2
Red (Gln region)	31.0	69.0	22.0	78.0	4.2	95.8

* *Values presented are expressed as a percent of the total Glx area*

In 5-2a, the optimal timings for the PRESS experiment were calculated to be TE1 = TE2 = 55 ms for 1.5 T. Considering the appearance of the short TE spectra in 5-1a, the optimization of the timing parameters have offered a drastic improvement in resolution. Gln has the most contamination from Glu at this field strength, with 31 % of the total signal composed of Glu in the Gln region. The intersection at 2.4 ppm of Glu and Gln almost extends to the baseline, and may improve the accuracy of a fitting routine. At 3 T (Fig. 5-2b), the timings as determined from the simulation were TE1 = 30 ms, and TE2 = 85 ms. These simulations show an improvement in signal composition in the two regions, although the intersection of of the Glu and Gln lines is not as sharp as at 1.5 T. The overlap has virtually been eliminated at 4.7 T, with Glu and Gln percent compositions of 98.8 and 95.8 in their respective regions. The timings for the 4.7 T simulations were determined to be TE1 = 20 ms and TE2 = 90 ms. The results indicate that the best reduction in signal overlap should occur at 4.7 T, with minimal contamination.

5.3.2 In Vivo Experiments

The in vivo data is shown in Fig. 5-3 for a) 1.5 T and b) 4.7 T using the optimized timing parameters. The theoretical line shapes for Gln (red) and Glu (blue) are also shown.

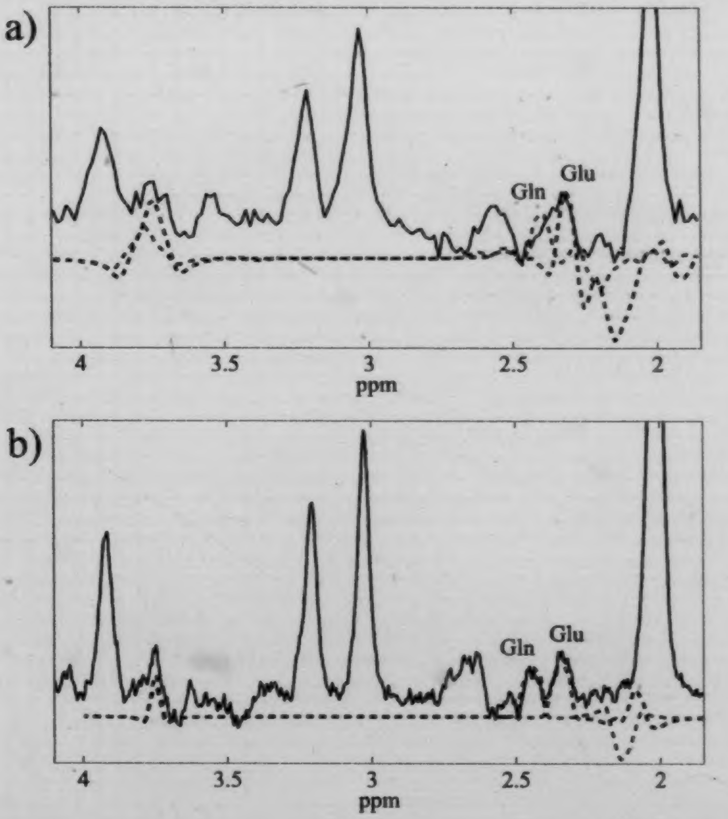

Figure 5-3: *In vivo spectra acquired at optimized timings determined from the simulation at a field strength of a) 1.5 T (TE1 = TE2 = 55 ms), and b) 4.7 T (TE1 = 20 ms, TE2 = 90 ms). The simulated spectra for Glu and Gln are shown in blue and red, respectively. Other sequence parameters included a voxel size of 8 cm^3 voxel size, TR = 1500 ms, and 256 averages.*

The resolution shown for the simulated spectra in 5-2a is not apparent in the in vivo spectra, due to the large linewidth, and therefore the expected possibility of discrimination is not realized. The increased resolution in the 4.7 T experiment allows the overlap to be minimized similar to the simulations. The theoretical lineshapes agree with the in vivo spectrum, and therefore cross-contamination between the two is expected to be minimal as predicted.

5.4 Discussion

This study investigates the optimization of timing parameters for the reduction of overlap between the Glu and Gln resonances in the PQ region (2.3-2.6 ppm) at 1.5 T, 3 T, and 4.7 T. The timings were chosen to collapse the outer wings of each PQ multiplet, and also reduce the contamination of Glu in the Gln region and vice versa. The overlap was calculated to be the least at 4.7 T, with only a 1.2 % and 4.2 % cross-contamination for Glu and Gln respectively. The broad lines in the 1.5 T in vivo studies prevented the possibility of resolving Glu and Gln. Although the amount of spectral overlap in the simulated spectra at 1.5 T was greater than that at 3 T, the 1.5 T lineshape may prove useful if the line broadening can be reduced further. The excellent resolution at 4.7 T showed good lineshape agreement between the simulator and experiment. The optimized timings also provide less spectral overlap than those at standard, clinical short echo times (Fig. 5.1), even triple the linewidth (9 Hz).

In addition to the reduction in spectral overlap, the quantification of Glu and Gln also requires accounting for macromolecular contamination (16), which has been shown to decrease the reliability of reported concentrations (17). Other metabolites may also overlap Glu and Gln at the optimized timings, particularly γ-aminobutyric acid (GABA) with Glu (2.28 ppm) and aspartyl resonances with Gln (2.5-2.65 ppm). A similar investigation including all overlapping metabolites in the Glu/Gln range could be performed to increase the in vivo applicability. The simultaneous detection of Glu, Gln and GABA was previously reported for a STEAM sequence at 4 T (11), with marginal SNR.

A similar experiment using the STEAM sequence (12) investigated timings at 3 T, 4 T, 4.7 T, 7 T and 9 T. The single voxel experiments at 4.7 T were limited to rat brain, and therefore a direct comparison of lineshapes between the PRESS and STEAM sequence is not possible. Both STEAM single voxel experiments (3 T in vivo, 4.7 T rat brain) have low Glu/Gln SNR compared to that shown above, however the spectroscopic imaging sets present promising data. PRESS optimization at 3 T (13) illustrated good Glu SNR, with a large uncertainty in the Glu concentration.

In conclusion, the optimized parameters for 4.7 T illustrate the best discrimination between Glu and Gln and least spectral overlap in the simulations. This was supported by the 4.7 T in vivo experiments, as broad lines hindered resolution at 1.5 T. This preliminary experiment needs to be extended to include quantification schemes and evaluate the accuracy of automated fitting programs between short TE acquisitions and those with optimized timings.

References

1. Provencher SW. Estimation of metabolite concentrations from localized in vivo proton NMR spectra. Magn Reson Med 1993;30(6):672-679.

2. Provencher SW. Automatic quantitation of localized in vivo 1H spectra with LCModel. NMR Biomed 2001;14(4):260-264.

3. Vanhamme L, van den Boogaart A, Van Huffel S. Improved method for accurate and efficient quantification of MRS data with use of prior knowledge. J Magn Reson 1997;129(1):35-43.

4. Jiru F, Skoch A, Klose U, Grodd W, Hajek M. Error images for spectroscopic imaging by LCModel using Cramer-Rao bounds. Magn Reson Mater Phy 2006;19(1):1-14.

5. Bartha R, Drost DJ, Williamson PC. Factors affecting the quantification of short echo in vivo 1H MR spectra: prior knowledge, peak elimination, and filtering. NMR Biomed 1999;12(4):205-216.

6. Thompson RB, Allen PS. A new multiple quantum filter design procedure for use on strongly coupled spin systems found in vivo: Its application to glutamate. Magn Reson Med 1998;39(5):762-771.

7. Wilman AH, Allen PS. Yield Enhancement of a Double-Quantum Filter Sequence Designed for the Edited Detection of GABA. J Magn Reson B 1995;109(2):169-174.

8. Rothman DL, Behar KL, Hetherington HP, Shulman RG. Homonuclear 1H double resonance difference spectroscopy of the rat brain in vivo. Proc Natl Acad Sci U S A 1984;81(20):6330-6334.

9. Gambarota G, van der Graaf M, Klomp D, Mulkern RV, Heerschap A. Echo-time independent signal modulations using PRESS sequences: A new approach to spectral editing of strongly coupled AB spin systems. J Magn Reson 2005;177(2):299-306.

10. Lee HK, Yaman A, Nalcioglu O. Homonuclear J-refocused spectral editing technique for quantification of glutamine and glutamate by 1H NMR spectroscopy. Magn Reson Med 1995;34(2):253-259.

11. Hu JN, Yang SL, Xuan Y, Jiang Q, Yang YH, Haacke EM. Simultaneous detection of resolved glutamate, glutamine, and gamma-aminobutyric acid at 4 T. J Magn Reson 2007;185(2):204-213.

12. Yang SL, Hu JN, Kou ZF, Yang YH. Spectral simplification for resolved glutamate and glutamine measurement using a standard STEAM sequence with optimized timing parameters at 3, 4, 4.7, 7, and 9.4 T. Magn Reson Med 2008;59(2):236-244.

13. Schubert F, Gallinat J, Seifert F, Rinneberg H. Glutamate concentrations in human brain using single voxel proton magnetic resonance spectroscopy at 3 Tesla. Neuroimage 2004;21(4):1762-1771.

14. Thompson RB, Allen PS. Sources of variability in the response of coupled spins to the PRESS sequence and their potential impact on metabolite quantification. Magn Reson Med 1999;41(6):1162-1169.

15. Pouwels PJW, Brockmann K, Kruse B, Wilken B, Wick M, Hanefeld F, Frahm J. Regional age dependence of human brain metabolites from infancy to adulthood as detected by quantitative localized proton MRS. Pediatr Res 1999;46(4):474-485.

16. Behar KL, Rothman DL, Spencer DD, Petroff OAC. Analysis of macromolecule resonances in 1H NMR spectra of human brain. Magn Reson Med 1994;32(3):294-302.

17. Choi CH, Bhardwaj PP, Kalra S, Casault CA, Yasmin US, Allen PS, Coupland NJ. Measurement of GABA and contaminants in gray and white matter in human brain in vivo. Magn Reson Med 2007;58(1):27-33.

Chapter 6

Conclusion

The work conducted during the course of the thesis focused on two main goals. The primary goal of the research was the production of simple editing techniques for weak and strong coupled spin systems. The two variants of difference spectroscopy, with and without flip angle variation (Chapters 3 and 4, respectively), accomplished this task without major changes to the standard spectroscopy sequence. In addition, the optimization of timings in the spectroscopy sequence, without the aid of difference spectroscopy was also investigated (Chapter 5). Though both approaches were aimed at specific metabolites for targets, the generality of the techniques have also been explored for other viable metabolites.

The second goal of the thesis explored field strength issues and the response of coupled spin systems to different fields. The prevalence of the radiofrequency field effect at higher static fields and the resulting effects on quantification was discussed and investigated in spectroscopic imaging of coupled and uncoupled spin systems (Chapter 2). Also, the optimal field strength for strongly coupled spin systems detected via difference spectroscopy was investigated for a variety of metabolites (Chapter 3). Finally, the effect of field strength on an optimally timed spectroscopy sequence was also explored (Chapter 5).

6.1 Constant Echo Time Difference Spectroscopy

The relatively low SNR and consequentially long scan times inherent in proton spectroscopy coupled with the difficulty of detection of many important brain metabolites has limited its application clinically. In an effort to detect metabolites, many editing strategies have been developed, which typically add a degree of complexity to the pulse sequence and/or post-processing. The constant TE difference spectroscopy technique was developed to alleviate the need for specialized pulse sequences while maintaining all spectral information.

The first application (Chapter 3) was based on strong coupling properties, with Glu, Gln and mI used as examples. The signal variation in TE space at 4.7 T allowed a difference spectroscopy experiment to differentiate between Glu and Gln using the MN resonance in the 2.04-2.14 ppm range, while maintaining a strong mI signal at 3.55 ppm. The total Glx signal in the MN region was calculated to be 96 % Glu in the simulations, which agreed well with the phantom experiments. The total yield compared to a similar experiment without difference spectroscopy was calculated to be 53 %. The signal yield calculated for mI was 73 %. The signal yield calculated from the analytical equations was dependent on field and coupling strength, and based on the equations the technique was extended in general to eight metabolite spin systems to investigate the performance of difference spectroscopy at multiple field strengths.

The second application extended the treatment to weakly coupled spin systems (Chapter 4), by changing the flip angle of the final refocusing pulse in the PRESS sequence to introduce signal variations in TE space (90°-180°-120°). The detection of the obscured A_2 resonance (3.01 ppm) of GABA was used as an example, with a yield of 30 % predicted by the simulator after subtraction. The signal yield was determined to also be dependent on coupling properties and field strength, although these effects were not investigated fully.

The primary limiting factor of the constant TE difference spectroscopy technique is the low SNR. This is especially apparent in the GABA study. The low concentration of GABA in vivo (1.4 – 2.2 ppm, (1)) and the additional signal loss due to the subtraction experiment (30 % maximum yield) can reduce the GABA signal to the noise level, rendering it undetectable. The Cr peak also needs to be reduced by roughly a factor of 10 to be of the same order of magnitude as GABA.

A second drawback of constant TE difference spectroscopy is the dependence of the subtraction results on frequency drift. In order to produce accurate results and minimize unnecessary line broadening, the number of points in each spectrum needs to be increased by interpolation (10 times the number of points are used in this research) before frequency correction. In addition, the phase of each spectrum must also be the same to reduce subtraction errors, requiring a robust automated scheme. Some of the frequency drifts during measurement of the FIDs cannot be corrected, if phase cycling is used. In order to apply a phase cycling scheme, a number of spectra (8 for CYCLOPS) need to be binned together during acquisition. In this work, eight spectra were acquired in succession at one of the chosen time points, followed by another set of eight at the second time point, and repeated until the number of averages required is obtained. Therefore, the frequency drift within a set of FIDs cannot be accounted for – only the overall drift for the set is measured, causing an overall broadening in a specific set. Subtraction errors are introduced if the second set of FIDs has different individual frequency drifts, resulting in a different amount of line broadening.

6.2 Static Field Considerations

The effects of different static magnetic field strengths were studied concurrently with the other projects. A higher field strength in theory should provide greater SNR and better resolution in the frequency domain. The achievable linewidths in vivo as measured in this thesis were 3 Hz (1.5 T), 5 Hz (3 T), and 8 Hz (4.7 T) for an 8 cm^3 voxel located in parietal grey matter. In terms of the ppm scale, this translates to 0.05 ppm (1.5 T), 0.04 ppm (3 T) and 0.04 ppm (4.7 T). Therefore, only a minimal decrease in linewidth was realized at higher field (in ppm). Also, the J-coupling constant is not field dependent, and therefore at higher fields the multiplets produced via J-coupling will appear more compact on the ppm scale. This phenomena in combination with the relatively poor linewidths observed in the experiment at 1.5 T and greater SNR at high field result in superior results for 4.7 T as shown in Chapter 5.

A higher field strength also produces more RF inhomogeniety, and can decrease the accuracy of spectral quantification. The RF interference effect results in a reduction of flip angle from optimal for voxels located near the edge of the brain in spectroscopic imaging experiments. At 4.7 T, this reduction is 50 % of the maximum observed in the center of the brain, whereas it is only 20 % at 3 T and negligible at 1.5 T (2). In Chapter 2, these high field effects were explored in spectroscopic imaging for coupled and uncoupled spin systems. The destructive interference pattern resulted in a 70 % reduction in Glx yield compared to a 42 % reduction in Cho for voxels located on the edges of the spectroscopic imaging grid. Therefore, if these differences in response to the RF inhomogeniety are not addressed, it is advantageous to perform quantitative spectroscopic imaging studies at lower field.

All experiments performed in the thesis rely heavily on numerical simulation to predict the response of spins to the PRESS sequence. TE space analysis and line shape investigation require a rigorous spin simulation program. This type of a priori knowledge may not be available to all researchers, and is therefore a general limitation in this work.

6.3 Future Investigations

The first area of future exploration should be the quantification of the various edited metabolites investigated as examples in this work (Glu, Gln, mI, GABA) via an automated fitting program such as LCModel (3). Much of the theory and utility of the techniques have been shown in this thesis, and therefore the actual effect of editing should be quantified and compared directly to the results shown in other studies (4-7). The supporting in vivo work should also be investigated more thoroughly for Chapter 3, 4 and 5 using a quantification scheme. Once the quantification has been established, a clinical study involving one of the metabolites (Glu in particular) could be explored to study the function of coupled spins in disease using these techniques, and improve upon the accuracy of previous quantification methods.

Chapter 3 provided the optimal field strengths for the detection of eight common in vivo spin systems using constant echo time difference spectroscopy, based on analytical approximations; only two of those were investigated in this thesis. The dependence of yield on the coupling constant and field strength requires more clarification in Chapter 4 in order to calculate optimal field strengths for various weakly coupled systems. The optimization of timings for Glu and Gln detection presented in Chapter 5 should also account for other resonances in the targeted ppm range, namely NAA, GABA, and macromolecular contributions. The technique can also be extended to other metabolites of interest by analysis of TE space and overlapping resonances, and could include multiple field strengths.

In conclusion, the techniques described in this thesis offer a simple approach to spectral editing of coupled spin systems, with application to many interesting in vivo metabolites.

6.4 References

1. Pouwels PJW, Brockmann K, Kruse B, Wilken B, Wick M, Hanefeld F, Frahm J. Regional age dependence of human brain metabolites from infancy to adulthood as detected by quantitative localized proton MRS. Pediatr Res 1999;46(4):474-485.

2. Collins CM, Smith MB. Signal-to-noise ratio and absorbed power as functions of main magnetic field strength, and definition of "90 degrees " RF pulse for the head in the birdcage coil. Magn Reson Med 2001;45(4):684-691.

3. Provencher SW. Estimation of metabolite concentrations from localized in vivo proton NMR spectra. Magn Reson Med 1993;30(6):672-679.

4. Hu JN, Yang SL, Xuan Y, Jiang Q, Yang YH, Haacke EM. Simultaneous detection of resolved glutamate, glutamine, and gamma-aminobutyric acid at 4 T. J Magn Reson 2007;185(2):204-213.

5. Schubert F, Gallinat J, Seifert F, Rinneberg H. Glutamate concentrations in human brain using single voxel proton magnetic resonance spectroscopy at 3 Tesla. Neuroimage 2004;21(4):1762-1771.

6. Yang SL, Hu JN, Kou ZF, Yang YH. Spectral simplification for resolved glutamate and glutamine measurement using a standard STEAM sequence with optimized timing parameters at 3, 4, 4.7, 7, and 9.4 T. Magn Reson Med 2008;59(2):236-244.

7. Shen J, Rothman DL, Brown P. In vivo GABA editing using a novel doubly selective multiple quantum filter. Magn Reson Med 2002;47(3):447-454.

Appendix 1

Spin Matrices for a Two Spin System

In a two spin system, with spins labeled I and S, spin matrices have dimensions 4 x 4, and can be calculated from the 2 x 2 one spin matrices by taking the direct product of the corresponding one spin matrix with the identity matrix, as shown in section 1.2.2. In each case, it is important to preserve the order of the direct product. To calculate an arbitrary I spin matrix, I_n, the format is $I_{OS,n}$ x 1, where 1 in this case is the identity operator, and the subscript OS denotes the one spin representation of I_n. The method to calculate an arbitrary S_n matrix is similar, with differing order of multiplication: 1 x $S_{OS,n}$. In this manner, the necessary matrices for the I and S spins in the 2 spin system can be determined. The I_Z and S_Z matrices in the two spin system were calculated as an example in section 1.2.2.

$$I_X = \frac{1}{2}\begin{bmatrix} 0 & 0 & 1 & 0 \\ 0 & 0 & 0 & 1 \\ 1 & 0 & 0 & 0 \\ 0 & 1 & 0 & 0 \end{bmatrix} \tag{A1.1}$$

$$I_Y = \frac{i}{2}\begin{bmatrix} 0 & 0 & -1 & 0 \\ 0 & 0 & 0 & -1 \\ 1 & 0 & 0 & 0 \\ 0 & 1 & 0 & 0 \end{bmatrix} \tag{A1.2}$$

$$I_Z = \frac{1}{2}\begin{bmatrix} 1 & 0 & 0 & 0 \\ 0 & 1 & 0 & 0 \\ 0 & 0 & -1 & 0 \\ 0 & 0 & 0 & -1 \end{bmatrix} \tag{A1.3}$$

$$S_X = \frac{1}{2}\begin{bmatrix} 0 & 1 & 0 & 0 \\ 1 & 0 & 0 & 0 \\ 0 & 0 & 0 & 1 \\ 0 & 0 & 1 & 0 \end{bmatrix} \tag{A1.4}$$

$$S_Y = \frac{i}{2}\begin{bmatrix} 0 & -1 & 0 & 0 \\ 1 & 0 & 0 & 0 \\ 0 & 0 & 0 & -1 \\ 0 & 0 & 1 & 0 \end{bmatrix} \tag{A1.5}$$

$$S_Z = \frac{1}{2}\begin{bmatrix} 1 & 0 & 0 & 0 \\ 0 & -1 & 0 & 0 \\ 0 & 0 & 1 & 0 \\ 0 & 0 & 0 & -1 \end{bmatrix} \tag{A1.6}$$

The raising and lowering operators can be determined from these matrices by using the relation:

$$I_{\pm} = I_X \pm iI_Y \quad \text{and} \quad S_{\pm} = S_X \pm iS_Y. \tag{A1.7}$$

Consequently, the matrix forms for the raising and lowering operators are:

$$I_{+} = \begin{bmatrix} 0 & 0 & 1 & 0 \\ 0 & 0 & 0 & 1 \\ 0 & 0 & 0 & 0 \\ 0 & 0 & 0 & 0 \end{bmatrix} \tag{A1.8}$$

$$I_- = \begin{bmatrix} 0 & 0 & 0 & 0 \\ 0 & 0 & 0 & 0 \\ 1 & 0 & 0 & 0 \\ 0 & 1 & 0 & 0 \end{bmatrix} \tag{A1.9}$$

$$S_+ = \begin{bmatrix} 0 & 1 & 0 & 0 \\ 0 & 0 & 0 & 0 \\ 0 & 0 & 0 & 1 \\ 0 & 0 & 0 & 0 \end{bmatrix} \tag{A1.10}$$

$$S_- = \begin{bmatrix} 0 & 0 & 0 & 0 \\ 1 & 0 & 0 & 0 \\ 0 & 0 & 0 & 0 \\ 0 & 0 & 1 & 0 \end{bmatrix} \tag{A1.11}$$

Appendix 2

Product Operator Transformation Tables

The transformations for the common Hamiltonians found in spectroscopy experiments are shown below, with the two interacting spins labeled I and S. The transformations are shown using both the Cartesian operator system and the raising and lowering operator approach, with the Hamiltonian transforming the operator shown above the arrow. The transformations apply to weakly coupled systems only:

A2.1 Transformations in Cartesian Coordinates

A2.1.1 Radiofrequency Pulses

$$\begin{aligned} I_X &\xrightarrow{-\gamma B_1 I_X t} I_X \\ I_Y &\xrightarrow{-\gamma B_1 I_X t} I_Y \cos(\gamma B_1 t) + I_Z \sin(\gamma B_1 t) \\ I_Z &\xrightarrow{-\gamma B_1 I_X t} I_Z \cos(\gamma B_1 t) + I_Y \sin(\gamma B_1 t) \end{aligned} \tag{A2.1}$$

$$\begin{aligned} I_X &\xrightarrow{-\gamma B_1 I_Y t} I_X \cos(\gamma B_1 t) - I_Z \sin(\gamma B_1 t) \\ I_Y &\xrightarrow{-\gamma B_1 I_Y t} I_Y \\ I_Z &\xrightarrow{-\gamma B_1 I_Y t} I_Z \cos(\gamma B_1 t) + I_X \sin(\gamma B_1 t) \end{aligned} \tag{A2.2}$$

A2.1.2 Chemical Shift

$$\begin{aligned} I_X &\xrightarrow{-\omega_I I_Z t} I_X\cos(\omega_I t)+I_Y\sin(\omega_I t) \\ I_Y &\xrightarrow{-\omega_I I_Z t} I_Y\cos(\omega_I t)-I_X\sin(\omega_I t) \\ I_Z &\xrightarrow{-\omega_I I_Z t} I_Z \end{aligned} \tag{A2.3}$$

A2.1.3 Weak Coupling

$$\begin{aligned} I_X &\xrightarrow{2\pi J I_Z S_Z t} I_X\cos(\pi Jt)+2I_Y S_Z\sin(\pi Jt) \\ I_Y &\xrightarrow{2\pi J I_Z S_Z t} I_Y\cos(\pi Jt)-2I_X S_Z\sin(\pi Jt) \\ I_Z &\xrightarrow{2\pi J I_Z S_Z t} I_Z \\ I_X S_X &\xrightarrow{2\pi J I_Z S_Z t} I_X S_X \\ I_X S_Y &\xrightarrow{2\pi J I_Z S_Z t} I_X S_Y \\ I_X S_Z &\xrightarrow{2\pi J I_Z S_Z t} I_X S_Z\cos(\pi Jt)+\frac{1}{2}I_Y\sin(\pi Jt) \\ I_Y S_Y &\xrightarrow{2\pi J I_Z S_Z t} I_Y S_Y \\ I_Y S_Z &\xrightarrow{2\pi J I_Z S_Z t} I_Y S_Z\cos(\pi Jt)-\frac{1}{2}I_X\sin(\pi Jt) \\ I_Z S_Z &\xrightarrow{2\pi J I_Z S_Z t} I_Z S_Z \end{aligned} \tag{A2.4}$$

A2.2 Raising and Lowering Operator Transformations

A2.2.1 Radiofrequency Pulses

$$\begin{aligned} I_+ &\xrightarrow{-\gamma B_1 I_X t} \frac{1}{2}\left[I_+\left(1+\cos(\gamma B_1 t)\right)+I_-\left(1+\cos(\gamma B_1 t)\right)\right]-iI_Z\sin(\gamma B_1 t) \\ I_- &\xrightarrow{-\gamma B_1 I_X t} \frac{1}{2}\left[I_-\left(1+\cos(\gamma B_1 t)\right)+I_+\left(1+\cos(\gamma B_1 t)\right)\right]-iI_Z\sin(\gamma B_1 t) \\ I_Z &\xrightarrow{-\gamma B_1 I_X t} \frac{i}{2}(I_+-I_-)\sin(\gamma B_1 t)+I_Z\cos(\gamma B_1 t) \end{aligned} \tag{A2.5}$$

$$\begin{aligned}
I_+ &\xrightarrow{-\gamma B_1 I_Y t} \frac{1}{2}\left[I_+\left(1+\cos\left(\gamma B_1 t\right)\right) - I_-\left(1-\cos\left(\gamma B_1 t\right)\right)\right] - iI_Z \sin\left(\gamma B_1 t\right) \\
I_- &\xrightarrow{-\gamma B_1 I_Y t} \frac{1}{2}\left[I_-\left(1+\cos\left(\gamma B_1 t\right)\right) - I_+\left(1-\cos\left(\gamma B_1 t\right)\right)\right] - iI_Z \sin\left(\gamma B_1 t\right) \\
I_Z &\xrightarrow{-\gamma B_1 I_Y t} \frac{i}{2}\left(I_+ + I_-\right)\sin\left(\gamma B_1 t\right) + I_Z \cos\left(\gamma B_1 t\right)
\end{aligned} \tag{A2.6}$$

A2.2.2 Chemical Shift

$$\begin{aligned}
I_+ &\xrightarrow{-\omega_I I_Z t} I_+ e^{-i\omega_I t} \\
I_- &\xrightarrow{-\omega_I I_Z t} I_- e^{i\omega_I t} \\
I_Z &\xrightarrow{-\omega_I I_Z t} I_Z
\end{aligned} \tag{A2.7}$$

A2.2.3 Weak Coupling

$$\begin{aligned}
I_+ &\xrightarrow{2\pi J I_Z S_Z t} I_+ \cos\left(\pi J t\right) - 2iI_+ S_Z \sin\left(\pi J t\right) \\
I_- &\xrightarrow{2\pi J I_Z S_Z t} I_- \cos\left(\pi J t\right) - 2iI_- S_Z \sin\left(\pi J t\right) \\
I_Z &\xrightarrow{2\pi J I_Z S_Z t} I_Z \\
I_+ S_+ &\xrightarrow{2\pi J I_Z S_Z t} I_+ S_+ \\
I_+ S_- &\xrightarrow{2\pi J I_Z S_Z t} I_+ S_- \\
I_+ S_Z &\xrightarrow{2\pi J I_Z S_Z t} I_+ S_Z \cos\left(\pi J t\right) - \frac{i}{2} I_+ \sin\left(\pi J t\right) \\
I_- S_- &\xrightarrow{2\pi J I_Z S_Z t} I_- S_- \\
I_- S_Z &\xrightarrow{2\pi J I_Z S_Z t} I_- S_Z \cos\left(\pi J t\right) + \frac{i}{2} I_- \sin\left(\pi J t\right) \\
I_Z S_Z &\xrightarrow{2\pi J I_Z S_Z t} I_Z S_Z
\end{aligned} \tag{A2.8}$$

Appendix 3

Product Operator Transformation Tables for a Strongly Coupled Two Spin System

Some common transformations listed in Kay and McClung (Ref. 61, Chapter 1) for the commuting strongly coupled Hamiltonians using the spherical angular momentum operators are listed below for an AB system. The Hamiltonians are defined as:

$$\begin{aligned} \mathcal{H}_0 &= \bar{\omega}\left(A_Z + B_Z\right) + 2\pi J A_Z B_Z, \\ \mathcal{H}_1 &= \delta\omega\left(A_Z - B_Z\right) + 2\pi J\left(A_X B_X + A_Y B_Y\right), \end{aligned} \tag{A3.1}$$

where $\delta\omega = (\omega_A - \omega_B)/2$, $\bar{\omega} = \left(\omega_A + \omega_B\right)/2$ and $\Lambda = \sqrt{\left(\delta\omega\right)^2 + \left(\pi J\right)^2}$. J is the coupling constant between the A and B spins.

$$\begin{aligned} & A_+ \xrightarrow{\mathcal{H}_0 t} e^{-i\bar{\omega}t}\left(A_+ \cos\left(\pi J t\right) - 2iA_+ B_Z \sin\left(\pi J t\right)\right) \\ & B_+ \xrightarrow{\mathcal{H}_0 t} e^{-i\bar{\omega}t}\left(B_+ \cos\left(\pi J t\right) + 2iB_+ A_Z \sin\left(\pi J t\right)\right) \\ & 2A_+ B_Z \xrightarrow{\mathcal{H}_0 t} e^{-i\bar{\omega}t}\left(2A_+ B_Z \cos\left(\pi J t\right) + iB_+ \sin\left(\pi J t\right)\right) \\ & 2B_+ A_Z \xrightarrow{\mathcal{H}_0 t} e^{-i\bar{\omega}t}\left(2B_+ A_Z \cos\left(\pi J t\right) + iA_+ \sin\left(\pi J t\right)\right) \\ & A_Z \xrightarrow{\mathcal{H}_0 t} A_Z \end{aligned} \tag{A3.2}$$

$$\begin{aligned}
&A_+ \xrightarrow{\mathcal{H}t} A_+\left(\cos(\Lambda t) - i\frac{\delta\omega}{\Lambda}\sin(\Lambda t)\right) + 2iA_Z B_+ \frac{\pi J}{\Lambda}\sin(\Lambda t) \\
&B_+ \xrightarrow{\mathcal{H}t} B_+\left(\cos(\Lambda t) + i\frac{\delta\omega}{\Lambda}\sin(\Lambda t)\right) + 2iB_Z A_+ \frac{\pi J}{\Lambda}\sin(\Lambda t) \\
&2A_+B_Z \xrightarrow{\mathcal{H}t} 2A_+B_Z\left(\cos(\Lambda t) - i\frac{\delta\omega}{\Lambda}\sin(\Lambda t)\right) + iB_+ \frac{\pi J}{\Lambda}\sin(\Lambda t) \\
&2B_+A_Z \xrightarrow{\mathcal{H}t} 2B_+A_Z\left(\cos(\Lambda t) + i\frac{\delta\omega}{\Lambda}\sin(\Lambda t)\right) + iA_+ \frac{\pi J}{\Lambda}\sin(\Lambda t) \qquad \text{(A3.3)} \\
&A_Z + B_Z \xrightarrow{\mathcal{H}t} A_Z + B_Z
\end{aligned}$$